MARTA DIES

# COUPLED DYNAMICAL PROCESSES IN BACTERIA

DIRECTOR: JORDI GARCIA-OJALVO

TUTORA: MARIA CARME TORRENT SERRA

TESI PRESENTADA PER OBTENIR EL TÍTOL DE DOCTORA

DEPARTAMENT DE FÍSICA I ENGINYERIA NUCLEAR

UNIVERSITAT POLITÈCNICA DE CATALUNYA

BARCELONA, AGOST 2015


UNIVERSITAT POLITÈCNICA
DE CATALUNYA
BARCELONATECH

*A l'Albert, per ensenyar-me els avantatges de viure en el present.*
*A l'Otger, per fer-me practicar.*

*"Science is a way of thinking*
*much more than it is a body of knowledge"*
*— Carl Sagan, 1997*

*From P D Hutcheon. Carl Sagan and Modern Scientific Humanism. Humanist in Canada, 33:6-9, Autumn 1997.*

# *Agraïments*

És tradició encetar el manuscrit d'una Tesi Doctoral reconeixent el mèrit a tots aquells que han ajudat d'una manera o altra a fer-la possible. En el meu cas, hi ha moltíssima gent a qui he d'agrair una bona pila de coses, no sé on acabarà la meva llista de reconeixements, el que sí sé però és per qui començar.

Jordi, moltíssimes gràcies per haver-me acollit en el teu grup i haver confiat en mi. Infinites gràcies per les teves idees i suggeriments que sempre arribaven com el "setè de caballeria" al rescat, salvant la situació quan em pensava que ja estava tot perdut.

Amb molta nostàlgia recordo el nostre antic grup, a la UPC al campus de Terrassa: Belén, Pau, el (J.) Tiana, el (J.) Zamora, Dani, Lorena, Elena, Toni, Núria, Cristina, Carme, Crina, Ramon. Especialment, li dec a l'Elena que aquesta Tesi hagi pogut veure la llum, les seves incontables indicacions sobre com millorar el manuscrit han estat molt importants. Elena, moltes gràcies per animar-me quan em pensava que no ho aconseguiria, ets una súper postdoc i una molt bona amiga! També li dec al Pau moltes coses, des de que "m'iniciés" en l'*AUTO* fins a l'estética d'aquesta Tesi, ja que va ser ell qui em va parlar del *Tufte-LaTeX* i em va passar el format. També em vaig inspirar en la seva Tesi [Rué, 2013] per redactar el tancament final d'aquest manuscrit. Belén, moltes gràcies pel teu suport des d'Ottawa! Encara a la UPC a Terrassa vull mencionar la Montse (moltes gràcies per ajudar-me amb les factures) i el Jaume (artífex de la primera cambra incubadora del microscopi).

Del nou grup a la UPF, he d'agrair al Marçal, la Nara, l'Alessandro, el Maciek, la Lara, la Rosa, el Bernat, la Marit, la Grace i l'Ariadna que sempre es respirés bon ambient i no faltessin els somriures en les meves breus incursions al despatx dels teòrics. També li agraeixo a la Letícia que fes molt més divertit i humà l'exili del laboratori, i que em donés un cop de mà en el tortuós tram final del doctorat. Dins l'ambient jove i dinàmic del PRBB he pogut conèixer científiques excel·lents que han estat font d'inspiració per compaginar la recerca i la maternitat: moltes gràcies Bàrbara i Andreea.

I would also like to thank Michael Elowitz and James Locke the tremendous opportunity to work with them and their people. I learned countless things while collaborating with them, but probably what I appreciate the most is the experience of working in a team.

Però l'ajut per tirar endavant aquesta Tesi no només ha sortit del món acadèmic. No són poques les forces que he pogut recuperar al llarg del camí gràcies al caliu i els ànims dels amics. Mireia i família, gràcies per no haver tirat mai la tovallola i haver seguit insistint una setmana i una altra per trobar una estona per veure'ns. Ballarines i ioguinis: Núria, Helena, Íngrid, Paula i Sílvia, moltes gràcies per ser-hi en la distància. Jordi, Ángel, César y Mari voy a arriesgarme y daros las gracias por adelantado por la celebración.

Finalment, arriba el moment de reconèixer el mèrit més gran de tots: res de tot això no hagués estat possible sense el suport incondicional de la meva família. Pare, moltes gràcies per haver-me encomanat el teu amor per la ciència i el coneixement. Mare, moltes gràcies per ensenyar-me amb el teu exemple a ser valenta i treure forces d'on semblava que ja no n'hi havia. Albert, estic en deute amb tu per tot l'ajut que sempre m'has donat. Gràcies pel teu suport i la teva fe en mi i en aquest projecte. Otger, m'hagués agradat agrair-te les nits de descans reparador, malauradament no ha pogut ser (de moment!), així que t'agrairé que hagis creat una versió més eficient de mi mateixa.

# *Resum*

L'objectiu d'aquesta Tesi és l'estudi de l'acoblament dinàmic entre processos cel·lulars, i de com aquest acoblament genera un comportament ben definit en presència de no-linealitats i soroll. Un funcionament cel·lular correcte depèn de la coordinació exquisida entre un gran nombre de processos dinàmics no lineals subjectes a fluctuacions, que s'esdevenen simultàniament dins la cèl·lula. Aquests tipus de processos dinàmics no tenen lloc de manera aïllada en una cèl·lula sinó que ocorren de manera simultània, essent per tant necessari establir l'origen i el grau de coordinació entre ells. Totes aquestes qüestions romanen encara sense resposta.

A la Part I introduïm i motivem els dos tipus de dinàmiques cel·lulars que hem estudiat en aquesta Tesi. Dediquem la Part II als polsos d'expressió o activitat de proteïnes (Capítols 2 i 3), mentre que ens concentrem en les oscil·lacions periòdiques d'expressió de proteïnes a la Part III (Capítol 4). Concretament, en el Capítol 2 abordem la qüestió sobre com l'acoblament de certs senyals d'entrada afecten la resposta del circuit que regula la competència per a la incorporació d'ADN en *Bacillus subtilis*. En cèl·lules silvestres i sota determinades condicions d'estrès ambiental, s'ha determinat que l'estat de competència segueix una dinàmica de polsos estocàstics. Aquí estudiem com la resposta dinàmica del circuit de competència varia des de polsos excitables fins a la biestabilitat i les oscil·lacions, depenent de l'acció conjunta de les dues entrades acoblades aplicades al sistema. Els efectes fenotípics reportats en aquest Capítol són causats per canvis en el comportament dinàmic del circuit genètic subjacent. L'anàlisi d'estabilitat d'un model teòric del circuit de competència estableix els diferents règims dinàmics que pot exhibir el circuit, els quals estan quantitativament d'acord amb els resultats experimentals.

Seguint amb dinàmiques de polsos, al Capítol 3 estudiem l'acoblament dinàmic entre polsos d'activitat de proteïnes en cèl·lules individuals. A aquest efecte, en col·laboració amb el laboratori del Prof. M. Elowitz de l'Institut de Tecnologia de Califòrnia, vàrem concentrar-nos en la família de factors sigma alternatius en *B. subtilis*. Els factors sigma són proteïnes que s'uneixen a l'ARN polimerasa de manera reversible, fent possible el reconeixement de promotors específics per part de l'holoenzim format. En aquest Capítol mostrem que diversos factors sigma alternatius presenten polsos estocàstics en la seva activació, i que aquests polsos competeixen per l'ARN polimerasa. A la llum d'aquests resultats proposem un nou mecanisme de repartiment, que anomenem en anglès "time-share", pel qual els factors sigma fan torns en el temps per utilitzar la majoria d'ARN polimerasa disponible. D'aquesta manera, només un o molt pocs factors sigma estarien actius simultàniament en una mateixa cèl·lula. També hem desenvolupat una sèrie de models matemàtics que revelen com els polsos i la competició afecten la distribució de l'ARN polimerasa.

Al Capítol 4 estudiem com un oscil·lador genètic sintètic està acoblat a la replicació i la divisió cel·lular. Vam utilitzar l'oscil·lador sintètic desenvolupat per a *Escherichia coli* al laboratori del Prof. J. Hasty a la Universitat de Califòrnia San Diego. Mostrem com el cicle cel·lular bacterià és capaç d'entrenar parcialment les oscil·lacions sintètiques de manera consistent en condicions de creixement normal, tot dirigint la replicació periòdica dels gens involucrats en l'oscil·lador. També exposem que la sincronització entre els dos processos periòdics s'incrementa si l'oscil·lador sintètic es retroacobla al cicle cel·lular mitjançant l'expressió d'un inhibidor de la iniciació de la replicació. A més, hem desenvolupat un model computacional simplificat que confirma aquest efecte.

Finalment, a la Part IV (Capítol 5) resumim i discutim els principals resultats presentats en aquesta Tesi, i suggerim direccions futures cap a on ampliar la recerca.

# *Summary*

The main object of this Doctoral Thesis is the study of the dynamical coupling between cellular processes, and how this coupling gives rise to a well-defined behavior in the presence of non-linearities and noise. Cell functioning relies on the exquisite coordination between a large number of dynamical nonlinear processes subject to fluctuations, which simultaneously operate within the cell. Many cellular dynamical processes occur in the form of periodic oscillations in the expression and/or activation of proteins. Also, more complex dynamics have been identified recently in the form of transient pulses occurring at random. These types of dynamical processes do not occur in isolation in a cell but they do so simultaneously, and therefore it is necessary to establish the origin and level of coordination between them. All these issues still remain unanswered. To address the different questions posed in this Thesis, we have used experimental and theoretical approaches.

In Part I we introduce and motivate the two types of cellular dynamics studied in this Thesis. Part II is devoted to pulses of protein expression or activity (Chapters 2 and 3), whereas in Part III we concentrate in periodic oscillations in protein expression (Chapter 4). Specifically, in Chapter 2 we focus on how the coupling of certain inputs affect the response of the circuit regulating competence for DNA uptake in *Bacillus subtilis*. In wild-type cells, under certain environmental stress conditions, competence has been found to follow a stochastic pulsing dynamics. Here we study how the dynamical response of the competence circuit varies from excitable pulses to bistability and oscillations depending on the joint action of two coupled inputs applied to the system. The phenotypical effects reported in this Chapter are caused by changes in the dynamical behavior of the underlying genetic circuit. The stability analysis of a theoretical model of the competence circuit establishes the various dynamical regimes that the circuit can exhibit, which are in very good quantitative agreement with experimental results.

Still dealing with pulsing dynamics, in Chapter 3 we study the dynamical coupling between pulses of protein activity in single cells. For that purpose, in collaboration with Prof. M. Elowitz's laboratory from the California Institute of Technology, we concentrated in the alternative sigma factors family in *B. subtilis*. Sigma factors are proteins that reversibly bind to core RNA polymerase thus giving the formed holoenzyme promoter-recognition properties. In this Chapter we show for the first time that several alternative sigma factors present stochastic pulses in their activation, and that these pulses take place in conditions of competition for core RNA polymerase. In the light of these results, we propose a new mechanism, "time-sharing", in which sigma factors take turns in order to use most of the available RNA polymerase, with only one or a few sigma factors being simultaneously active in a given cell. We also develop several mathematical models that shed light on how pulsing and competition affect RNAP allocation.

In Chapter 4 we study how a synthetic genetic oscillator is coupled to cell division and replication. We took advantage of a synthetic oscillator developed for *Escherichia coli* in the laboratory of Prof. J. Hasty at the University of California San Diego. We have shown that the bacterial cell cycle is able to partially entrain the synthetic oscillations consistently under normal growth conditions, by driving the periodic replication of the genes involved in the oscillator. We have also shown that synchronization between the two periodic processes increases when the synthetic oscillator is coupled back to cell cycle via the expression of an inhibitor of replication initiation. Additionally, we have developed a computational toy model that confirmed this effect.

Finally, in Part IV (Chapter 5) we summarize and discuss the main results presented in this Thesis, and suggest directions for future research.

# *Contents*

# *List of Figures*

# *List of Tables*

# *I*

# *Introduction*

# 1
# *Dynamical processes in cells*

On June 15 1878 a photographic experiment by E. Muybridge took place. Muybridge was commissioned by Leland Stanford (Governor of California, business magnate, founder of Stanford University and also a horse enthusiast) to demonstrate that a galloping horse lifts all four feet off the ground at some point during the gait, something impossible to distinguish for the human eye.

It took Muybridge several years to develop the photographic camera technology that made this experiment possible by dramatically reducing the exposure time needed (of the order of the minute in those days). Muybridge placed 12 of his state of the art cameras in line alongside the racetrack equidistant at 27 inches, and conceived a trip wire mechanism to shoot the cameras when the horse pulled the string during her race [Muybridge, 1957, Mitchell, 2001]. The result of this experiment is shown in Figure 1.1. These images can be considered the first time-lapse sequence of history, each frame being ~0.04 seconds apart.

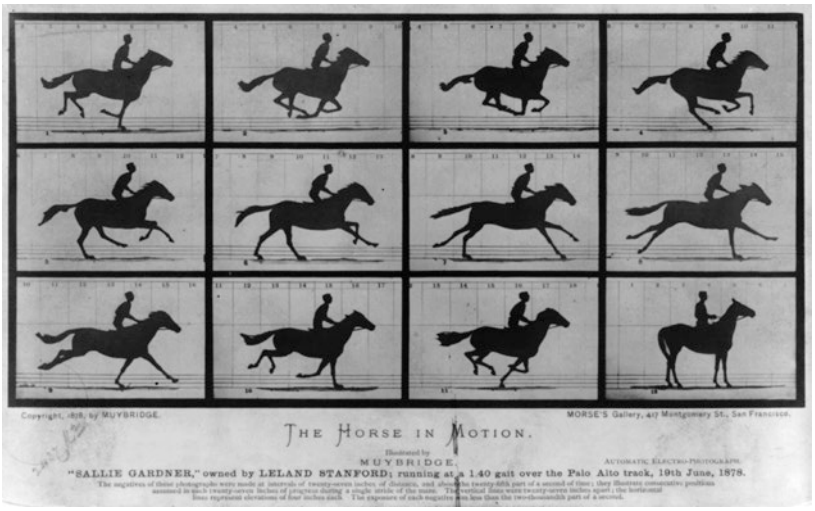


Figure 1.1: **The Horse in motion. "Sallie Gardner," owned by Leland Stanford; running at a 1:40 gait over the Palo Alto track, 19th June 1878.** Copyright, 1878, by Muybridge. This image has been downloaded from the United States Library of Congress's Prints and Photographs division (digital ID cph.3a45870).

Stanford obtained the proof he was looking for, and the world of arts and sciences experienced a tremendous revolution by the splitting of the second. Muybridge gave the world a taste of what would be invented in a few years time: the motion film. The horserace experiment was also

reported in the contemporaneous scientific journals *Scientific American* and the French *La Nature*. A new field of knowledge was born: the study of animal locomotion, in which scientists learnt how to use photographs as data, thus dissecting motion.

In biology, the first published time-lapse microscopy experiments date from the first decade of the 20th century [Coutu and Schroeder, 2013]. These movies tracked dynamical processes such as colony formation in the tunicate *Botryllus* [Pizon, 1905] or the fertilization and early development of sea urchins [Ries, 1909, Chevroton and Vles, 1909, Coutu and Schroeder, 2013][1]. However, details on inner cell structures were only visible by fixing and staining the sample, and this implied killing the specimen. The invention of phase contrast microscopy[2] in the 1930s allowed the visualization of these structures in living cells [Landecker, 2009].

But the major revolution in live cell imaging arrived in the 1990s with the cloning[3] of the jellyfish green fluorescent protein (GFP) [Prasher et al., 1992, Tsien, 2003], and the establishment of GFP as a potential marker for gene expression in living cells [Chalfie et al., 1994]. At that time, molecular cloning was developed enough to achieve portability across different organisms and also to monitor a wide variety of targets. The discovery of new fluorescent proteins with non-overlapping spectral emissions in the early 2000s [Matz et al., 2002, Zhang et al., 2002] allowed for simultaneous observation of different processes at a single cell level *in vivo*.

One striking application of fluorescent proteins in live cell imaging consists in tagging a protein with a fluorophore. In most cases, this protein fusion does not perturb the functionality of the tagged protein when expressed in cells, thus allowing the study of protein dynamics [Lippincott-Schwartz et al., 2001, Zimmer, 2002]. One example is the work done to track the dynamics of the tumour suppressor protein p53 and the oncogene Mdm2 in mammal cells [Geva-Zatorsky et al., 2006] (see Figure 1.2A).

Another use of fluorescent reporters is to establish the level of transcription of a specific promoter. This is particularly useful when studying the activity of regulatory genes, such as sigma factor $\sigma^B$ in *Bacillus subtilis*, responsible for triggering the cell's response to energy stress [Locke et al., 2011]. In this case, the activity of a $\sigma^B$ target promoter is a reporter of the state of a specific transcriptional program in the cell (see Figure 1.2B).

In conclusion, time-lapse fluorescent microscopy is a fairly recent technique that unveils for the first time dynamical processes inside the living cell. Quantification of these data, and a strong will to analyse the new observations in order to elaborate laws (or at least identify mechanisms) such as those found in exact sciences [Landecker, 2009] have led physicists to enter wet-labs.

A particularly interesting dynamical phenomenon, from a physical

[1] The earliest time-lapse sequences still preserved are at the Pasteur Institute. As explained in [Coutu and Schroeder, 2013], one of these movies is available in [Roux et al., 2004] as the supplementary movie 1.

[2] Phase contrast microscopy relies in the difference of phases that the electromagnetic wave experiences when it travels through different mediums, for instance, cells, organelles or culture media. This difference is due to variations in the velocity of light traveling through a transparent specimen and through the surrounding medium, which is in turn caused by changes in the refraction index [Ockenga, 2011].

[3] DNA cloning consists of inserting a DNA fragment containing a sequence of interest into a self-replicating DNA element (for instance, a plasmid). In this way, the cloned sequence will propagate together with the plasmid [Alberts et al., 2002]. The development of cloning techniques also contributed to further expanding the live cell imaging field. The first multipurpose cloning vector, pBR322, was designed and constructed in the late 1970s [Balbás et al., 1986, Sambrook et al., 1989].

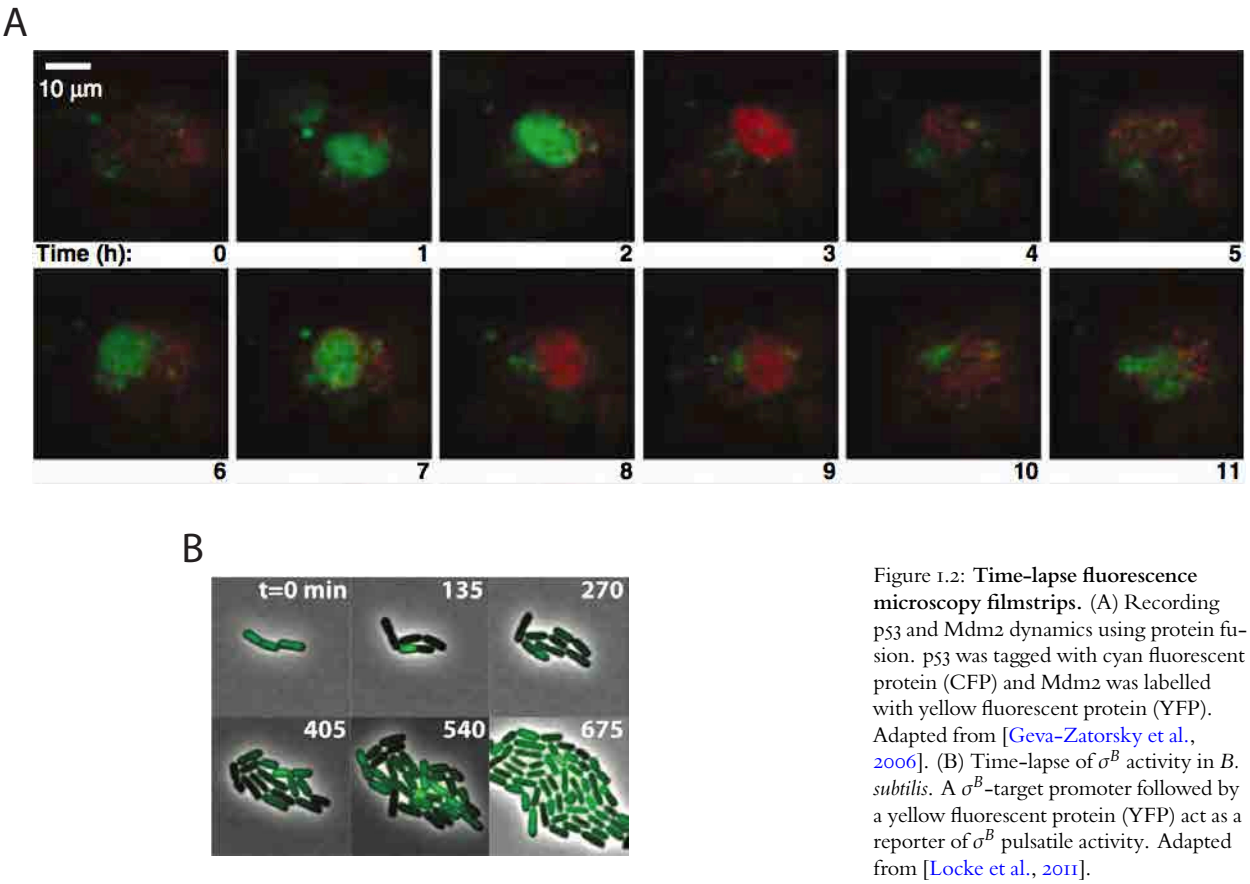


Figure 1.2: **Time-lapse fluorescence microscopy filmstrips.** (A) Recording p53 and Mdm2 dynamics using protein fusion. p53 was tagged with cyan fluorescent protein (CFP) and Mdm2 was labelled with yellow fluorescent protein (YFP). Adapted from [Geva-Zatorsky et al., 2006]. (B) Time-lapse of $\sigma^B$ activity in *B. subtilis*. A $\sigma^B$-target promoter followed by a yellow fluorescent protein (YFP) act as a reporter of $\sigma^B$ pulsatile activity. Adapted from [Locke et al., 2011].

point of view, is synchronization. As defined by [Pikovsky et al., 2003] synchronization is `an adjustment of rhythms of oscillating objects due to their weak interaction.` The phenomenon thus affects self-sustained oscillators that present a characteristic frequency, and the interaction between two of these autonomous oscillators must be weak enough so as not to end up with a new unified system that cannot be decomposed again.

Synchronization has been observed for centuries in living systems. One of the earliest documented examples in a large population of oscillating systems dates from the 17th century, when the physicist E. Kaempfer documented the spectacle of glowworms swarms flashing their tails simultaneously after his voyage to Siam [Pikovsky et al., 2003]. A.T. Winfree was a pioneer applying non-linear dynamical methods to the study of biological rhythms, especially studying circadian oscillators and heart beating [Winfree, 1967].

But it is thanks to time-lapse fluorescence microscopy that the observation of new complex dynamics within the cell brings up some challenging questions. Some examples are dynamical processes occurring in the form of periodic oscillations in the expression and/or activation of proteins. Genetic oscillators exhibiting different periods have been

reported: from circadian clocks responsible for inducing time-dependent behavior in cells and organisms with an approximated period of 24 hours, to ultradian oscillators that have periods of the order of a few hours. Circadian clocks have been found in a large variety of organisms, from bacteria and fungi to plants and animals [Young and Kay, 2001]. Of particular interest are the studies performed in cyanobacteria at the single cell level where the authors concluded that the strong temporal stability of the clock was due to the intracellular biochemical network, as the coupling between cells was negligible [Mihalcescu et al., 2004, Amdaoud et al., 2007]. Some examples of ultradian oscillators are the Zebrafish somitogenesis oscillator [Lewis, 2003], the Notch effector Hes1 [Monk, 2003, Tiana et al., 2007] and the transcription factor p53 [Monk, 2003, Geva-Zatorsky et al., 2006].

However more complex dynamics have been identified recently in the form of transient pulses occurring at random. This is the case for example of the master regulator of the competence state in *Bacillus subtilis*, ComK, in response to nutritional stress [Süel et al., 2006]. Another example of stochastic pulses in *B. subtilis* is the activation of the sigma factor $\sigma^B$ in response to energy stress [Locke et al., 2011]. In yeast, Crz1 presents bursts of localization in the cellular nucleus [Cai et al., 2008]. Even the regulation of pluripotency in stem cells follows a pulsing dynamics, as in the case of the Nanog transcription factor expression [Kalmar et al., 2009].

These types of dynamical processes do not occur in isolation in a cell but they do so simultaneously, and therefore it is necessary to establish the origin and level of coordination between them, their robustness to random fluctuations intrinsic to the cellular state and whether this coordination is actively or passively regulated. All these issues still remain unanswered.

The main object of this Doctoral Thesis is the study of the dynamical coupling between cellular processes, and how this coupling gives rise to a well-defined behavior in the presence of non-linearities and noise. We focus on the study of the origin and control of the coupling for two types of cellular dynamics: pulses of protein expression or activity on the one hand (Chapters 2 and 3), and periodic oscillations on the other (Chapter 4).

Specifically, in Chapter 2 we focus on how the coupling of certain inputs affect the response of the circuit regulating competence for DNA uptake in *B. subtilis*. In wild-type cells, under certain environmental stress conditions, competence has been found to follow a stochastic pulsing dynamics [Süel et al., 2006]. Here we study how the dynamical response of the competence circuit varies from excitable pulses to bistability and oscillations depending on the joint action of two coupled inputs applied to the system.

Still dealing with pulsing dynamics, in Chapter 3 we study the dynamical coupling between pulses of protein activity in single cells. For that purpose, we concentrated in the alternative sigma factors family in

*B. subtilis*. Sigma factors are proteins that reversibly bind to core RNA polymerase thus giving the formed holoenzyme promoter-recognition properties. As mentioned before, the alternative sigma factor $\sigma^B$ has recently been shown to hold a frequency-modulated pulsatile response to energy stress [Locke et al., 2011]. In this Chapter we show for the first time that several alternative sigma factors present stochastic pulses in their activation, and that these pulses take place in conditions of competition for core RNA polymerase. In the light of these results, we propose a new mechanism that allows sharing of the common limited resource (RNA polymerase) among the alternative sigma factors. To further understand this new mechanism we have developed and analysed several mathematical models.

Finally, in Chapter 4 we study how a synthetic genetic oscillator is coupled to cell division and replication. We took advantage of a synthetic oscillator developed in the laboratory of Prof. J. Hasty at the University of California San Diego [Stricker et al., 2008] for *Escherichia coli*. We quantified the degree of entrainment of the synthetic oscillator to bacterial cell cycle, and went one step further by back-coupling the chromosomal replication to the synthetic oscillator in order to test whether the two oscillators can mutually entrain their dynamics.

# *II*

# *Pulsatile behavior in stress-induced dynamics in bacteria*

# 2
# *Dynamics in competence*

Cells are usually subject to multiple simultaneous sources of biochemical and physical signals that provide them with information about their external environment and their internal state. Their adequate response to these external and internal conditions relies in the integration of the corresponding inputs. Previous efforts addressed at understanding signal integration in gene regulation have mainly concentrated on mapping the combinatorial response of bacteria to multiple environmental signals by measuring the expression of a single promoter [Kaplan et al., 2008, Krishna et al., 2009, Davidson et al., 2010, Hunziker et al., 2010, Silva-Rocha and de Lorenzo, 2011]. But in many instances different inputs act upon distinct nodes (genes or proteins) of the cell's underlying gene regulation network, and it is the network itself, not a particular promoter, that integrates the information at the system's level. It thus becomes necessary to understand how the integrated response of gene regulatory networks depends on the specific entry points of the inputs.

This Chapter is devoted to the study of the integrated response of the circuit regulating competence for DNA uptake in *Bacillus subtilis*. Specifically, we characterize the response of single cells *in vivo* to a combination of increased environmental stress that affects one of the two key competence genes, and a chemical signal controlling the constitutive expression of the other one of these genes. In order to quantitatively control the environmental stress acting upon the circuit, we used copy number variations of the gene affected by the stress. Quantitative time-lapse fluorescence microscopy shows that a variety of dynamical behaviors can be reached by the combination of the two inputs. An *in silico* bidimensional bifurcation analysis of a mathematical model of the circuit offers good quantitative agreement with the experimental observations, and sheds light on the dynamical mechanisms leading to the different integrated responses exhibited by the gene regulatory circuit.

## *2.1 The competence circuit in Bacillus subtilis*

Genetic competence is a well-defined cellular state that is triggered by nutrient starvation in *B. subtilis*. This state differs from the

vegetative state (characteristic of exponential growth) in the impairment of replication, and the development of the ability to uptake and process extracellular DNA. This is accomplished by the activation of a master transcription factor, ComK, that is responsible for the expression of over a hundred proteins that give rise to the new phenotypical state [Dubnau and Losick, 2006].

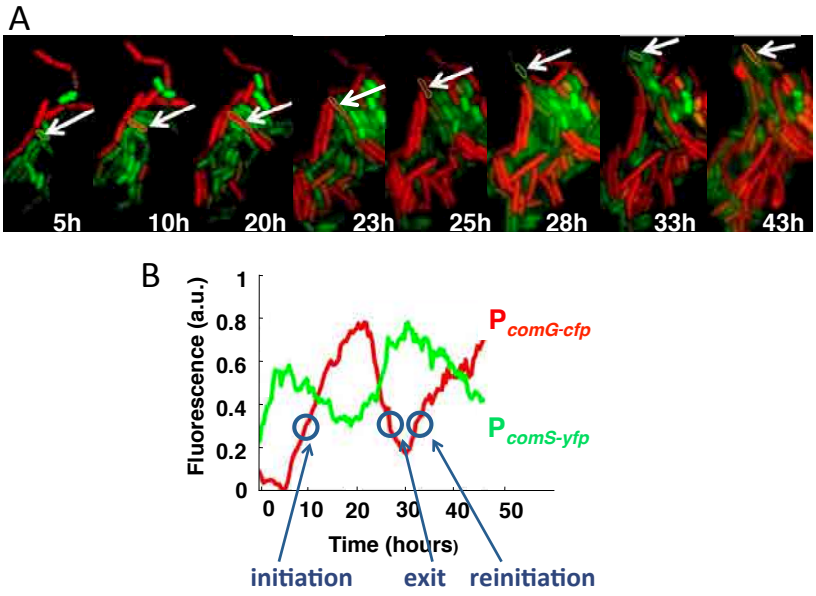


Figure 2.1: **Dynamical features of genetic competence.** (A) Typical filmstrip of a cell undergoing two consecutive competence events, as labeled by the activity of the *comG* promoter, regulated by ComK, controlling *cfp* expression (in red in the figure). The *yfp* signal, representing *comS* levels, is shown in green. (B) Time traces of *comG* and *comS* promoter activities for the cell highlighted in A. The conditions for this experiment are those of Figure 2.3C below. See Appendix A.1 for details of growth conditions and the microscopy procedures used. Adapted from [Espinar et al., 2013].

The competence behavior can be quantified with time-lapse fluorescence microscopy. Figure 2.1A shows a series of false-color snapshots of a *B. subtilis* microcolony subject to baseline stress conditions (see Appendix A.1 for details on cell culture and imaging under these conditions), with the activity of the ComK-regulated $P_{comG}$ promoter monitored by a cyan fluorescent protein (CFP), whose fluorescent emission is represented in red in the figure. The filmstrip shows that a fraction of cells in the microcolony differentiate into the competent state. In particular, the cell outlined in yellow undergoes two consecutive transient differentiation events in a time window of over 30 hours. Computing the mean cell fluorescence as a function of time, as shown in the red time trace of Figure 2.1B, we can quantify this behavior. In this way, a systematic monitoring of competence reveals that this process is strongly dynamic, and the nature of this dynamics totally depends on the inputs the competence circuit receives.

We can analyze the competence events in terms of their probability of initiation, exit and reinitiation (see Figure 2.1B).This statistical characterization represents an advantage of dynamic phenotypes over static cellular responses. Fluorescence measurements are not able to provide absolute values of expression levels, unless single molecules are detected [Cai et al., 2006]. However, transition probabilities are absolute by definition and are fairly straightforward to measure.

Another advantage of this system is that the gene regulatory circuit

that governs competence is well known and relatively simple. This makes competence an ideal model process for signal integration studies. Figure 2.2 shows a simplified scheme of the interactions between the two main components forming the circuit [Süel et al., 2006]. The master regulator of competence, ComK, is subject to a positive and a negative feedback loop. On the one hand, ComK directly activates its own transcription. On the other hand, it negatively regulates the expression of the stress sensor protein ComS, which promotes ComK activation by competitively binding to their common protease MecA [Süel et al., 2006]. This combination of a positive and a negative feedback loop gives rise to excitable behavior in the form of noise-driven ComK pulses, which are interpreted as functional competence events[1] [Süel et al., 2007].

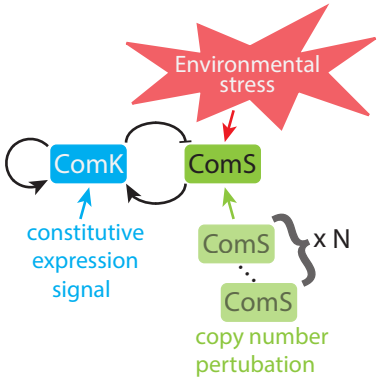


Figure 2.2: **Scheme of the circuit underlying genetic competence in *B. subtilis*.** The three types of inputs whose integration is considered in this work are also shown.

Previous work has shown that isolated perturbations of this circuit can lead to other dynamical regimes such as oscillations [Süel et al., 2007]. In this line, traditionally there has been a dichotomy in the interpretation of the competence dynamics in *B. subtilis*. Former studies at the level of single cells interpret wild-type competence as an excitable dynamics driven by noise [Süel et al., 2006, 2007]. However, other studies identify competence as a bistable phenomenon [Maamar and Dubnau, 2005]. Figure 2.3A and B shows how these two dynamics emerge in the wild-type case, depending on the intensity of environmental stress the cells are exposed to. In each panel, the left plot shows a collection of single-cell time traces of CFP levels quantifying the ComK-regulated $P_{comG}$ promoter, obtained by time-lapse fluorescence microscopy. The right plot shows histograms of CFP levels as measured from a typical instant in each time series analyzed. Finally, the insets display selected snapshots from these movies. Cells in Figure 2.3A were subject to baseline conditions of stress (see Appendix A.1), whereas cells in Figure 2.3B were exposed to harder stress conditions (that we called general stress conditions, see Appendix A.1). Hence, modifying the severity of environmental stress the competence circuit moves from one of these dynamical states to the other.

[1] From the biological point of view, we note that effective competence requires cells not only to turn on ComK expression, but also to turn it off eventually. Cells in which ComK expression is sustained die without dividing, and therefore without passing on to their progeny any advantage that might have been gained by incorporating exogenous DNA.

## 2.2 *Perturbing the competence circuit*

Here, we aim to characterize the response of the circuit to pairs of simultaneous perturbations, depending on their relative location within the circuit. We consider two types of inputs (Figure 2.2): (i) the constitutive expression level of one of the two main components of the circuit: ComK, and (ii) the intensity of the regulated (native) expression of the other one: ComS.

To control the constitutive expression of ComK, we used a strain containing one additional copy of this gene under the control of the isopropyl $\beta$-D-1-thiogalactopyranoside (IPTG)-induced hyperspank promoter, $P_{hyp}$ (see Appendix A.2 for a description of the strains used in this work). This strain also contains a reporter construct in which the $P_{comG}$

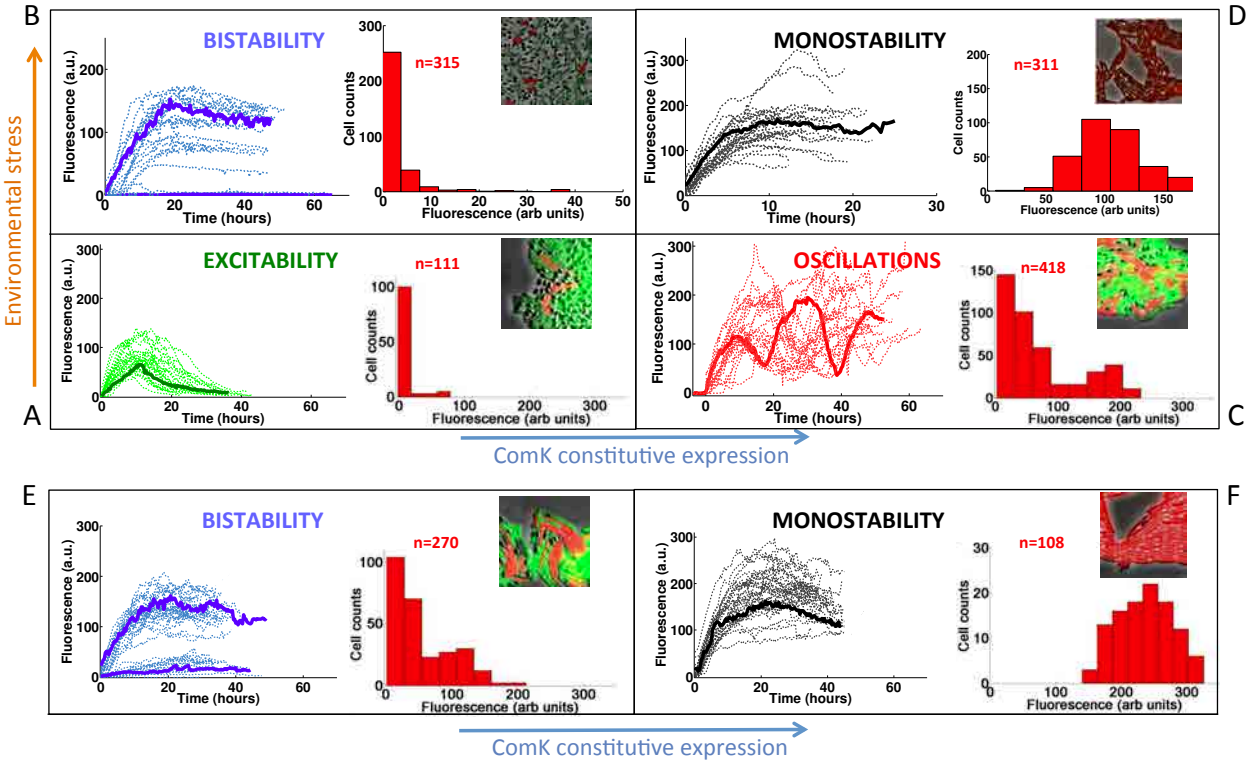


Figure 2.3: **Dynamical phenotypes arising from input integration.** The four upper panels correspond to joint variation of increasing environmental stress (increasing vertically toward the top) and the ComK constitutive expression level (increasing horizontally toward the right):(A) $\tilde{\alpha}_k = 1$, baseline stress conditions (see Appendix A.1 for details); (B) $\tilde{\alpha}_k = 1$, general stress conditions (see Appendix A.1 for details); (C) $\tilde{\alpha}_k = 3.2$, baseline stress conditions; and (D) $\tilde{\alpha}_k = 3.2$, general stress conditions. Strain V10 was used in panels (A) and (B), and strain Hyper-$\alpha$K was used in panels (C) and (D). The two lower panels correspond to a ComS high copy number situation: $\tilde{\beta}_s = 75$ (strain Hyper-$\alpha$K-75xS). Specifically, in (E): $\tilde{\alpha}_k = 1$ and $\tilde{\beta}_s = 75$; and in (F): $\tilde{\alpha}_k = 3.2$ and $\tilde{\beta}_s = 75$. They thus correspond to panels (B) and (D), but using here an increase in ComS copy number instead of real stress conditions. In each panel, the left plot shows single-cell time traces of CFP levels quantifying $P_{comG}$ activity, with a particular time trace highlighted with a thicker line, and the right plot presents histograms of CFP levels as measured from a typical frame in each movie analyzed (at an intermediate time, because at large times there is substantial death and sporulation in the system). Insets display selected snapshots from these movies. Adapted from [Espinar et al., 2013].

promoter drives the expression of *cfp* (Hyper-$\alpha$K strain, Table A.3). We explored five different IPTG levels, namely 0, 3, 5, 10, and 100 $\mu$M. In order to calibrate the promoter activities triggered by these IPTG values, we quantified the amount of fluorescence emitted by cells with a $P_{hyp}$-*yfp* reporter, where *yfp* accounts for yellow fluorescent protein (Control-$\alpha$ strain, Table A.3) for the same IPTG levels, and compared the measured values with the average signals obtained from a strain containing a $P_{comK}$-*yfp* reporter (KG strain, Table A.3) in cells not exhibiting competence. This comparison allowed us to establish the amounts of constitutive expression from the $P_{hyp}$ promoter for increasing IPTG, in units of the basal expression level of the $P_{comK}$ promoter, $\alpha_k^{wt}$ (see Figure 2.4 and Table A.4). In what follows we call this normalized value $\tilde{\alpha}_k$.

As mentioned above, the second input that we consider affects the strength of the regulated expression of ComS. Using general stress conditions we dramatically increase the stress intensity to which the cells are exposed to (with respect to baseline stress conditions), and we move the competence circuit from an excitable landscape to a bistable one (Figure 2.3A and B). However, general stress conditions do not allow for well-controlled experiments because these conditions produce systemic changes in the cells that alter their physiology in multiple ways, resulting in a high mortality rate and thus making data collection and reproducibility difficult to achieve. Therefore, to vary in a controlled way the strength of the regulated ComS expression, we used copy number

variations of this gene. Specifically, we introduced an additional copy of the *comS* gene (under the control of its native promoter) in two plasmids of different characteristic copy numbers (kindly provided by Beth A. Lazzazzera, UCLA): pHP13, which has a low and relatively stable copy number of ~ 6, and pDG148, with a larger copy number; and transformed the corresponding strains with each one of these two plasmids. To calibrate the actual copy number of these plasmids, we compared the fluorescence generated by cells containing the $P_{comS}$-*cfp* reporter in the pHP13 and pDG148 plasmids, with the signal produced by a strain in which a single copy of $P_{comS}$-*cfp* had been chromosomally integrated (Norm-$\beta$S strain) (see Table A.3 for strain information). Simultaneously quantifying the mean expression levels in these strains over long times using time-lapse microscopy, we could establish the copy numbers of these two plasmids at around 6.5 and 75, respectively (Figure 2.5). In this way, we were able to apply three different well established values of the maximum expression level of the $P_{comS}$ promoter with respect to its wild-type value. We denote this normalized quantity as $\tilde{\beta}_s$. We then included the multi-ComS plasmids in the Hyper-$\alpha$K strain described above, generating new strains (Control-$\beta$S-6xS and Control-$\beta$S-75xS, Table A.3) that allowed us to vary the two inputs simultaneously and independently in a totally controlled way.

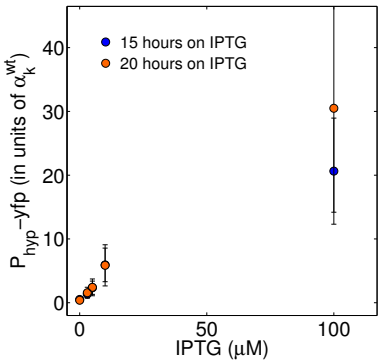


Figure 2.4: **Dose response of $P_{hyp}$-*yfp* to IPTG.** The plot shows $P_{hyp}$-*yfp* levels as a function of IPTG concentration. Fluorescence levels were measured at 15 and 20 h of growth on 1.5% (w/v) low melting agarose pads made with resuspension medium (RM) (Appendix A.1) and final IPTG concentrations of 0, 3, 5, 10 and 100 $\mu$M. As explained in the main text, $\alpha_k^{wt}$ accounts for the basal expression level of the $P_{comK}$ promoter, measured in the same conditions described here, with $P_{comK}$ driving the expression of *yfp*. From [Espinar et al., 2013].

## 2.3 *Phenotypic consequences of integration*

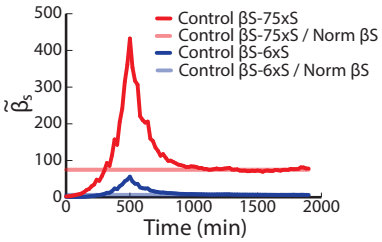


Figure 2.5: **Calibration of $P_{comS}$ promoter activity.** Continuous lines represent the normalized time traces obtained by dividing the mean fluorescence of the Control-$\beta$S-6xS ($n$ = 10, black) and Control-$\beta$S-75xS ($n$ = 15, red) strains respectively by that of the single-copy strain Norm-$\beta$S ($n$ = 10). Dashed lines represent the mean stationary values of these normalized traces, which are 6.46 and 74.97 for the pHP13::$P_{comS}$-*cfp* and pDG148::$P_{comS}$-*cfp* plasmids, respectively. From [Espinar et al., 2013].

FIGURE 2.3 SUMMARIZES THE PHENOTYPIC CONSEQUENCES of the integrated response of the competence circuit to the pairs of inputs described above. It shows single-cell data from the competence reporter $P_{comG}$-*cfp* for four selected combinations of each of the two input pairs considered. The upper panel (top two rows) shows results for the integration of the constitutive expression of ComK, $\tilde{\alpha}_k$, with an increasing environmental stress; whereas in the lower panel (bottom row) the latter is systematized by increasing the ComS copy number, $\tilde{\beta}_s$ (Figure 2.3E and F correspond to B and D situation).

In the upper panel, the environmental stress increases from bottom to top and the constitutive expression signal increases from left to right. In the lower panel, only the highest ComS copy number is considered. In each panel, the left plot contains single-cell time traces aligned so that competence turn-on (if it exists) occurs simultaneously in all traces. We have included cells representing all the different dynamical behaviors that we found in each case (except for cells that do not turn to competence in the excitable regime, represented by green time traces).

Input conditions for which the system is bistable lead to two types of behaviors, with some cells never entering competence and some others exhibited sustained expression of ComK for up to 40 hours, until either the cell dies or the movie ends. A histogram of CFP levels for all measured values at a typical instant of all movies analyzed (right plot in each panel of Figure 2.3) reveals a clear bimodality in the bistable regimes (panels B and E), which contrasts with the extremely weak bimodality of

the excitable regime (panel A) that is consistent with the low probability of competence of the wild-type cells. As explained at the beginning of this chapter, biologically speaking the functional competence requires cells to turn on ComK expression and also to eventually turn it off. In that way cells can keep on with replication after having been able to incorporate exogenous DNA, thus passing to their progeny any advantage they might have gained. In that sense, the only dynamical behaviors that maintain functional competence are excitability (panel A) and the oscillatory regime (panel C). In this latter case, cells are able to return to the vegetative state where they can divide before turning on ComK expression again. The remaining dynamical behaviors: bistability and certainly also monostability (panels D and F), eliminate effective competence.

A second phenotypic consequence of competence is to delay, but not eliminate, sporulation. Sporulation is another cellular differentiation response to stress in which the bacterium becomes dormant and waits for a potential improvement of the environmental conditions before germinating. Sporulation is known to be inhibited by ComK expression [Kuchina et al.], and thus when this expression occurs transiently (as in the excitable and oscillatory regimes), that fate is delayed but not eliminated. Similarly, bistability does not prevent sporulation, since in this regime a subpopulation of cells that do not express ComK exists, cells in this subpopulation are thus able to sporulate. The presence of spores in those regimes (excitability, bistability and oscillations) is evident in the microcolony snapshots shown as insets in the right-hand side of the corresponding panels of Figure 2.3. In the monostable regime, on the other hand, all cells in the population express ComK in a sustained way (see time traces and histograms in panels D and F), and as a consequence spores cannot be produced in this case, as is shown in the snapshots displayed in those panels.

## 2.4 *Statistical characterization of competence events*

In wild-type conditions, *B. subtilis* cells activate competence in a probabilistic and sparse manner, with less than 10% of cells in a microcolony exhibiting competence pulses at any given time as a response to stress [Dubnau and Losick, 2006]. As anticipated above, this behavior can be characterized statistically by computing the probabilities of several types of events associated with the pulses, such as their initiation, exit, and reinitiation within a certain time window after exit (Figure 2.1B). We systematically evaluated these probabilities under a combination of the two controlled inputs described above: ComK constitutive expression, $\tilde{\alpha}_k$, and ComS copy number, $\tilde{\beta}_s$.

Figure 2.6 summarizes our observed results for the integration of the constitutive expression of ComK, which determines the value of the parameter $\tilde{\alpha}_k$, with the copy number of ComS natural gene, which establishes in an integer manner the value of $\tilde{\beta}_s$. Three statistical observables are computed, namely the probabilities of competence initiation, $P_{init}$, of exit from competence, $P_{exit}$, and of competence reinitiation within a defined time window, $P_{reini}$[2].

[2] The probability of competence initiation ($P_{init}$) was determined as follows. Under baseline stress conditions (Appendix A.1), $P_{init}$ was defined as the number of competence initiation events divided by the total number of cell division events in a time window of ~140-150 minutes, characterised by increasing levels of $P_{comS}$-*yfp* (which ensures that the colony is under sustained growth conditions). The probability of competence exit ($P_{exit}$) was calculated as the fraction of competent cells that successfully leave the competence state. Finally, the probability of reinitiation $P_{reini}$ is defined as the probability that a cell that has successfully left competence state, goes back into that state after a fixed amount of time (we took this time to be equal to two cell cycles). Tables A.5 to A.7 present a summary of the statistics leading to the three probabilities measured experimentally for all input conditions.

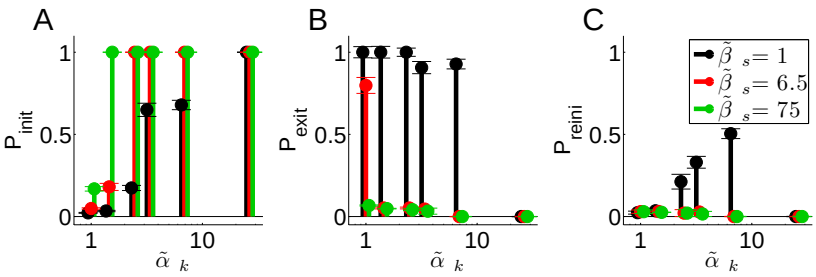


Figure 2.6: **Statistical analysis of competence dynamics in the presence of two inputs.** Different levels of induction for the constitutive expression of ComK and three different copy numbers of the natural ComS gene are considered: 1 (black), 6.5 (red), and 75 (green). The error bars are calculated via the standard deviation of the means taken in different movies. Adapted from [Espinar et al., 2013].

This statistical characterization shows distinct integration features depending on the pairs of inputs being applied to the circuit. More specifically, the probability of initiation, $P_{init}$, increases up to 100% (all cells undergo competence within a cell cycle) for increasing $\tilde{\alpha}_k$. But whereas that increase is smooth for low $\tilde{\beta}_s$, it becomes sharp and occurs earlier for high $\tilde{\beta}_s$ (Figure 2.6A). The exit probability, in turn, decreases abruptly in all cases for increasing $\tilde{\alpha}_k$ (Figure 2.6B). Finally, the probability of another competent event arising within one cell cycle after exit is only non-zero for intermediate values of $\tilde{\alpha}_k$ and small $\tilde{\beta}_s$ (Figure 2.6C).

## 2.5 *Dynamical characterization of competence events*

We can interpret the results in Section 2.4 in terms of dynamical behaviour. Table 2.1 summarizes the classification criteria we used in order to represent the different dynamical regimes occurring for varying values of the input pairs, as shown in the phase diagrams of Figure 2.7. In those diagrams, the different experimental regimes (classified according to the criteria listed above) are represented by means of symbols, for the quantitative well controlled input-integration experiments performed (see Figure 2.2). The shape and color of the symbols encode the dynamical regime. Green circles represent the wild-type excitable behavior exhibited by *B. subtilis* under baseline stress conditions [Süel et al., 2006]. Blue squares correspond to bistability, with the two states being the vegetative and the competent states. Black triangles denote monostable behavior in which competence is the only cellular state available to the cell. Finally, red diamonds mark the oscillatory behavior. The plots reveal distinct forms of integration in each case, according to the type of dynamical behaviors generated as the two inputs are varied in a coordinated way.

| **Dynamical regime** | **P**$_{init}$ | **P**$_{exit}$ | **P**$_{reini}$ | **Inputs** |
|---|---|---|---|---|
| Oscillations | Low-medium | High | High | $\tilde{\alpha}_k$ Medium |
| | | | | $\tilde{\beta}_s$ Low |
| Excitability | Low-medium | High | Low | $\tilde{\alpha}_k$ Low |
| | | | | $\tilde{\beta}_s$ Low |
| Bistability (steady) | Low-medium | Low | N/A | $\tilde{\alpha}_k$ Low |
| | | | | $\tilde{\beta}_s$ High |
| Monostability | High | Low | N/A | $\tilde{\alpha}_k$ High |
| | | | | $\tilde{\beta}_s$ High |

Table 2.1: **Dynamical classification of competence regimes.**

In particular, when ComK is varied constitutively (Figure 2.7), the bifurcation scenario is different between the independent applications of the two inputs, and also with respect to the integrated response. For instance, while the increase of ComS copy number leads to a transition from excitable to bistable behavior, incrementing only the constitutive expression of ComK (given a situation in which ComS copy number is low) generates oscillatory dynamics. These two scenarios are in turn different from the case of a joint increase of the two inputs, which leads to monostable competence for input levels that, when independently applied, result in either bistability or oscillations. Note that monostability is also the ultimate fate for extremely large levels of ComK constitutive expression, but it is substantially advanced by the joint action of the two inputs.

In order to understand the different response maps of the circuit for the two quantitative inputs, represented as symbols in the phase diagrams of Figure 2.7, we now focus on a mathematical model of the competence circuit. As mentioned at the beginning of Section 2.1,one of the advantages of competence is the good understanding of its underlying gene regulatory circuit, and consequently of a well-defined model of its dynamics. Previous investigations have shown that wild-type competence dynamics [Süel et al., 2006], and its response to single perturbations of the competence circuit [Süel et al., 2007] can be adequately described by the following two coupled ordinary differential equations (in dimensionless units):

$$\frac{dK}{dt} = \alpha_k + \frac{\beta_k K^n}{k_k^n + K^n} - \frac{K}{1+K+S} - \delta_k K \tag{2.1a}$$

$$\frac{dS}{dt} = \frac{\beta_s}{1+(K/k_s)^p} - \frac{S}{1+K+S} - \delta_s S \tag{2.1b}$$

where $K$ and $S$ represent the concentrations of ComK and ComS in the cell, respectively. In the first equation, the first term in the right-hand side ($\alpha_k$) represents the constitutive expression of the ComK gene. In wild-type cells, this promoter has a non-zero basal activity that we in-

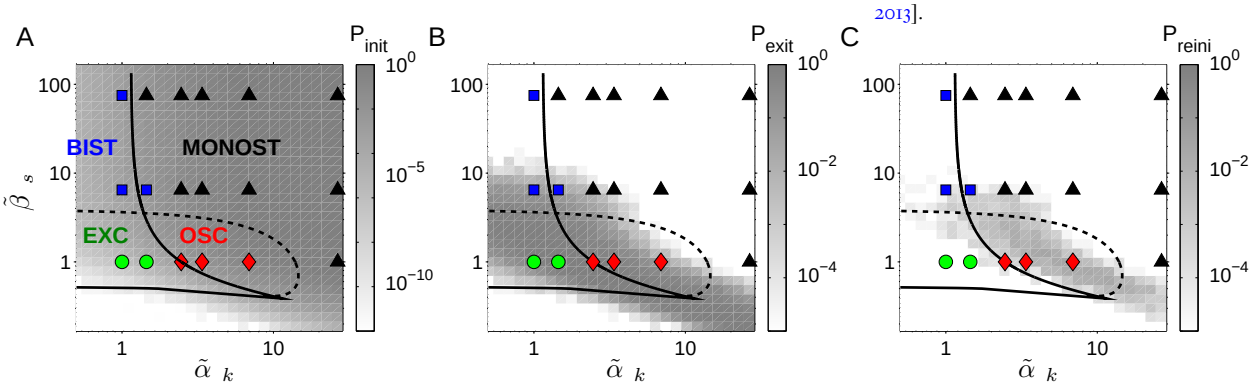


Figure 2.7: **Phase diagrams of the competence circuit corresponding to the joint variation of the constitutive expression of ComK, $\tilde{\alpha}_k$, and the ComS expression rate, $\tilde{\beta}_s$.** The symbols represent the experimental observations, with green circles corresponding to excitable dynamics (here defined by $P_{init} < 0.5$ and $P_{exit} > 0.85$), blue squares to bistable behavior ($P_{exit} < 0.85$ if $P_{init} < 0.5$: a fraction of the cells turn on competence and stay there, representative of spatial heterogeneity between two stable states; or $P_{exit} > 0.85$ if $0.5 < P_{init} < 0.95$: most cells turn on competence and come back, representative of temporal switching between two stable states). Black triangles denote monostable competence ($P_{init} > 0.5$ and $P_{exit} < 0.1$), and red diamonds oscillatory dynamics ($P_{reini} > 0.1$). Lines represent bifurcation boundaries of a deterministic mathematical model of the competence circuit (see text), as computed with the numerical continuation software AUTO through XPP; solid lines correspond to saddle-node bifurcations and dashed lines to Hopf bifurcations. The symbols and lines are the same among the three panels, which differ in the quantities plotted in grayscale, obtained from discrete simulations of the competence circuit: $P_{init}$ (A), $P_{exit}$ (B), and $P_{reini}$ (C). Parameters of the deterministic model are $\alpha_k^{wt} = 0.00035$, $\beta_k = 0.25$, $\beta_s^{wt} = 3$, $k_k = 0.2$, $k_s = 0.0625$, $\delta_k = \delta_s = 0.1$, $n = 2$, and $p = 5$. Remember that $\tilde{\alpha}_k = \alpha_k/\alpha_k^{wt}$ and $\tilde{\beta}_s = \beta_s/\beta_s^{wt}$. Parameters of the discrete model are given in Table A.2. Adapted from [Espinar et al., 2013].

crease in a controlled way in the Hyper-$\alpha$K, Hyper-$\alpha$K-6xS, and Hyper-$\alpha$K-75xS strains. The second term in the right-hand side represents the positive feedback of ComK activating its own transcription. In the second equation, corresponding to ComS, the first term accounts for the inhibition of ComS expression by ComK.

In both equations, the last two terms correspond to the competitive degradation of ComK and ComS by the common protease MecA [Süel et al., 2006] (second to last term) and a linear degradation term (last term).

The expression parameters $\alpha_k$, $\alpha_s$, and $\beta_s$ relate to their corresponding normalized values as follows: $\alpha_k = \tilde{\alpha}_k \cdot \alpha_k^{wt}$ and $\beta_s = \tilde{\beta}_s \cdot \beta_s^{wt}$. On the other hand, $\beta_k$ represents the maximum rate of regulated expression of ComK.

A stability analysis of the different fixed points exhibited by Eq.(2.1) establishes the various dynamical regimes that the circuit can exhibit, which can then be compared with the experimental results described above. The different regimes are separated by bifurcation points [Strogatz, 2000], which can be traced in two-dimensional parameter spaces such as the ones shown in Figure 2.7 by means of numerical continuation methods. This analysis allows us to establish different regions separated by bifurcation lines[3]. The solid lines in Figure 2.7 denote saddle-node bifurcations, in which an unstable and a stable fixed point are created, and the dashed lines correspond to Hopf bifurcations, in which a stable oscillation emerges [Strogatz, 2000].The distinct dynamical behaviors observed are labeled in the left panel of Figure 2.7. The experimental observations described above fit, represented by symbols, reasonably well with the theoretical expectations.

We now want to assess whether the good agreement between experiment and theory exhibited in Figure 2.7 depends on the criteria used to classify the dynamical behavior from the experimentally measured probabilities, defined in the caption of that figure. Modifications of these criteria do not change the results qualitatively, although they certainly affect some of the dynamical assignments, specially those close to the theoretical bifurcation lines. This is to be expected, since due to the existence of underlying biochemical noise, the boundaries defined by the bifurcation lines are smoothed out [Turcotte et al., 2008]. In order to evaluate the importance of this effect, we performed discrete simulations of the reactions underlying the deterministic model (Eq.(2.1)).The grayscale colormaps in Figure 2.7 represent the simulated values of the three event probabilities defined above: $P_{init}$ in panel A, $P_{exit}$ in panel B, and $P_{reini}$ in panel C. The results show that these probabilities vary smoothly across the deterministic bifurcation lines, whereas the deterministically predicted transitions are robust. Modifying the probability threshold values given in the caption of Figure 2.7 would change the way a simulation result is classified (falling within one dynamical regime or another), similarly to what would happen with the experimental results. These changes, however, do not alter the qualitative conclusions that can be extracted from the theoretical model, which provide an explanation

[3] The excitable region in Figure 2.7 panels is crossed by a saddle-homoclinic bifurcation line, not indicated in the plot, which separates a region of pure excitability for lower $\beta_s$, from a regime in which the excitable dynamics coexists with a limit cycle for higher $\beta_s$. This limit cycle disappears at the Hopf bifurcation denoted by the dashed line. We have not included this bifurcation line in the plots because given the presence of noise, which destabilizes the limit cycle, the two regimes are biologically indistinguishable. Note that plots consider $\tilde{\beta}_s$ and that $\beta_s \propto \tilde{\beta}_s$.

for the distinct integration responses of the circuit to different input pairs, in terms of the diverse bifurcation scenarios triggered by the various inputs.

## 2.6 Discussion

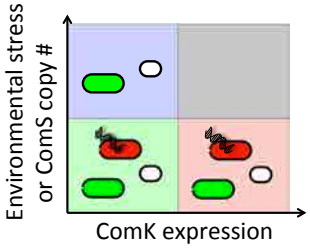


Figure 2.8: **Schematic summary of the input integration observed experimentally.** Background colors have the same meaning as in Figure 2.3 and 2.7. Additionally, green cells denote vegetative cells, red cells represent functional competence, and white spots represent spores. Adapted from [Espinar et al., 2013].

These results show that the integrated response of the inputs considered in this work is functionally very different from the effect of each input acting individually (Figure 2.8). In particular, although no single input prevents sporulation or normal vegetative growth *per se*, their combination eliminates these two cellular states.

In this work we have considered three inputs of different nature. The first one corresponds to a (continuously controllable) level of constitutive expression of one of the two fundamental genes of the competence circuit, ComK. In a realistic biological setting, this input could correspond to a contextual signal such as those affecting signaling pathways in developing organisms [Artavanis-Tsakonas et al., 1999]. The effects of such contextual signals is beginning to be studied systematically in small developmental networks [Cotterell and Sharpe, 2010].

The second input consists in increasing the environmental stress that *B. subtillis* cells are exposed to, as it directly affects the other main gene of the competence circuit: ComS [Grossman, 1995]. For this purpose, we let cells grow in a nutrient limited medium and then used conditioned media containing general stress signals. As a result, the excitable regime becomes bistable, and the oscillatory regime becomes monostable. It is noteworthy that the results obtained in the wild-type case might help explain why certain studies identify competence as a bistable phenomenon [Maamar and Dubnau, 2005], whereas others interpret it as an excitable dynamics [Süel et al., 2006]: the system responds in one way or the other depending on the specific stress conditions of the medium.

However, these general stress conditions produce systemic changes in the cells that alter their physiology in multiple ways, thus preventing a full control of the experiments. To address this issue, the third input takes the form of multiple (discrete) copies of the gene affected by the environmental stress (ComS) retaining their native regulation. This input allows us to vary in a controlled way the strength of the regulated response of ComS, thus mimicking real stress conditions, but without the disadvantage of any other undesired collateral effect. Again, if we consider this input in a realistic biological context, it would correspond to copy number variations such as those being extensively studied in recent years in the human genome [Conrad et al., 2010] and yeast [DeLuna et al., 2008, Gruber et al., 2012], among other organisms.

Even though the interplay between the two levels of cellular control exposed here (a contextual signal on the one hand, and copy number variations on the other one) is crucial for the correct functioning of cells, little is know about their integration. By systematically exploring the integration of contextual and genomic inputs, studies such as the one

described here should help shed light on the relation between structure and function in cellular networks.

The physiological effects reported here are caused by changes in the dynamical behavior of our genetic circuit. Functional consequences of dynamics have also been reported in mammalian cells [Ashall et al., 2009, Purvis et al., 2012]. While recent studies have systematically addressed the effect of individual stimuli on dynamical behavior at the single-cell level [Ashall et al., 2009, Batchelor et al., 2011], here we have considered the effects of combining two inputs. In that sense, our study is a dynamical generalization of more "classical" epistasis studies addressing the effect of combinations of genetic perturbations on cell growth [Segre et al., 2005] or the evolution of resistance under drug interactions [Michel et al., 2008]. In our case, the use of dynamical phenomena (in the form of transient activation of a cellular differentiation program) allows us to define observables that that do not depend on arbitrary factors associated with the measurement process (in our case fluorescence detection from populations of fluorescent proteins that are not monitored at the single-molecule level). Furthermore, this study was developed using well-controlled input signals that were quantitatively normalized with respect to appropriate reference strains. These facts allow for an objective comparison with a theoretical model of the competence circuit, which brings us closer to a quantitative understanding of the biology [Garcia and Phillips, 2011, Garcia et al., 2011] underlying bacterial stress response. This approach could in principle be extended to other gene regulation networks in higher organisms.

# 3
# *Dynamics in sigma factors*

In Chapter 2 we saw how coupling different inputs in *Bacillus subtilis* resulted in the emergence of different dynamical behaviors. In particular, we saw how the state of competence can be described as stochastic pulses events of the competence master regulator, ComK, expression under certain conditions. In this Chapter we deal with pulsatile dynamics again, but this time we study the dynamical coupling between pulses of protein activity inside a single cell. To that end, we have focused in the sigma factors family in *B. subtilis*. In eubacteria, sigma factors are proteins that bind reversibly to core RNA polymerase (the enzyme responsible for gene transcription), conferring on it promoter recognition specificity. This allows for a high level of transcription control in response to several environmental stresses and other stimuli [Helmann and Chamberlin, 1988, Gruber and Gross, 2003]. In a recent work, Locke *et al.* [Locke et al., 2011] observed the activation of the sigma factor $\sigma^B$ in response to energy stress in individual *B. subtilis* cells. They described a frequency-modulated pulsing response of $\sigma^B$, whose frequency increased with the level of stress.

In collaboration with Prof. Michael Elowitz's lab from the California Institute of Technology, we analyzed the dynamics of sigma factor activity in individual *B. subtilis* cells using time-lapse fluorescence microscopy. We saw that under stationary phase stress conditions, several different alternative sigma factors exhibit pulsatile activation. Then, systematizing the energy stress applied to cells using micophenolyc acid (MPA, a drug that reduces cellular ATP levels [Zhang and Haldenwang, 2005, Locke et al., 2011]), we proceeded to further characterize these pulses. We saw that seven alternative sigma factors presented stochastic pulses in their activation of about 1 hour of duration. These pulses occurred in an asynchronous manner under conditions of competition for core RNAP. These results suggest that sigma factors take turns in order to use core RNA polymerase ("time-sharing") being only one or a few sigma factors active at the same time in a given cell.

Time-sharing is a general strategy used in engineering to share a limited resource between multiple users. One example is the time-division multiplexing (TDM) protocol used in today's digital telephony. TDM transmits and receives multiple independent signals using the same

wire at the same time by dividing the signal into many segments. At the reception, each signal will show in the line only a fraction of time in an alternating pattern [Decina and Rossi, 1980].

Because core molecular components are often available in limited quantities in cells, time-sharing could be a widespread mechanism for the sharing of core components in other genetic regulatory circuits.

In order to better understand how sigma factors interact, we propose three mathematical models that show how time-sharing can emerge either from simple noise driven pulse-generating gene circuits, either from a limit cycle model, but in all cases competing for limiting amounts of core RNAP.

## *3.1 Sigma factors in Bacillus subtilis*

In bacteria, alternative sigma factors reversibly bind to the core RNA polymerase (RNAP) conferring the formed holoenzyme with specific promoter-recognition properties [Losick and Pero, 1981, Helmann and Chamberlin, 1988, Gruber and Gross, 2003] (see Figure 3.1 A). Prokaryotes have one house-keeping sigma factor and then a variable number (that depends on the specific type of bacteria) of alternative sigma factors that trigger specific transcriptional programs in response to particular stress conditions, growth transitions, and morphological changes [Gruber and Gross, 2003]. In particular, *B. subtilis* has 18 different sigma factors [Gruber and Gross, 2003] (see Table 3.1, Figure 3.1 B).

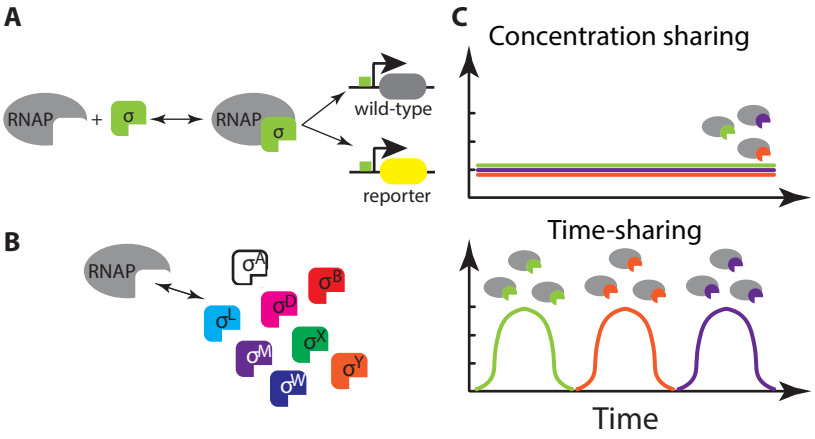


Figure 3.1: **Sigma factors share core RNAP.** (A) Alternative sigma factors reversibly bind to RNAP giving the holoenzyme promoter-recognition specificity. We used this property to build reporter strains in which a promoter specifically activated by one sigma factor controls the expression of a fluorescent protein. (B) We studied a subset of *B. subtilis* alternative sigma factors not involved in sporulation that share core RNAP. (C) RNAP sharing can be achieved mainly by two mechanisms: by equitably distributing RNAP between all the sigma factors present in the cell ("concentration sharing"); or by sigma factors taking turns to use most of the available RNAP ("time-sharing"), being only one or a few sigma factors active at the same time in an individual cell.

Hitherto the only considered mechanism that allow sharing of a common limited resource as is RNAP for the cell, is to distribute RNAP molecules equitably between all the sigma factors expressed in the cytoplasm ("concentration sharing"). In this work, we propose a different mechanism that consists in sigma factors taking turns to use most of the available RNAP at once ("time-sharing"), so that in a single cell only one or a few sigma factors are simultaneously active (see Figure 3.1 C). Despite time-sharing strategies have been studied in other contexts (for

| $\sigma$-factor | Function | References |
|---|---|---|
| $\sigma^A$ | House keeping | [Helmann and Chamberlin, 1988] |
| $\sigma^B$ | General stress response | [Gruber and Gross, 2003, Paget and Helmann, 2003, Hecker et al., 2007] |
| $\sigma^D$ | Flagelar synthesis | [Paget and Helmann, 2003] |
| $\sigma^E$ | Sporulation | [Gruber and Gross, 2003, Paget and Helmann, 2003] |
| $\sigma^F$ | Sporulation | [Gruber and Gross, 2003, Paget and Helmann, 2003] |
| $\sigma^G$ | Sporulation | [Gruber and Gross, 2003, Paget and Helmann, 2003] |
| $\sigma^H$ | Sporulation initiation | [Gruber and Gross, 2003, Kroos and Yu, 2000] |
| $\sigma^I$ | Heat-shock or nutritional stress | [Zuber et al., 2001, Asai et al., 2007, Tseng and Shaw, 2008] |
| $\sigma^K$ | Sporulation | [Gruber and Gross, 2003, Paget and Helmann, 2003] |
| $\sigma^L$ | Cold-shock adaptation, amino acid catabolism | [Wiegeshoff et al., 2006, Zellmeier et al., 2005] |
| $\sigma^M$ | Osmotic stress response | [Gruber and Gross, 2003, Hecker et al., 2007] |
| $\sigma^O$ | Regulation of oxalate decarboxylase expression by acid stress | [MacLellan et al., 2009] |
| $\sigma^V$ | Cell wall protection | [Helmann, 2002, Zellmeier et al., 2005] |
| $\sigma^W$ | Cell wall stress response, antibiotic response | [Gruber and Gross, 2003, Hecker et al., 2007] |
| $\sigma^X$ | Modulatory role in cell envelope, antimicrobial response | [Gruber and Gross, 2003, Zellmeier et al., 2005] |
| $\sigma^Y$ | Nitrogen starvation response | [Helmann, 2002, Zellmeier et al., 2005, Tojo et al., 2003, Cao et al., 2003] |
| $\sigma^Z$ | Unknown | [Helmann, 2002, Luo et al., 2010] |
| YlaC | Oxidative stress response | [Helmann, 2002, Luo et al., 2010, Matsumoto et al., 2005] |

Table 3.1: ***Bacillus subtilis* sigma factors.**

instance in telecommunications as explained in the introduction of this Chapter), examples of time-sharing in cells have not been reported so far.

Most alternative sigma factors are typically co-transcribed with their cognate anti-sigma factor. This protein prevents the association between the sigma factor and the core RNAP, and can be inhibited by different signals (stress for instance), thus enabling sigma factor activation [Gruber and Gross, 2003].

In a recent work, Locke *et al.* [Locke et al., 2011] observed the activation of the sigma factor $\sigma^B$ in response to energy stress in individual *B. subtilis* cells. They described a frequency-modulated pulsing response of $\sigma^B$, with frequency increasing with the level of stress. These pulses represent $\sigma^B$ molecules becoming simultaneously active by binding to RNAP and thus initiating transcription of target genes. Pulses terminate when $\sigma^B$ releases RNAP, resulting in the deactivation of $\sigma^B$ molecules.

However, dynamics of other sigma factors have not been reported so far. Hence it is unclear whether pulsing is specific of $\sigma^B$ or occurs more generally among alternative sigma factors, whether multiple sigma factors pulse under the same conditions, and how pulsing affects RNAP sharing.

To address these questions, we constructed a set of reporter strains consisting in promoters specifically activated by each one of the *B. subtilis* sigma factors not involved in sporulation, controlling the expression of a fluorescent protein (see Figure 3.1 A and Figure 3.2).

Under general stress conditions (using stationary phase conditioned media, see in Appendix B.2.2) we saw pulsatile activation for the 6 sigmas studied (these were, $\sigma^B$, $\sigma^D$, $\sigma^M$, $\sigma^W$, $\sigma^X$, and $\sigma^Y$), see Figure 3.3. As discussed in Chapter 2, the magnitude of stress applied to *B. subtilis* using stationary phase conditioned media affects the physiology of cells in several aspects, dramatically increasing the mortality rate and thus obstructing proper data acquisition. For this reason, we used mycophenolic

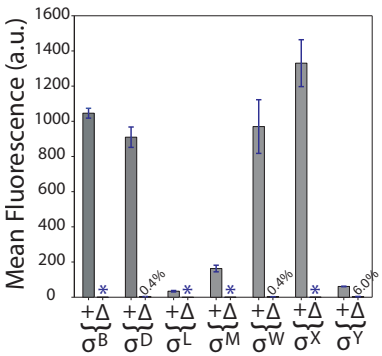


Figure 3.2: **Each sigma factor reporter strain is activated specifically by its corresponding sigma factor.** Each sigma factor reporter strain consists of a promoter activated by the corresponding sigma factor controlling the expression of a yellow fluorescent protein (YFP). In this experiment, each reporter strain was grown in the presence of 40 $\mu$g/ml mycophenolic acid (MPA, a drug that reduces cellular ATP levels and allows to mimic energy stress conditions [Zhang and Haldenwang, 2005, Locke et al., 2011]) considering two different genetic backgrounds: (+) indicates that the considered sigma factor is in the genome; (Δ) denotes that the considered sigma factor is knocked out. Each bar is the average of the 2 independent experiments, where for each experiment the average fluorescence of at least 300 cells was taken. The shown percentages are the fluorescence signal in the knockout strain relative to signal in the original reporter strain. Asterisks indicate measurements for which the fluorescence signal obtained is indistinguishable from autofluorescence. Error bars represent SEM. Adapted from J.C.W.Locke and J.Park [Locke et al., 2014].

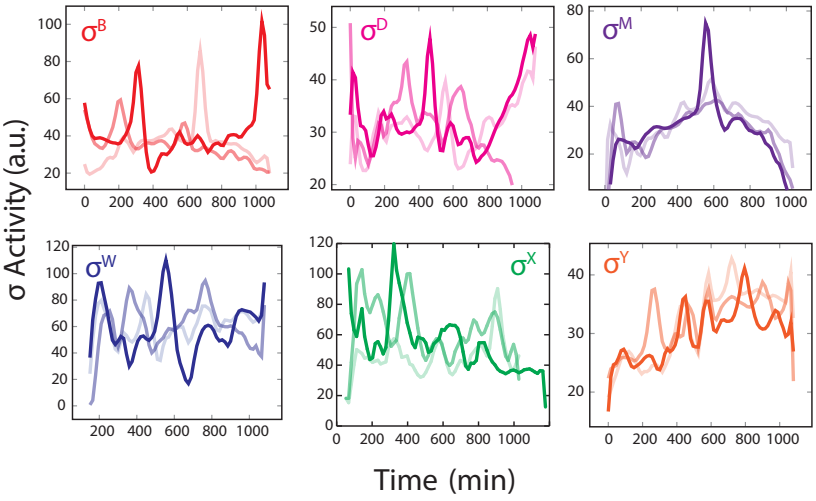


Figure 3.3: **Several sigma factors pulse under stationary phase conditions.** Alternative sigma factor reporter strains were grown separately in stationary phase conditioned media. Each panel shows 3 representative time traces of a lineage with pulsatile dynamics. Adapted from [Locke et al., 2014].

acid (MPA) (a drug that reduces cellular ATP levels) to mimic energy stress conditions, avoiding undesired systemic effects of stationary phase stress. Working with MPA also allows a proper control of the intensity of the applied stress. All the characterization experiments were performed with this drug, at the given concentrations.

## 3.2 *Characterization of individual dynamics of sigma factors*

We proceeded first to characterize the pulses growing the reporter strains individually in a minimal medium containing 40 $\mu$g/ml MPA. Using time-lapse fluorescence microscopy and quantitative image analysis we tracked sigma factor activities over time in single cells.

To quantify sigma factor activity instead of sigma factor abundance, we computed the promoter activity as in [Locke et al., 2011][1]. This activity is an indicator of the rate at which free sigma factor can associate with available RNAP and start transcription at target promoters. Given that sigma factors can be sequestered by their cognate anti-sigma factor (thus preventing the formation of the sigma-RNAP holoenzyme), the promoter activity depends on the levels of sigma factor protein, anti-sigma factor, and the availability of RNAP inside the cell.

This analysis revealed that seven sigma factors ($\sigma^B$, $\sigma^D$, $\sigma^L$, $\sigma^M$, $\sigma^W$, $\sigma^X$, $\sigma^Y$) showed pulsatile activation under constant conditions (see Figure B.1). Pulses had a typical duration of ~ 1 hour (Figure 3.4 A), showed similar amplitude distributions between different sigmas (Figure 3.4 B), and ocurred at frequencies ranging from $0.06 \pm 0.01$ h$^{-1}$ for $\sigma^X$ to $0.13 \pm 0.02$ h$^{-1}$ for $\sigma^D$ (Figure 3.4 C). In our experimental conditions, the cell cycle had a duration of $\sim 1.9 \pm 0.2$ h. This means that pulses occur from once every 8.3 cell cycles to once every 3.5 cell cycles. No significant correlations were observed in sister cell pairs (Figure B.2),

[1] Briefly, taking the total fluorescence per cell and considering the production, degradation, dilution and photobleaching rates of the fluorescent protein we can establish that its production rate is given by the following ODE:

$$P(t) = \frac{dF(t)}{dt} + \gamma \cdot F(t)$$

where $F(t)$ is the total fluorescence and $\gamma$ combines the degradation, dilution and photobleaching processes. In order to avoid the dependence of $P(t)$ on segmentation errors, we can rewrite $F(t)$ in terms of the cell's mean fluorescence ($M(t)$) multiplied by the cell's area (as a good approximation it is given by $L(t) \cdot W(t)$, this is, the cell length multiplied by its width; note that in *B. subtilis* $W(t) \approx W_0$),

$$F(t) = W_0 \cdot L(t) \cdot M(t)$$

Replacing $F(t)$ in the expression for $P(t)$ we obtain:

$$\tilde{P}(t) = \frac{P(t)}{W_0 L(t)} = (\mu(t) + \gamma) \cdot M(t) + \frac{dM(t)}{dt}$$

Where $\tilde{P}(t)$ can be interpreted as the production rate per chromosomal equivalent (allowing comparison of production rate throughout all instants of the cell cycle), and $\mu(t) = \frac{d \log L(t)}{dt}$ defines the cell's instantaneous growth rate. From [Locke et al., 2011]. We set $\gamma = 0.05$ to avoid non-physical negative values of promoter activity due to bleaching of fluorescent proteins during movies.

or between a parent cell and its two daughters (Figure B.3), suggesting that pulses are generated stochastically.

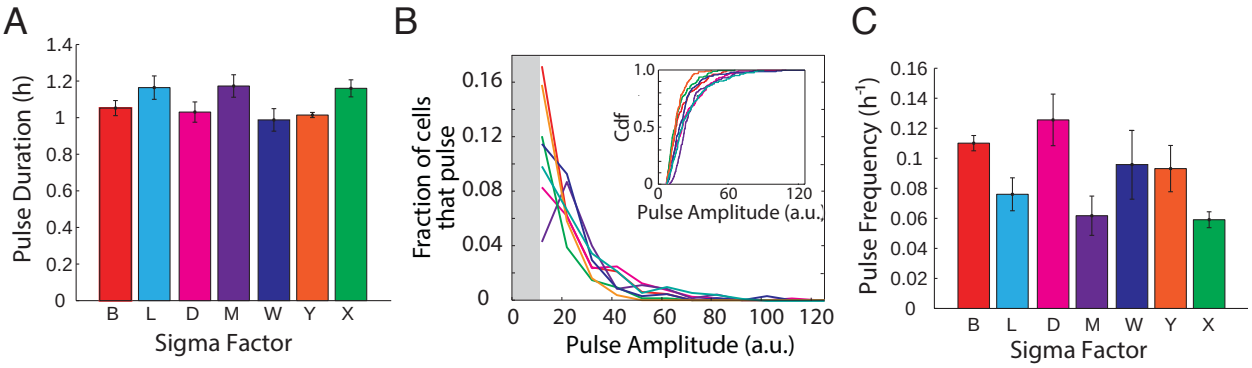


Figure 3.4: **Individual characterization of pulses.** Reporter strains were analyzed under 40 $\mu$g/mL MPA energy stress conditions. Panels show (A) the obtained mean pulse durations, (B) histogram of pulse amplitudes (gray shading indicates the amplitude detection cutoff; the inset shows the cumulative distribution functions), and (C) mean pulse frequencies. Error bars denote the mean ± SEM. From J.C.W.Locke and J.Park [Locke et al., 2014].

It is noteworthy that the housekeeping factor $\sigma^A$, which does not have an associated anti-sigma factor and presents a higher affinity for RNAP [Maeda et al., 2000], showed a more homogeneous activation with no pulses (see Figure 3.5).

## 3.3 *Characterization of collective dynamics of sigma factors*

In order to establish whether alternative sigma factors pulse in a synchronous or an asynchronous form, we chose 5 of the best-characterized pulsatile sigma factors ($\sigma^B$, $\sigma^D$, $\sigma^M$, $\sigma^W$, and $\sigma^X$) and constructed a "matrix" of strains containing pairwise combinations of these sigma factor reporters.

Specifically, each strain contained a cyan fluorescent protein (CFP) reporter for a sigma factor and a yellow fluorescent protein (YFP) reporter for another sigma (Figure 3.6 A). The matrix also considered the "diagonal" case, where CFP and YFP reported the activity of the same sigma factor. This allowed us to establish an upper limit for possible correlations. As expected, diagonal strains showed strong positive correlations in snapshots experiments (see Appendix B.2.4), despite intrinsic noise in gene expression and measurement errors that tend to reduce correlations [Elowitz et al., 2002]. On the other hand, off-diagonal strains (that contain reporters for different sigma factors) show little or no correlation (see Figure 3.6 B,C). These results would be in agreement with the hypothesis that sigma factors pulse in an asynchronous manner.

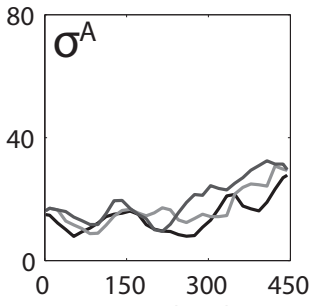


Figure 3.5: **Housekeeping factor $\sigma^A$ does not pulse.** Activity time traces for the housekeeping factor $\sigma^A$ under 40 $\mu$g/mL MPA energy stress conditions. Traces show the homogeneous (non-pulsing) activation of $\sigma^A$ in 3 different cell lineages. Adapted from J.C.W.Locke and J.Park [Locke et al., 2014].

Previous studies in *E.coli* and *B.subtilis* reported that under certain conditions alternative sigma factors can compete for a limited pool of core RNAP [Grigorova et al., 2006, Maeda et al., 2000, Hicks and Grossman, 1996]. To better understand whether competition plays a role in this system, we engineered a strain in which levels of constitutive $\sigma^B$ could be controlled. This strain lacked the wild-type $\sigma^B$ operon and also contained a copy of the $\sigma^B$ gene controlled by the inducible $P_{hyp}$ promoter introduced in Section 2.2 above and a YFP reporter for $\sigma^W$

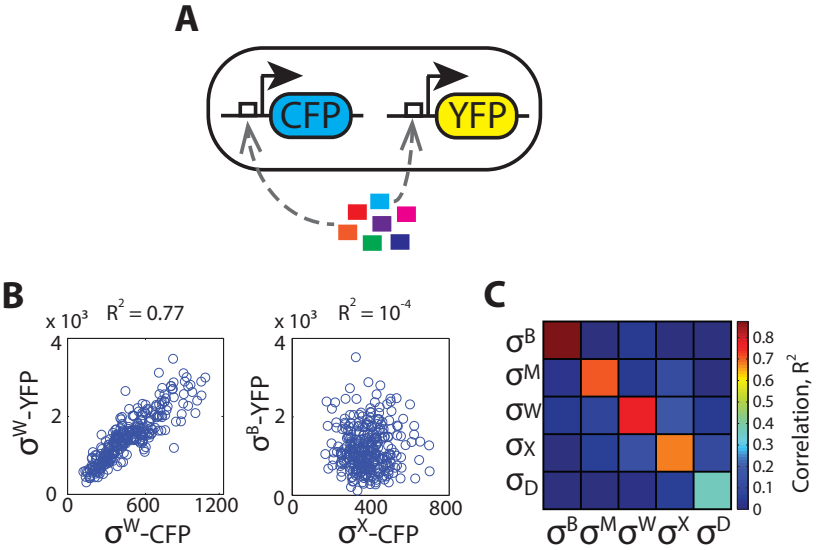


Figure 3.6: **Correlations for alternative sigma factor pulses.** (A) Each strain in the matrix contains two sigma factor reporters, expressing CFP and YFP, both chromosomally integrated. (B) Distributions of gene expression for the corresponding strains were taken after 180 min of growth in SMM liquid culture with 40 $\mu$g/mL MPA. Each point represents the two fluorescence intensities of a single cell. Left panel shows results for one strain in the diagonal and it is noteworthy the high level of correlation. Right panel shows results for one off-diagonal strain where no significant correlation was found. (C) Heatmap showing the degree of correlation between sigma factors pairs for all strains analyzed. (B) and (C) adapted from J.C.W.Locke and J.Park [Locke et al., 2014].

(Figure 3.7 A). Next, using fluorescence microscopy we quantified the effect of varying the constitutive expression of $\sigma^B$ on $\sigma^W$ activity. Specifically, we found that $\sigma^W$ activity was reduced proportionally to the level of induction of ectopic $\sigma^B$ (see Figure 3.7 B). It is noteworthy that $\sigma^W$ activity is also prevented even at $\sigma^B$ activation levels comparable to those obtained in standard pulsing activity of wild-type cells.

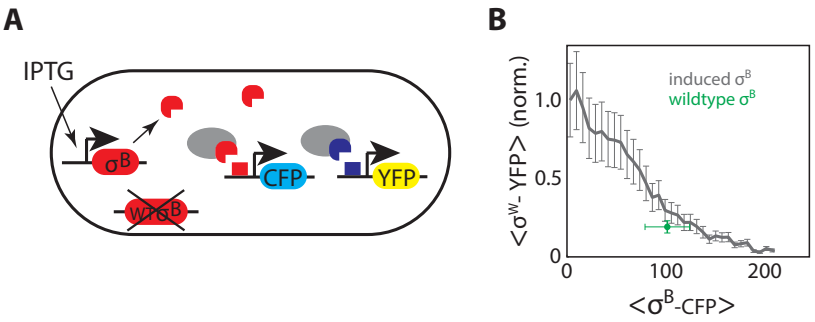


Figure 3.7: **Sigma factors competition.** (A) Strain used for the competition experiment. The $\sigma^B$ operon was knocked out and replaced with an IPTG-inducible promoter controlling the expression of $\sigma^B$. This strain also contained a chromosomally integrated CFP reporter for $\sigma^B$ activity and a chromosomally integrated YFP reporter for $\sigma^W$ activity. See Appendix B.1 for strain list and full description. (B) Ectopic expression of $\sigma^B$ showed dose-dependent inhibition of $\sigma^W$ activity (wild-type case is drawn with a green dot). Error bars represent SEM. (B) Adapted from J.C.W.Locke and J.Park [Locke et al., 2014].

## 3.4 Modelling sigma factor pulses

To understand how pulsing and competition together affect the sharing of the RNAP we developed several mathematical models, of which we explain here the most relevant ones.

All the models described here incorporate the most common features among the different alternative sigma factors gene regulatory networks. These common features are: transcriptional autoregulation (the sigma factor and its cognate anti-sigma are expressed from the same operon, which is activated by its own sigma factor), inhibition by the co-expressed anti-sigma factor, and limiting levels of RNAP resulting in competitive binding between sigma factors (this assumption is supported by results shown in Figure 3.7B).

### 3.4.1 Ultrasensitivity model

Molecular titration is a regulatory mechanism by which an active protein is sequestered by a repressor forming an inactive complex. As described in [Buchler and Louis, 2008] this mechanism can generate ultrasensitive responses where a small fold change in the input (for instance, the number of molecules of a certain species) is amplified to a large fold change in the output (following the previous example, that would be the number of molecules of another species in the system). A reasonable assumption when modeling sigma factors is to consider that there is a tight binding between the sigma factor ($S$) and its cognate anti-sigma ($A$) (this is the case for instance of the switch-response of Notch to *cis*-Delta in mammalian cells [Sprinzak et al., 2010]). In this way, we can postulate a mathematical model for the sigma factors and identify an ultrasensitivity region using the work from [Buchler and Louis, 2008].

Hence, if binding between $S$ and $A$ is tight we could conceive a "basal" situation in which the system is completely off (for instance, having a slightly larger $A$ production over $S$ production would result in $A$ sequestering all $S$ molecules). Then, inputs to the system that inactivate the anti-sigma could reduce its level enough to trigger positive up-regulation of the operon. If the system was tuned in a ultrasensitive regime, the positive up-regulation of $S$ could overwhelm, at least temporarily, the negative feedback due to up-regulation of $A$, thus generating pulses.

In order to verify the previous hypothesis, let us consider a collection of alternative sigma factors $S_i$ (for $i = 1, ..., N$, where $N$ is the total number of sigma factors considered), each expressed from an operon that also includes the corresponding anti-sigma factor $A_i$. Transcription of the operon is activated by the holoenzyme $C_i$ composed by the RNA polymerase ($R$) and the sigma factor itself, constituting a positive feedback. This feedback loop is interfered with by the anti-sigma factor $A_i$, which binds competitively to $S_i$. The situation is summarized in Figure 3.8.

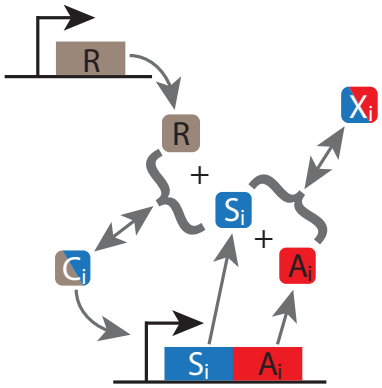


Figure 3.8: **Ultrasensitivity model diagram of interactions.** Alternative sigma factors ($S_i$) and their cognate anti-sigma factors ($A_i$) are expressed from the same operon. Transcription of the operon is activated by the holoenzyme $C_i$ composed by RNAP ($R$) and $S_i$, thus constituting a positive feedback. In turn, expression of $A_i$ sequesters $S_i$ forming the inactive complex $X_i$, thus interfering in the holoenzyme formation and leading to a negative feedback loop.

Modelling the dynamics of the biochemical processes described above by means of chemical kinetics we obtain:

$$\frac{dS_i'}{dt'} = \phi_s + \beta_s C_i' - k_{r+} R' S_i' + k_{r-} C_i' - k_{a+} A_i' S_i' + k_{a-} X_i' - \lambda_s S_i' \tag{3.1a}$$

$$\frac{dA_i'}{dt'} = \phi_a + \beta_a C_i' - k_{a+} A_i' S_i' + k_{a-} X_i' - \lambda_a A_i' \tag{3.1b}$$

$$\frac{dC_i'}{dt'} = k_{r+} R' S_i' - k_{r-} C_i' - \lambda_c C_i' \tag{3.1c}$$

$$\frac{dX_i'}{dt'} = k_{a+} A_i' S_i' - k_{a-} X_i' - \lambda_x X_i' \tag{3.1d}$$

$$\frac{dR'}{dt'} = \alpha - \sum_{i=1}^{N} k_{r+} R' S_i' + \sum_{i=1}^{N} k_{r-} C_i' - \lambda_r R' \tag{3.1e}$$

Assuming that the complexes' unbinding rates are sufficiently larger than the linear degradation rates, $k_{r-} \gg \lambda_c$, $k_{a-} \gg \lambda_x$, the corresponding equations can be adiabatically eliminated, leading to the following simplified model in dimensionless units:

$$\frac{dS_i}{dt} = \varphi_S + \rho_i R S_i - A_i S_i - \delta_S S_i \tag{3.2a}$$

$$\frac{dA_i}{dt} = \varphi_A + \xi\mu R S_i - A_i S_i - \delta_A A_i \tag{3.2b}$$

$$\frac{dR}{dt} = 1 - \sum_{i=1}^{N} \chi_i R S_i - R \tag{3.2c}$$

where the rescaled variables and parameters are shown in Table 3.2, and $\xi$ is an independent parameter that controls the intensity of the positive feedback loop.

Assuming now a tight binding in the sigma–anti-sigma interaction and considering only one sigma factor, we can generate pulses by externally decreasing $A$ production (this is, decreasing $\mu$) and then re-establishing the original value again, in order to recover $A$ levels that turn off $S$ free (see Figure 3.9).

In order to characterize the pulses we identified the ultrasensitivity regime, as in [Buchler and Louis, 2008]. As a result, we obtained the ultrasensitivity curves shown in Figure 3.10, where we plotted in panel A the sigma factor rescaled concentration at the equilibrium, $S_{eq}$, as a function of $\mu$, for different $S$ and $A$ degradation rates ($\delta_S$ and $\delta_A$, respectively); in panel B $S_{eq}$ as a function of $\varphi_S$, for several values of $\varphi_A$; and in panel C $S_{eq}$ as a function of $\varphi_A$, for several values of $\varphi_S$. Note that the simulation shown in Figure 3.9 corresponds to the blue line ($\delta_S = \delta_A = 0.005$) in Figure 3.10A, so that when we vary $\mu$ from 0.07 to 0.007 we move from the ultrasensitivity region to out of it. Then, when we reestablish $\mu$ to its original value we enter again in the ultrasensitivity region.

Further description of the ultrasensitivity regime for this model can be found in Appendix B.3.1.

**Rescaled variables**

$S_i = \frac{\lambda_x k_{a+}}{\lambda_r (k_{a-}+\lambda_x)} S_i'$ $\quad A_i = \frac{\lambda_x k_{a+}}{\lambda_r (k_{a-}+\lambda_x)} A_i'$

$R = \frac{\lambda_r}{\alpha} R'$ $\quad t = \lambda_r t'$

**Rescaled parameters**

$\varphi_S = \frac{\phi_s}{\lambda_r^2} \lambda_x \frac{k_{a+}}{k_{a-}+\lambda_x}$ $\quad \varphi_A = \frac{\phi_a}{\lambda_r^2} \lambda_x \frac{k_{a+}}{k_{a-}+\lambda_x}$

$\xi\mu = \frac{\alpha}{\lambda_r^2} \beta_a \frac{k_{r+}}{k_{r-}+\lambda_c}$ $\quad \chi = \frac{\lambda_c}{\lambda_x} \frac{k_{r+}}{k_{r-}+\lambda_c} \frac{k_{a-}+\lambda_x}{k_{a+}}$

$\delta_S = \frac{\lambda_s}{\lambda_r}$ $\quad \delta_A = \frac{\delta_A}{\delta_R}$

$\xi\gamma = \frac{\alpha}{\lambda_r^2} \beta_s \frac{k_{r+}}{k_{r-}+\lambda_c}$ $\quad \eta = \frac{\alpha}{\lambda_r^2} \lambda_c \frac{k_{r+}}{k_{r-}+\lambda_c}$

$\rho = \xi\gamma - \eta$

Table 3.2: **Rescaled variables and parameters for the dimensionless ultrasensitivity model.**

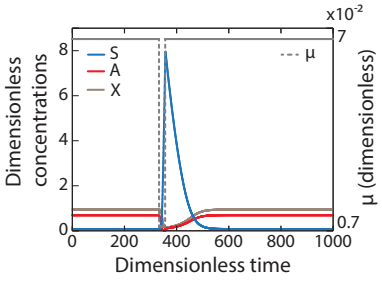


Figure 3.9: **Pulse resulting from ultrasensitivity.** Considering only one sigma factor, we can generate pulses by changing abruptly the value of $\mu$ from 0.07 to 0.007 and reestablishing the initial value again so that the pulse turns off. The parameter values used for this simulation are: $\phi_S = 0.003$, $\phi_A = 0.001$, $\xi = 11$, $\rho = 0.7$, $\chi = 0.8$, $\delta_S = 0.005$, $\delta_A = 0.005$, and $\mu = 0.07 - 0.007$.

Once we characterized the deterministic system, we implemented it under a stochastic framework in order to obtain a more realistic variation in $A$ production ($\mu$). Going back to the dimensional model, we performed stochastic simulations for 2 identical sigma factors ($i = 1, 2$) considering a noisy $\beta_{A,i}$ for each sigma (note that $\beta_A \propto \mu$, this is the anti-sigma production rate due to RNAP-sigma holoenzyme - see Table 3.2). Following [Shahrezaei et al., 2008], we generated one log-normal stochastic process for each $\beta_{A,i}$ so that $\beta_{A,i}(t) = \beta^0_{A,i} e^{\epsilon_i(t)} / \langle e^{\epsilon_i(t)} \rangle$. Where $\epsilon_i(t)$ is an Ornstein-Uhlenbeck (OU) process and the autocorrelation time of the $\beta_{A,i}$ noise is equal to the cell cycle duration (that is, 2 h approximately) as we can consider that $A_i$ a stable protein and is therefore only diluted by cell division. Exponentiating the OU process ensures that the noisy reaction rate is always positive. In fact, the new reaction rate becomes log-normally distributed, consistent with experimental observations that have found gene expression rates to be log-normally distributed rather than follow a normal distribution [Rosenfeld et al., 2005]. Normalizing the reaction rate by $\langle e^{\epsilon_i(t)} \rangle$ ensures that the mean value of $\beta_{A,i}$ is not affected by noise.

In Figure 3.11 the time series of $C_1(t)$ and $C_2(t)$ for one particular simulation are shown, as well as the evolution of free RNAP ($R(t)$) (see Appendix B.3.1 for more details and Table B.4 for the numerical values of the parameters).

This model relies in ultrasensitivity due to the tight binding between the sigma factor and its cognate anti-sigma, and assumes that extrinsic noise affects only the expression rate of the anti-sigma factor despite being $S$ and $A$ expressed from the same operon. It is particularly interesting the fact that we do need an asymmetry between $S$ and $A$ in order to obtain non-trivial pulses. This might suggest the existence of an "extra process" involved in obtaining a functional anti-sigma factor.

One interesting hypothesis related to the extrinsic noise affecting only

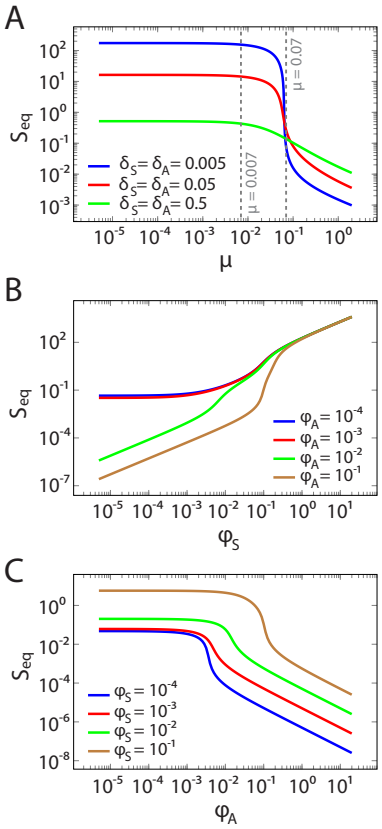


Figure 3.10: **Ultrasensitivity curves.** Ultrasensitivity increases for (A) lower degradation rates, $\delta_S$ and $\delta_A$; (B) higher basal production of anti-sigma, $\varphi_A$; (C) higher basal production of sigma, $\varphi_S$. Curves were obtained for the following sets of parameter values: $\rho = 0.7$, $\xi = 11$, $\chi = 0.8$ and (A) $\varphi_S = 0.003$, $\varphi_A = 0.001$; (B) and (C) $\delta_S = 0.005$, $\delta_A = 0.005$, and $\mu = 0.07$.
Panel (A) explicitly shows $\mu$ values used in Figure 3.9; the parameter set considered in that simulation corresponds to the blue curve.

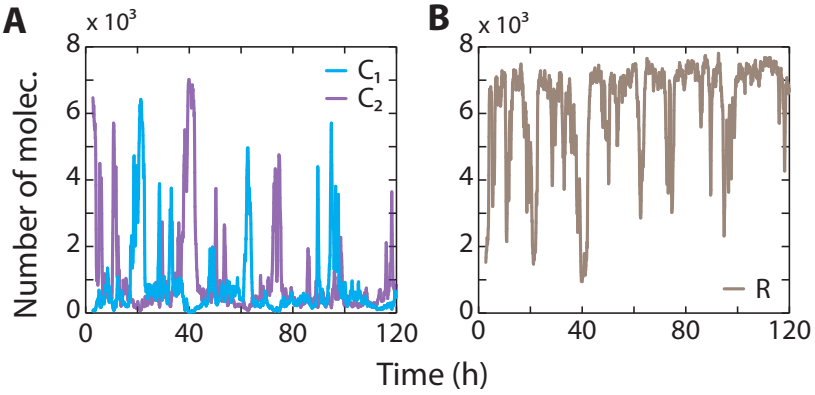


Figure 3.11: **Time traces for sigma-RNAP holoenzyme from a stochastic simulation of 2 identical coupled sigma factors with noisy $\beta_{A,1}$ and$\beta_{A,2}$.** (A) Number of molecules for sigma-RNAP holoenzyme, $C_1$ and $C_2$, and (B) number of free RNAP molecules, $R$, are plotted in function of time. See Table B.5 for parameter values considered for this simulation.

the anti-sigma factor is the following. In the group of the extracytoplasmic function (ECF) sigma factors (which includes $\sigma^M$, $\sigma^W$, $\sigma^X$, $\sigma^Y$ and $\sigma^Z$) one common feature is the way the anti-sigma factor inactivates its cognate sigma factor. In most cases, the anti-sigma is a transmembrane protein that sequesters by default its cognate sigma factor, only releasing it when receiving a certain input from the extracellular environment [Helmann, 2002, Zellmeier et al., 2005]. Thus, for the anti-sigma factor to be functional after being produced, it would need to be located in the membrane in order to be able to inactivate $S$. Besides, under this hypothesis the anti-sigma factor would be the element of the circuit receiving extracellular signals, and thus subject to external noise.

Regarding the remaining sigma factors considered in our experiments, in the case of $\sigma^B$ the asymmetry hypothesis between $S$ and $A$ still holds, as $\sigma^B$ anti-sigma factor RsbW is further regulated by the anti-anti-sigma factor RsbV that acts as an energy stress sensor [Locke et al., 2011]. In the case of $\sigma^D$ (responsible for flagellar biosynthesis) its cognate anti-sigma (FlgM) is present in the cytosol until the hook-basal body structure complex (HBB, this would be the base of the flagellum) is functional. Then FlgM is exported outside the cytoplasm presumably via this HBB structure allowing $\sigma^D$ to activate the transcriptional program for flagellum generation [Hughes and Mathee, 1998]. Finally, $\sigma^L$ up to date does not have an identified anti-sigma factor. Some authors postulate a roadblock regulation mechanism for $\sigma^L$ mediated by ccpA (a protein that mediates catabolite repression): ccpA would bind to a specific region of the $\sigma^L$ gene when glucose is present, thus preventing the RNAP proceed with transcription of this gene [Choi and Saier, 2005]. But ccpA is not part of $\sigma^L$ operon (as opposite to the general case where the sigma factor and its anti-sigma are transcribed from the same operon). So in the case of $\sigma^L$ the asymmetry hypothesis between $S$ and $A$ would still hold, but the production from $S$ and $A$ would not come from the same operon.

### 3.4.2 *Ligand model*

Following with the ECF sigma factors discussion at the end of Section 3.4.1 regarding the transmembrane anti-sigma factor detecting certain environmental inputs, we propose here another mathematical model that incorporates a ligand ($L_i$) responsible for the inactivation of its target anti-sigma ($A_i$) thus allowing the release of its cognate sigma factor ($S_i$). See Figure 3.12 for a diagram of circuit's interactions.

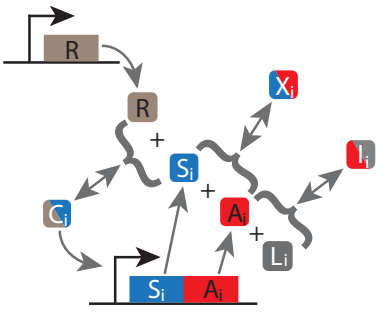


Figure 3.12: **Ligand model diagram of interactions.** Each alternative sigma factor pathway involves a sigma factor, $S_i$, an anti-sigma factor, $A_i$, and a regulatory ligand, $L_i$. All negative regulation occurs through sequestration. RNAP, $R$, is shared between the sigma factors, and the holoenzyme $C_i$ (composed by $R$ and $S_i$) activates the expression of the operon containing $S_i$ and $A_i$.

In this model, a stochastic burst of ligand production can suddenly reduce the activity of its cognate anti-sigma factor allowing the initiation of a pulse of the corresponding sigma factor. Autoregulation of the sigma factor operon reinforces the pulse by up-regulating expression of the sigma factor itself. The pulse eventually terminates itself through increased expression of the anti-sigma factor (see Figure B.8).

The corresponding reactions for this model are listed in Table 3.3. Note that $L_i(t)$ follows a gamma distribution as a result of the interactions specified in this table. This was motivated by previous observa-

tions that cellular protein concentrations follow a gamma distributed Ornstein-Uhlenbeck (GOU) process [Friedman et al., 2006, Raj et al., 2006, Taniguchi et al., 2010].

| **Basal productions** | | **Activated productions** | | **Ligand dynamics** | |
|---|---|---|---|---|---|
| $\varnothing \xrightarrow{k_2} S_i$ | (a) | $C_i \xrightarrow{\beta_S} C_i + S_i$ | (j) | $P_{OFF,i} \xrightarrow{K_1} P_{ON,i}$ | (r) |
| $\varnothing \xrightarrow{k_3} A_i$ | (b) | $C_i \xrightarrow{\beta_A} C_i + A_i$ | (k) | $P_{ON,i} \xrightarrow{K_2} P_{OFF,i}$ | (s) |
| $\varnothing \xrightarrow{k_1} R$ | (c) | **Degradations/dilutions** | | $P_{ON,i} \xrightarrow{K_3} P_{ON,i} + m_i$ | (t) |
| **Formation of complexes** | | $S_i \xrightarrow{k_{12}} \varnothing$ | (l) | $m_i \xrightarrow{K_4} m_i + L_i$ | (u) |
| $S_i + A_i \xrightarrow{k_{a+}/\Omega} X_i$ | (d) | $A_i \xrightarrow{k_{13}} \varnothing$ | (m) | $m_i \xrightarrow{K_5} \varnothing$ | (v) |
| $X_i \xrightarrow{k_{a-}} S_i + A_i$ | (e) | $R \xrightarrow{k_{11}} \varnothing$ | (n) | $L_i \xrightarrow{K_6} \varnothing$ | (w) |
| $A_i + L_i \xrightarrow{k_{l+}/\Omega} I_i$ | (f) | $X_i \xrightarrow{k_{14}} \varnothing$ | (o) | | |
| $I_i \xrightarrow{k_{l-}} A_i + L_i$ | (g) | $I_i \xrightarrow{k_{15}} \varnothing$ | (p) | | |
| $S_i + R \xrightarrow{k_{r+}/\Omega} C_i$ | (h) | $C_i \xrightarrow{k_{16}} \varnothing$ | (q) | | |
| $C_i \xrightarrow{k_{r-}} S_i + R$ | (i) | | | | |

Table 3.3: **Set of reactions for the stochastic ligand model.** Where $\Omega$ is a volume factor that in bacteria can be considered $\approx$ 1 molec nM$^{-1}$ [Süel et al., 2007] (see Table B.6).

Figure 3.13 shows the time series for $L$, $C$ and $R$ corresponding to a stochastic simulation of one sigma factor.

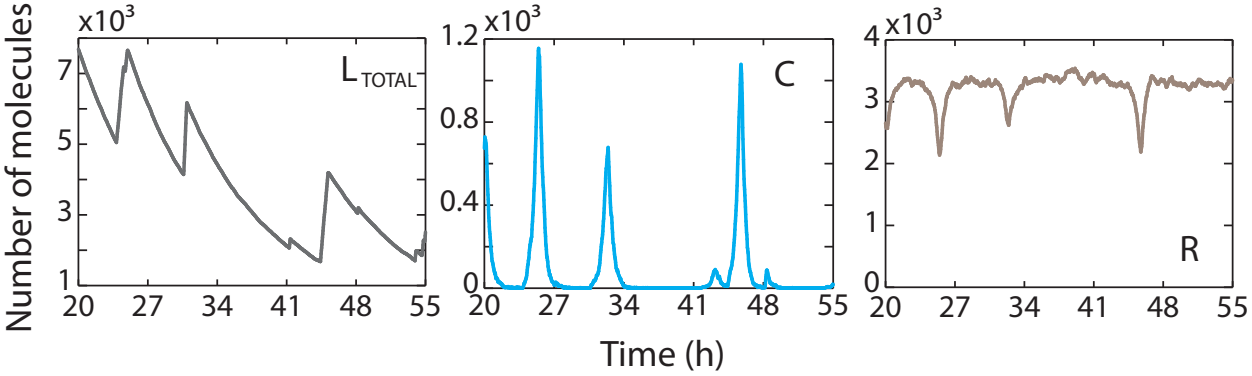


Figure 3.13: **Time series of the ligand model for one sigma.** Time traces for the total amount of ligand, $L_{TOTAL}$ (left panel); the sigma-RNAP holoenzyme complex, $C$ (center panel); and the available RNAP, $R$ (right panel), corresponding to a stochastic simulation of one sigma factor. Only one sigma factor is enough for pulsing. Parameter values for this simulation are shown in Table B.6.

We focused on the deterministic system in order to optimize computation time. The ligand concentration was generated in bursts randomly distributed over time uniformly, and exponentially distributed in magnitude. This ensures a GOU process for the ligand protein concentration. This implementation allows for direct manipulation of both burst magnitude and frequency independently. Hence, the ordinary differential equations (ODEs) were solved between the stochastic ligand bursts in the discretized stochastic GOU process.

The system ODEs are the following:

$$\frac{dS_i}{dt} = k_2 - k_{a+}S_iA_i + k_{a-}X_i - k_{r+}S_iR + k_{r-}C_i + \beta_S C_i - k_{12}S_i \tag{3.3a}$$

$$\frac{dA_i}{dt} = k_3 - k_{a+}S_iA_i + k_{a-}X_i - k_{l+}L_iA_i + k_{l-}I_i + \beta_A C_i - k_{13}A_i \tag{3.3b}$$

$$\frac{dR}{dt} = k_1 - \sum_{i=1}^{N} k_{r+}RS_i + \sum_{i=1}^{N} k_{r-}C_i - k_{11}R \tag{3.3c}$$

$$\frac{dI_i}{dt} = k_{l+}L_iA_i - k_{l-}I_i - k_{14}I_i \tag{3.3d}$$

$$\frac{dX_i}{dt} = k_{a+}S_iA_i - k_{a-}X_i - k_{15}X_i \tag{3.3e}$$

$$\frac{dC_i}{dt} = k_{r+}RS_i - k_{r-}C_i - k_{16}C_i \tag{3.3f}$$

Where $L_i(t)$ follows:

$$\frac{dL_i}{dt} = k_{l-}I_i - k_{l+}L_iA_i - k_{17}L_i \tag{3.4}$$

and its dynamics is modified by adding the random quantity $\epsilon_0 L_i(t)$ (being $\epsilon_0$ a random number exponentially distributed that controls the ligand burst magnitude) at random times $T_0$ (uniformly distributed) throughout the simulation. Hence,

$$L_i(t) \to L_i(t) + \epsilon_0 L_i(t) \tag{3.5}$$

The deterministic version of the ligand model is the system we used to simulate competition and correlation (see Section 3.5).

### 3.4.3 *Limit cycle model*

A different possibility for modelling sigma factor pulses of activity is to think about every pulsing sigma as an independent oscillator, coupled between each other through RNAP sharing.

Taking into account the interactions shown in Figure 3.14, the model ODEs are the following:

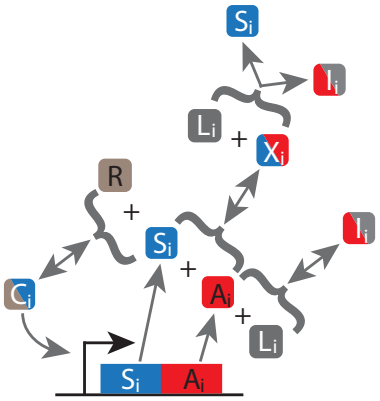


Figure 3.14: **Limit cycle model diagram of interactions.** Interactions in this model are the ones described in Figure 3.12 except that in here the ligand ($L_i$) can break the inactive sigma–anti-sigma complex ($X_i$), forming a ligand–anti-sigma aggregate ($I_i$) thus releasing the sigma factor ($S_i$).

$$\frac{dS_i}{dt} = k_2 - k_{a+}S_iA_i + k_{a-}X_i - k_{r+}S_iR + k_{r-}C_i + k_{lx}L_iX_i + \beta_S M_i - \delta S_i \tag{3.6a}$$

$$\frac{dA_i}{dt} = k_3 - k_{a+}S_iA_i + k_{a-}X_i - k_{l+}L_iA_i + \beta_A M_i - \delta A_i \tag{3.6b}$$

$$\frac{dX_i}{dt} = k_{a+}S_iA_i - k_{a-}X_i - k_{lx}L_iX_i - \delta X_i \tag{3.6c}$$

$$\frac{dI_i}{dt} = k_{l+}L_iA_i + k_{lx}L_iX_i - \delta I_i \tag{3.6d}$$

$$\frac{dC_i}{dt} = k_{r+}RS_i - k_{r-}C_i - \delta C_i \tag{3.6e}$$

$$\frac{dM_i}{dt} = k_m Tr_i - (\delta + \delta_m)M_i \tag{3.6f}$$

$$\frac{dTr_i}{dt} = k_t C_i - k_m Tr_i - (\delta + \delta_m)Tr_i \tag{3.6g}$$

Where $L_i(t) = L_T^{(i)} - I_i(t)$ is the amount of free ligand (with $L_T^{(i)}$ being the total pool of ligand fixed at the beginning of the simulation), $R = R_T - \sum_{i=1}^{N} C_i$ is the amount of available RNAP (with $R_T$ being the total pool of RNAP, also a constant parameter of the simulation), $M_i$ is the mRNA that will be translated into its corresponding sigma factor ($S_i$) and its anti-sigma ($A_i$), and $Tr_i$ represents the immature form of $M_i$. These ODEs are essentially the same presented in Section 3.4.2 (Eq.(3.6)) except that in here the total amount of ligand ($L_T^{(i)}$) and RNAP ($R_T$) present in the system are constant throughout the simulation. Also, we introduced another interaction for which the ligand ($L_i$) can break the sigma–anti-sigma inactive complex ($X_i$), forming a ligand–anti-sigma aggregate ($I_i$) thus releasing the sigma factor ($S_i$) that can now bind to RNAP. This "partner-switching" interaction together with the implicit delay introduced through explicitly modeling mRNA (via $M_i$ and $Tr_i$ species) facilitate that the model could present a stable limit cycle.

We first identified a volume in parameter space that was biologically meaningful, and systematically explored a multi-dimensional region of this volume looking for oscillations that are robust with respect to variations of the total RNAP pool ($R_T$) and pulse durations of the order of magnitude of the experimental data (this is, around 1 h). It is worth to mention that this system was too stiff to perform a numerical bifurcation analysis with the numerical continuation software AUTO through XPP [Ermentrout and Mahajan, 2003].

Time traces for the complex sigma-RNAP ($C$) and free RNAP ($R$) simulating only one sigma factor are plotted in Figure 3.15. Note that for the parameter values considered here the RNAP is not saturated, as it is not straightforward to find biologically meaningful parameters for which oscillations are robust to reasonable variations of $R_T$, pulse durations are around 1 h and free RNAP is low.

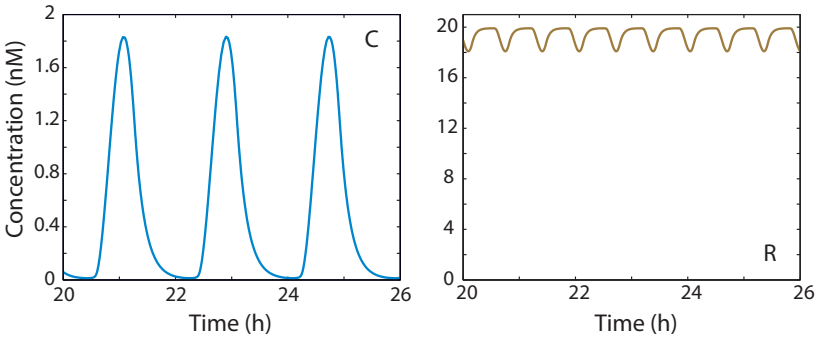


Figure 3.15: **Limit cycle model time series for only one sigma.** Time traces for the holoenzyme complex sigma-RNAP, $C$, (left panel) and the available RNAP, $R$, (right panel) corresponding to numerical integration of the ODEs. Only one sigma factor is enough for pulsing. Note that under the current parameter set RNAP is not saturated. Parameter values for this simulation are shown in Table B.8.

## 3.5 *Modelling competition and correlation*

To model competition and correlation between pulses of sigma factor activity, we chose the ligand model in front of the ultrasensitivity and the limit cycle ones because these two models present some difficulties. Regarding the ultrasensitivity model, it is not straightforward to modify pulse frequencies and durations in order to match experimental data. Regarding the limit cycle model, the parameter set found results in pulse durations and amplitudes in agreement with experimental data but it does not operate in the regime of RNAP saturation.

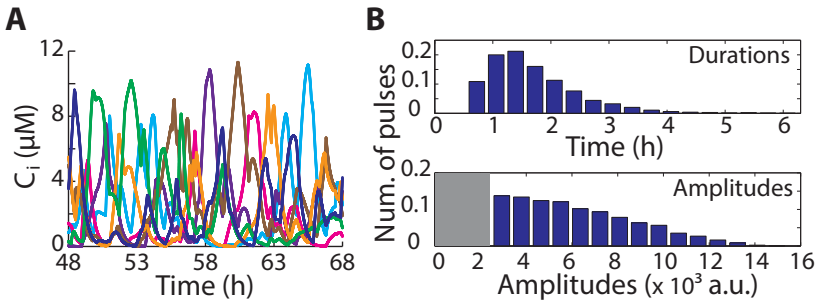


Figure 3.16: **Ligand model simulations for 7 identical pulsing sigma factors.** (A) Time traces for the RNAP-sigma factor holoenzyme ($C_i$) of 7 identical pulsing sigma factors ($i = 1, \ldots, 7$). (B) Histogram of pulse durations (upper panel) and amplitudes (lower panel) for the simulation shown in panel (A). Gray area in the amplitudes histogram indicates the selected cutoff (set to amplitude = 2500 a.u.), when a pulse surpasses this cutoff it is counted as a pulse and is discarded otherwise. Parameter values for this simulation are shown in Table B.7.

In order to understand how sigma factor pulses interact in a scenario of limiting amounts of RNAP, we proceeded to couple 7 identical sigma factors for the ligand model (see Section 3.4.2). We first identified physiologically reasonable parameters that could produce similar pulsing dynamics to those observed experimentally, under conditions of limiting amounts of RNAP (see Figure 3.16). In these simulations, sigma-RNAP pulses present a typical duration of around 1 h and a long-tailed distribution for amplitudes, in agreement with experimental data[2]. While a pulse is active, the amount of available RNAP is significantly reduced, hence alternative sigma factors compete for the use of RNAP. The pulse eventually terminates itself through increased expression of the anti-sigma factor, thus releasing RNAP and allowing other sigma factors to initiate pulses (Figure B.8).

[2] Experimental and simulated pulses were defined and analyzed in the same way. See Appendix B.2 for details.

Note that if we remove the anti-sigma factor from the model the resulting sigma does not pulse (Figure 3.17), being now constitutively expressed. As we saw in Section 3.2 this is the case for the housekeeping sigma factor $\sigma^A$ (see Figure 3.5). This sigma factor was not explicitly included in the simulations, because its effect can be directly translated into reducing the pool of RNAP present in the system.

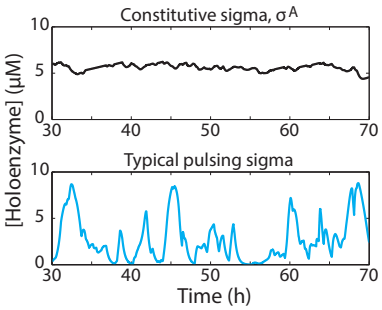


Figure 3.17: **A sigma factor with no anti-sigma associated does not pulse.** This figure shows time series for a sigma factor with no anti-sigma associated, situation corresponding to $\sigma^A$, (upper panel) and for a standard sigma factor (lower panel). As can be clearly seen, removing the cognate anti-sigma results in a total loss of the pulsing behavior, now being this sigma factor constitutively expressed. Parameters used for these simulations are the same as in Figure 3.16.

Figure 3.18 quantifies time-share dynamics. Panel A shows that at any given time > 75% of available RNAP was occupied by just 2-3 most active alternative sigma factors. This is in agreement with the experimental distribution of the number of sigma factors active at a time shown in panel B (this calculation was performed from the experimental data assuming that pulses are uncorrelated between the different sigma factors, and considering the frequencies and durations measured experimentally for each of the 7 studied sigma factors, see Appendix B.4 for details). These results suggest that only a few sigma factors occupy RNAP simultaneously, and that active sigma factors alternate the possession of RNAP over timescales of the pulse duration. In our simulations, the different sigma factors compete for RNAP as shown in Figure 3.18C, although the level of competition is not as high as what we saw experimentally (see Figure 3.7). One prediction of this model is that one active sigma factor is strongly anti-correlated with the remaining sigmas (see Figure 3.18D). Unfortunately, checking this prediction experimentally presents numerous technical challenges, being the main one the limitation in the number of available colors in fluorescence microscopy that prevents simultaneously tracking several sigma factors in the same movie. Another one is obtaining long time-series data to compute sufficiently clear experimental cross-correlations.

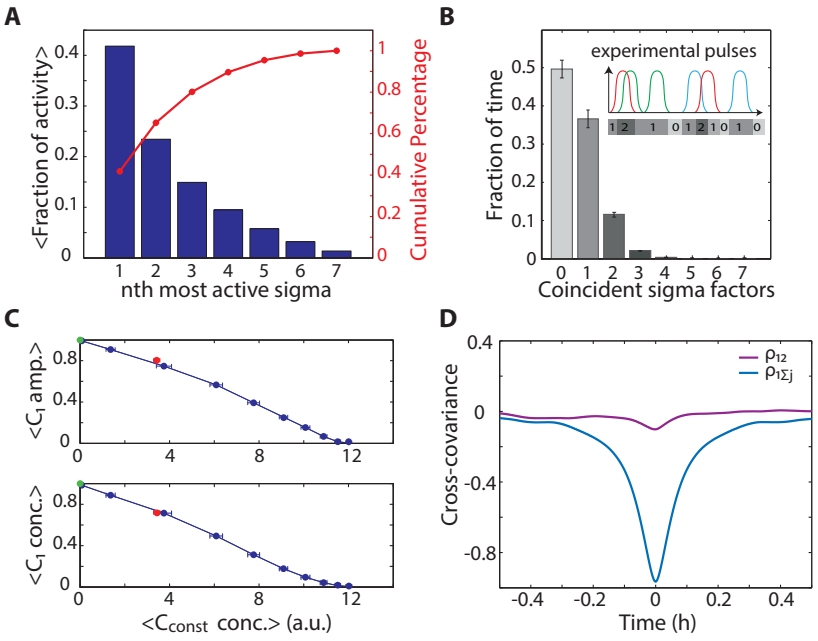


Figure 3.18: **Activity distribution, competition and cross-correlation for the ligand model.** (A) Activity distribution of the n-th most active sigmas (blue bars) computed for the simulation shown in Figure 3.16. The cumulative percentage of sigma activity accounted for by the most active sigmas (in red) is also plotted. The 79% of the RNAP is being used by 3 sigma factors. (B) Predicted distribution of the number of sigma factors simultaneously active from experimentally determined pulse statistics, assuming pulse independence (from J.C.W.Locke and J.Park [Locke et al., 2014]). See Appendix B.4 for details on the calculation. (C) Competition plot for 6 pulsing sigmas and 1 constitutively expressed sigma factor. Here we have considered 3 different stabilities for the $C_i$ complex, with the strongest sigma (the one with highest affinity for the RNAP) being the one that is expressed constitutively in an inducible manner, and the weakest sigma (the one with the lowest affinity for the RNAP) being the one we used to evaluate the effects of that induction. The green dot corresponds to the situation of $N = 6$ pulsing sigmas, and the red dot corresponds to the "wild-type" situation, with $N = 7$ pulsing sigmas. Parameters used for these simulations are shown in Table B.7. (D) Cross-correlation between $\sigma^1$ and $\sigma^2$ (two identical pulsing sigmas) for simulation shown in Figure 3.16A (purple line); and between $\sigma^1$ and the sum of all the remaining sigmas (blue line). This latter case suggests that one sigma factor is strongly anti-correlated with all the other sigma factors.

In summary, this model shows that time-sharing can emerge from the combination of pulsatile activation dynamics and competition for core RNAP.

## 3.6 *Discussion*

In order to understand the phenotypic consequences of time-sharing in cells, let us compare two scenarios. One way of sharing core RNA polymerase would be partitioning RNAP molecules between the different sigma factors at constant levels over time (this is, concentration sharing, as in Figure 3.1C upper panel). In this case, cells would exhibit relatively homogeneous phenotypes among them. This the starting mechanism that has been considered so far in the literature.

In contrast, alternative sigma factors can use RNAP almost exclusively during short periods of high activity (time-sharing, as in Figure 3.1C lower panel). This new sharing mechanism is the one we propose in our sigma factor pulses. The pulses' duration is of the order of about 1 h, which means that during a cell's life (the cell division time in our experiments is 1.9 ± 0.2 h) only one or very few alternative sigma factors are active. At a population level, as pulses of activity are generated stochastically, the picture is that there are always subpopulations of cells in every phenotype. This ensures a prompt response of at least one of these subpopulations to rapidly evolving environmental stresses, without cells having to cycle through the activation of all the different sigma factors.

Following this train of thought, we could imagine a specific transient stress selecting a given subpopulation, then once the stress signal is over,

the full distribution of phenotypes would be re-established after about one cell cycle.

In summary, time-sharing and concentration sharing can result in very different phenotypic distributions that have a large impact in how cell populations face rapidly changing environments.

Other functional capabilities that time-sharing may offer to cells are avoiding conflicts between incompatible gene regulatory programs, and increasing coordination of target promoters by concentrating most target gene expression into brief periods of high activation.

Time-sharing is a common solution to allocate limited resources between multiple users in other contexts. As mentioned at the beginning of this Chapter one example is the time-division multiplexing protocol that allows the simultaneous transmission and reception of multiple independent signals using a single channel [Chu, 1969, Decina and Rossi, 1980]. Another example would be distributed computing systems where the processor is shared between different jobs that alternate its use depending on activity [Wilkes, 1972]. In biology, many cellular systems rely on shared molecular components, hence time-sharing could represent a general dynamic design principle used by other molecular systems in the cell.

# *III*

# *Oscillatory dynamics in genetic circuits in bacteria*

# 4
# *Coupling oscillators*

In previous Chapters we dealt with coupled dynamical processes that resulted in pulsatile protein expression or activity. Here we will focus on dynamical processes occurring in the form of periodic oscillations in the expression of proteins. As explained in Chapter 1 genetic oscillators are a widespread dynamical phenomenon in living organisms. In particular, circadian rhythms (characterized by a period of about 24 h) have attracted a great interest in the last two decades in part due to its challenging dynamics and in part due to their role in controlling some key processes in organisms (such as repair mechanisms [Lahav, 2004], and metabolic [Kaasik and Lee, 2004] and signalling pathways [Covert et al., 2005]). A very interesting study at the single cell level about how the circadian clock entrains cell cycle in cyanobacteria is the one by [Yang et al., 2010]. Understanding how genetic oscillators interact with each other and produce a certain phenotype is an important question that needs to be addressed. In this Chapter we study the interaction between a natural oscillator, such as cell cycle in *Escherichia coli*, and a synthetic one.

## *4.1 Genetic oscillators*

The bacterial cell cycle consists in cell growth, chromosomal replication and cell division [Wang and Levin, 2009]. In general, for all bacterial species and during the exponential phase, this whole cycle has a fairly constant period under a fixed set of conditions (such as temperature and culture medium), thus being a natural genetic oscillator.

During bacterial duplication, it is critical to ensure that daughter cells will inherit one copy of the chromosome, and only one. Hence, chromosomal replication must occur only once per cell division. Replication is initiated at a specific site of the DNA, known as *oriC*, where the replication machinery conformed by several proteins is recruited forming multimeric complexes. The formation of these complexes is triggered by specific proteins, such as DnaA in *E. coli* [Donachie and Blakely, 2003, Katayama et al., 2010]. Only the active form of DnaA initiates replication. Once the process has started, cell needs to inhibit DnaA activity to ensure that replication occurs only once per cell division. *E. coli* presents three main DnaA-regulatory mechanisms, one of them consisting in

the so-called the regulatory inactivation of DnaA (RIDA) system.The RIDA system is essentially formed by the Hda protein and the beta subunit of DNA polymerase III holoenzyme, encoded by *dnaN* gene. This RIDA complex forms a sliding clamp on DNA that converts the active ATP-DnaA to the inactive ADP-DnaA form, thus preventing replication re-initiation [Camara et al., 2005, Kaguni, 2006, Katayama et al., 2010].

One of the consequences of chromosomal replication is that during a certain fraction of the cell cycle bacteria have two copies of the genome. In this way cell cycle drives the number of proteins of transcribed genes [Swain et al., 2002]. This is something to take into account when studying genetic oscillators operating inside a cell.

Over the last two decades synthetic biology has provided grounds for understanding complex gene regulatory networks by the engineering of simple circuits that can be used as toy models. As already mentioned in Chapter 1 and at the beginning of this Chapter, genetic oscillators exhibiting different periods have been found in a large variety of organisms (for a nice review on biological oscillators and modelling see [Goldbeter, 2002]). Several efforts have been made in this field to understand the basic principles governing gene regulatory networks that lead to oscillatory dynamics. This is the case of the synthetic oscillator for *E. coli* developed in the laboratory of Prof. J. Hasty at the University of California San Diego [Stricker et al., 2008]. This synthetic oscillator was engineered using an inducible combinatorial promoter ($P_{lac/ara}$) for which the following gene transcription is activated by the AraC protein in the presence of arabinose, and repressed by the LacI protein in the absence of isopropyl $\beta$-D-1-thiogalactopyranoside (IPTG) (see Figure 4.1). The two components of the oscillator: *araC* and *lacI* genes, and the green fluorescent protein (*gfp*) gene that acts as a reporter, were marked with a degradation tag and were placed under the control of three identical copies of the $P_{lac/ara}$ promoter. Then, these elements were introduced into two different plasmids and transformed in a genetically modified *E. coli* with deletions in the *araC* and *lacI* wild-type genes, conforming the JS011 strain (see Supplementary Information in [Stricker et al., 2008]). Thus, activating the promoters in the presence of arabinose and IPTG results in the transcription of the three elements. Incrementing AraC levels results in a higher transcription of the three elements (positive feedbak), but once a critical level of LacI is reached the transcription is slowed down (negative feedback). The combined dynamics of these two feedback loops can lead to oscillations in protein expression levels.

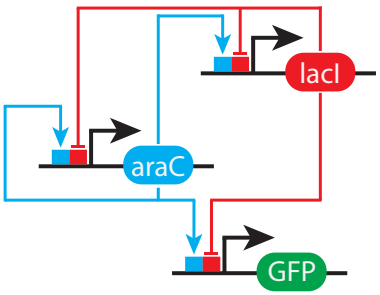


Figure 4.1: **Network diagram of the synthetic oscillator.** The hybrid promoter $P_{lac/ara}$ controls the transcription of *araC* and *lacI* genes, forming a positive and a negative feedback loop respectively. *gfp* acts as a reporter of the state of the genetic oscillator.

Many cellular processes are driven by oscillating gene regulatory networks, and it is still not well understood how these genetic oscillators coordinate with each other inside a living cell. One approach to this question might be provided by the concept of phase synchronization introduced by Rosenblum *et al.*, who applied it to the study of weakly coupled self-sustained chaotic oscillators [Rosenblum et al., 1996]. In this Chapter we will establish the degree of entrainment caused in the synthetic oscillator developed by Hasty and co-workers (JS011) by the

bacterial cell cycle, and we will determine whether the two oscillators can mutually entrain their dynamics by ectopically implementing a back-coupling from the synthetic oscillator to the chromosomal replication. For this purpose, we designed and constructed a plasmid (pMiL101) that contains a copy of *hda* and *dnaN* genes (members of the RIDA system) under the control of the oscillator $P_{lac/ara}$ promoter, and we introduced it into he synthetic oscillator strain JS011, conforming a bidirectionally coupled strain (see Appendix C.1 for details). Figure 4.2 shows a diagram of the synthetic oscillator back-coupled to chromosomal replication.

To ensure a fair comparison between the synthetic oscillator driven by cell cycle system and the back-coupled one, we transformed the pMiL101 plasmid backbone (this is, the plasmid containing only the origin of replication and the antibiotic resistance, without the back-coupling to replication) into JS011 (see Appendix C.1 for details). We will refer to this strain as the unidirectional strain.

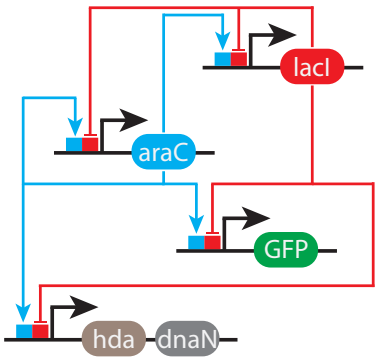


Figure 4.2: **Network diagram of the synthetic oscillator back-coupled to chromosomal replication.** This is the network shown in Figure 4.1 with an extra element: another copy of the hybrid promoter $P_{lac/ara}$ driving the transcription of *hda* and *dnaN* genes, members of the RIDA system that inhibit the initiation of chromosomal replication.

## 4.2 *Characterization of the natural and synthetic genetic oscillators*

We started by characterizing the synthetic oscillator driven by the cell cycle using the unidirectional strain. We filmed microcolonies of this strain with time-lapse fluorescence microscopy, and tracked individual cells while growing in a minimal medium containing 0.7 % (w/v) Arabinose and 2 mM IPTG (see Appendix C.2 for details on cell culture and imaging). Figure 4.3A shows a filmstrip of the unidirectional strain, with the GFP signal colored in green. A heterogenous pattern "off-on-off-on" in GFP fluorescence can be appreciated in single cells, reflecting the oscillations in the reporter's expression. Time traces for cell length and fluorescence of three independent lineages for this strain are plotted in Figure 4.3B.

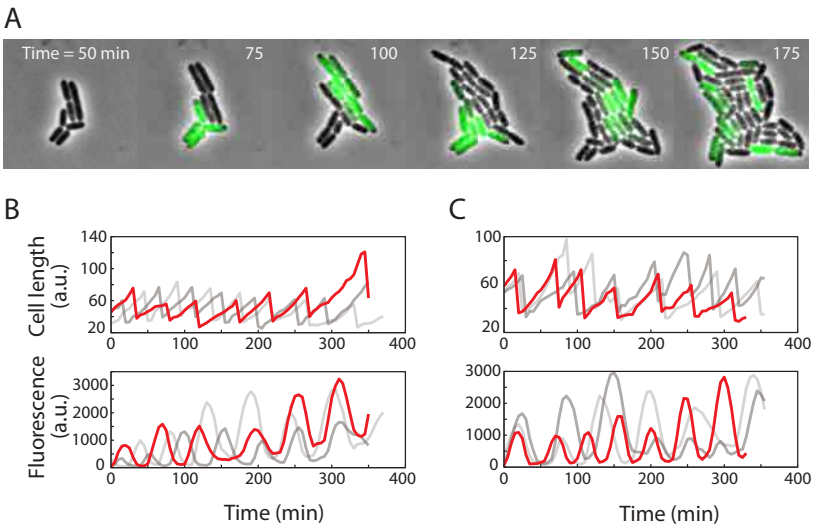


Figure 4.3: **Tracking the natural and synthetic oscillators.** (A) Filmstrip for the unidirectional strain (see Appendix C.2 for details on cell culture and imaging). GFP fluorescence (colored in green) follows a heterogeneous "off-on-off-on" oscillating pattern in single cells. (B) and (C) show cell length and GFP fluorescence time traces in independent lineages for the unidirectional case and the bidirectional one, respectively.

Analysis of data shows that the cell cycle period is ~ 48 ± 12 min and the synthetic oscillator period is ~ 54 ± 11 min under our experimen-

tal conditions. The distributions of these two quantities are shown in Figure 4.4A.

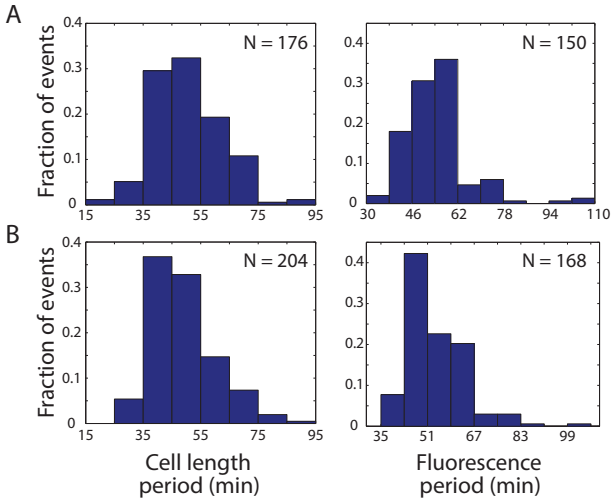


Figure 4.4: **Experimental distributions of the periods of the cell cycle (left) and synthetic (right) oscillators.** (A) Unidirectional strain, for these data period mean value plus/minus standard deviation of the mean were obtained for cell length, $\langle T_L \rangle = 48 \pm 12$ min, and fluorescence, $\langle T_F \rangle = 54 \pm 11$ min. (B) Bidirectional strain: $\langle T_L \rangle = 47 \pm 12$ min and $\langle T_F \rangle = 54 \pm 10$ min.

Figure 4.3C shows the time traces of the synthetic oscillator back-coupled to chromosomal replication using the bidirectional strain. In this case, when AraC and LacI in the synthetic oscillator are expressed at a high level, the RIDA system is also overexpressed, thus inhibiting replication initiation. In this case the obtained periods are $\sim 47 \pm 12$ min for the cell cycle and $\sim 54 \pm 10$ min for the synthetic oscillator under the same experimental conditions as the previous case. The corresponding distributions of the two quantities are shown in Figure 4.4B. Hence, introducing the back-coupling in the system seems not to affect the period of any of the two oscillators. However, given that overexpression of the RIDA system is controlled by the synthetic oscillator, we directly act on replication time. In this way, as we introduced in Section 4.1, the system can present phase synchronization when frequencies are adjusted in a way that we can establish a phase shift between the two oscillators [Pikovsky et al., 2003].

Therefore, we proceeded to define a phase that accounts for the progress of the system through a cycle, and correspondingly assigned it to each point of the time series data of the two oscillators. We defined a cycle as the segment of data going from one minimum of cell length to the following maximum (thus spanning the entire cell life), and fixed this phase to be 0 at the beginning of the cycle (when the cell is born) and 1 at the end of the cycle (just before the cell divides). As experimental data is sampled at a fixed interval, it is straightforward to assign the intermediate values for the phase. Fluorescence data was also segmented according to cell length cycles, and phases were assigned correspondingly.

We are now prepared to quantify the existing phase shift between the two oscillators by asking when fluorescence maximums occur within a cell length cycle. The distributions of the timing of fluorescence maximums within a cell length cycle are shown in Figure 4.5 for the unidirectional strain (left panel) and for the bidirectional one (right panel).

For the sake of clarity, phase has been redefined so that 0.6 indicates the minimum of cell length (when the cell is born) whereas 0.5 indicates the moment when cell achieves its maximum length. In this way, it is clear to appreciate that only the histogram for the bidirectional case appears as a unimodal distribution similar to a gaussian "bell curve". These results suggest that synchronization between the two oscillators increases with back-coupling.

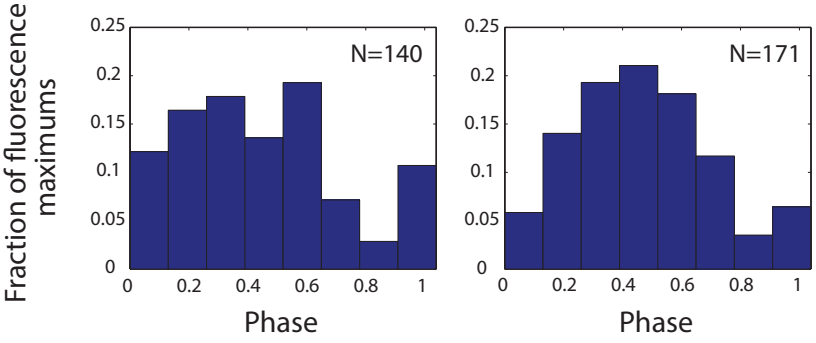


Figure 4.5: **Phase shift between the two oscillators.** Distributions of the timing of fluorescence maximums within a cell length cycle are plotted for the unidirectional case (left panel) and the bidirectional one (right panel). Note that only the histogram for the bidirectional case appears as a unimodal distribution similar to a gaussian "bell curve". The $x$ axis covers one full cycle of cell division. For a better visualization of data, phase has been redefined so that a phase equal to 0.6 denotes when the cell is born (minimum of cell length), whereas a phase equal to 0.5 indicates the moment of cell's maximum length.

## 4.3 *Modelling the two oscillators*

In order to deeper understand the experimental results we propose the following toy model. Since the unidirectional system (this is, the synthetic oscillator driven by cell cycle) is a particular case of the more general scenario depicted by the bidirectional system (where the synthetic oscillator is back-coupled to chromosomal replication), we will introduce first the bidirectionally coupled model and will explain the specificities of the unidirectional system as a particular case of the back-coupled model.

For the synthetic oscillator, we developed a reduced model based in an activator-repressor system [Rué and Garcia-Ojalvo, 2011] where only two species are described: the activator, $A$, and the repressor, $R$, both controlled by the same promoter. The dynamics of these two species is described by Eq.(4.1)a-b (see Appendix C.3 for details). Besides, the influence of the synthetic oscillator on replication is modeled by considering the production of the RIDA system ($B$), which is also controlled by the hybrid promoter, $P_{lac/ara}$, as given by Eq.(4.1)c.

In turn, the cell cycle was modelled as an integrate and fire mechanism, in which cell length grows exponentially (Eq.(4.1)d) and two thresholds trigger chromosomal replication and cell division events. In this way, when cell length reaches the first threshold (replication, $R_{thr}$) the productions of all the oscillator elements are doubled (as the copy number of genes is increased by 2-fold) (Eq.(4.2)). We are assuming here that all the considered species are transcribed at the same time. Given that all these genes are located in plasmids, the possible delays due to replicating genes from far away positions in the chromosome does not apply. $B$ is assumed to increase the threshold $R_{thr}$, in a way that mimics its inhibitory effect on replication (Eq.(4.3)). Once the cell length arrives

to the second threshold (division, $D_{thr}$), returns to its initial value $L_0$ (Eq.(4.4)) and the production rates are re-established to their original values (Eq.(4.2)). The full model is:

$$\frac{dA}{dt} = \alpha_1\zeta + \frac{\beta_1\zeta A^n}{K^n + A^n + (\gamma R)^p} - \delta_1 A \tag{4.1a}$$

$$\frac{dR}{dt} = \alpha_2\zeta + \frac{\beta_2\zeta A^n}{K^n + A^n + (\gamma R)^p} - \delta_2 R \tag{4.1b}$$

$$\frac{dB}{dt} = \alpha_3\zeta + \frac{\beta_3\zeta A^n}{K^n + A^n + (\gamma R)^p} - \delta_3 B \tag{4.1c}$$

$$\frac{dL}{dt} = \alpha_0 L \tag{4.1d}$$

where $\alpha_0 = L_0/\tau$ (with $\tau$ being the characteristic time of cell cycle). $\zeta$ is the parameter that reflects the driving of the synthetic oscillator by chromosomal replication:

$$\zeta = \begin{cases} 1 & \text{for } L_0 \leq L < R_{thr} \\ 2 & \text{for } R_{thr} \leq L < D_{thr}\ , \end{cases} \tag{4.2}$$

as mentioned above $B$ mediates the coupling of the synthetic oscillator to chromosomal replication by

$$R_{thr} = D_{thr} \cdot \left(\epsilon + \frac{\eta \cdot \kappa \cdot B}{B + K_l}\right). \tag{4.3}$$

Where $\epsilon \in (0, 1)$ is the fraction of the division threshold at which replication occurs. In the case when the synthetic oscillator is not back-coupled to replication, for $\epsilon \to 1$ we have that $R_{thr} \to D_{thr}$. When back-coupling is introduced ($0 < \eta \leq 1$) $R_{thr}$ increases and approaches $D_{thr}$. As the term $B/(B + K_l)$ saturates to 1, the maximum limit where replication can happen (considering the strongest back-coupling, so $\eta = 1$) is $\kappa = 0.9 \cdot (1 - \epsilon)$. We chose this limit because we estimated it was not biologically realistic that replication occurred simultaneously to cell division.

Besides, division events are implemented as follows

$$L(t) \text{ becomes } L_0 \quad \text{for } L = D_{thr}\ . \tag{4.4}$$

Note that as the synthetic oscillator elements are controlled by the same promoter ($P_{lac/ara}$) parameters $K$, $n$, $p$ and $\gamma$ are the same for species $A$, $R$ and $B$. Figure 4.6 shows two diagrams for the model interactions for the unidirectional and the bidirectional cases.

Some variability was introduced into the deterministic model by allowing random variation in the reaction rates. In this way, for each cell cycle parameter values were drawn from a gaussian distribution with mean values shown in Table C.1 and standard deviations ranging from 2% of the mean value in the case of the synthetic oscillator parameters (Eq.(4.1)a-c) up to 18% in the case of initial cell length $L_0$. This was adjusted to be in agreement with experimental results, in which the length

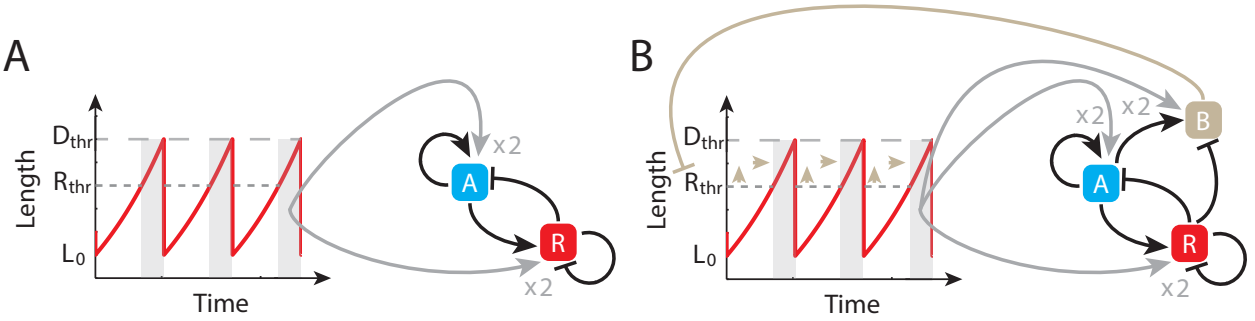


Figure 4.6: **Diagrams of model interactions.** Cell length increases exponentially between division events. When it reaches the replication threshold ($R_{thr}$) all the productions from the synthetic oscillator are doubled (gray areas). Once cell length arrives to the division threshold ($D_{thr}$) it returns to its initial value ($L_0$) and the synthetic oscillator productions are re-established to their original rates. This applies to (A) the unidirectional case and (B) the bidirectional one. Besides in (B), the oscillator inhibits replication initiation by increasing $R_{thr}$ so that it narrows the time intervals where oscillator production rates are doubled (pushes gray areas towards the right).

distribution of newborn cells shows a deviation of 18% for the unidirectional and the bidirectional strains, while the division ratio presents a deviation of 13% (see Figure 4.7). Also, in the light of maximum cell length distributions shown in this Figure, we assumed that back-coupling only affected the replication threshold (by incrementing its value and approaching it to the division threshold) and we left the division threshold unchanged.

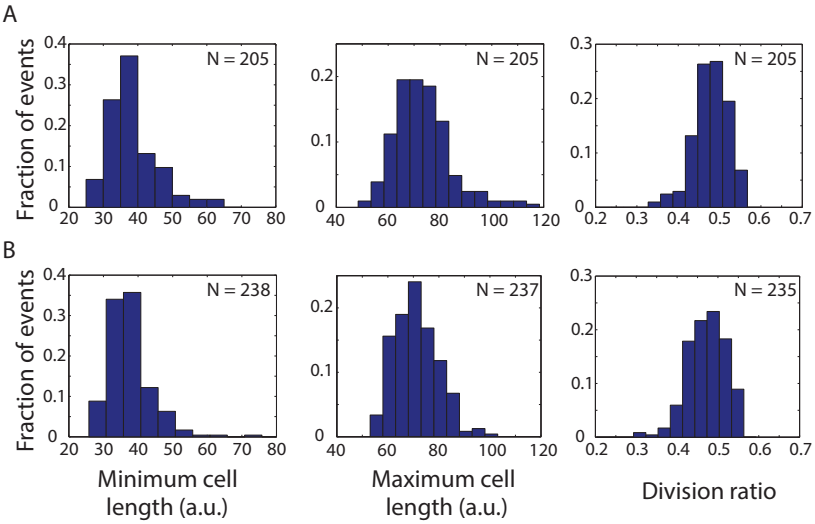


Figure 4.7: **Experimental distributions for cell length minimum, maximum and division ratio.** (A) Unidirectional strain new born cell length distribution (left panel), $\langle L_{min} \rangle = 39 \pm 7$ a.u, maximum cell length distribution (medium panel), $\langle L_{max} \rangle = 74 \pm 11$ a.u., and cell division ratio (defined as $\rho = (L_{max} - L_{min})/L_{max}$, right panel) distribution, $\langle \rho \rangle = 0.47 \pm 0.06$. (B) The same distributions are plotted for the bidirectional strain: $\langle L_{min} \rangle = 38 \pm 7$ a.u, $\langle L_{max} \rangle = 72 \pm 9$ a.u., and $\langle \rho \rangle = 0.47 \pm 0.06$.

Figure 4.8 shows the time series for the synthetic oscillator driven by cell cycle ($\eta = 0$) and for the synthetic oscillator back-coupled to chromosomal replication ($\eta > 0$), corresponding to the experiments with the unidirectional and the bidirectional strains, respectively. To allow comparison, experimental time traces for these strains in one independent lineage are also plotted. We focused in the activator ($A$) expression to account for the synthetic oscillator state as the model does not consider a fluorescent reporter. The replication threshold ($R_{thr}$) has been indicated in every cell cycle as a vertical gray bar. For $\eta = 0$ the periods obtained for the division and synthetic oscillators are $\langle T_L \rangle = 44 \pm 10$ min and

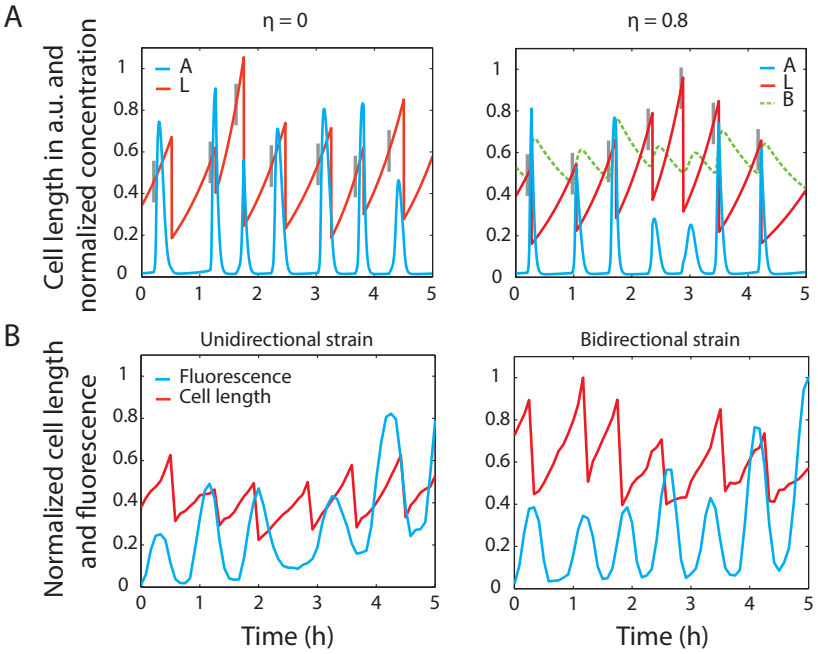


Figure 4.8: **Simulated and experimental time series of the coupled oscillators for the unidirectional case (left) and the bidirectional one (right).** (A) Numerical integration of the coupled oscillator model ODEs. Cell length ($L$) is shown in red and the normalized concentration of the activator ($A$) in blue. In every cell cycle, replication threshold ($R_{thr}$) is indicated as a vertical gray bar. In the bidirectional case time series for $B$ is also plotted (green dashed line). (B) Time traces for cell length (red line) and GFP fluorescence (blue line) in one independent lineage for the unidirectional and the bidirectional strains. Data from Figure 4.3 (solid red lines in that Figure).

$\langle T_A \rangle = 46 \pm 13$ min, respectively. For $\eta = 0.8$ the values obtained are $\langle T_L \rangle = 43 \pm 11$ min and $\langle T_A \rangle = 50 \pm 16$ min (see Figure 4.9). Hence, the mean values and deviations of the periods obtained in simulations are in agreement with the experimental ones.

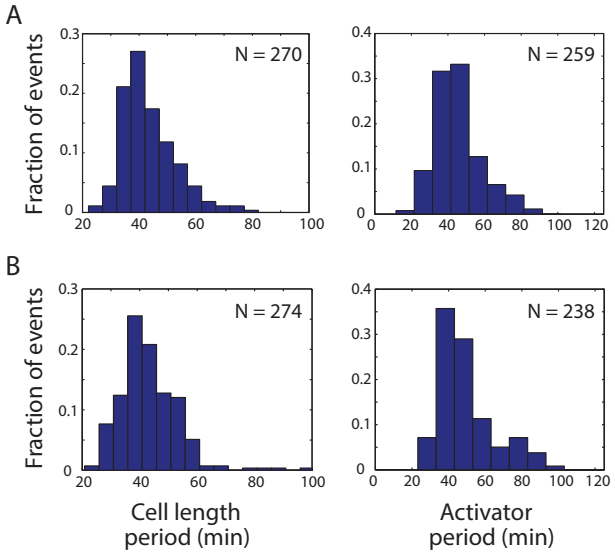


Figure 4.9: **Theoretical distributions of the periods of the cell cycle and synthetic oscillators.** (A) Unidirectional case ($\eta = 0$), for these data period mean value plus/minus standard deviation of the mean were obtained for the cell cycle, $\langle T_L \rangle = 44 \pm 10$ min, and the synthetic oscillator, $\langle T_A \rangle = 46 \pm 13$ min. (B) Bidirectional case ($\eta = 0.8$), $\langle T_L \rangle = 43 \pm 11$ min and $\langle T_A \rangle = 50 \pm 16$ min.

In order to quantify the phase shift between the cell cycle and the synthetic oscillator, we assigned a phase to simulated time series in exactly the same way as we did for experimental data (see Section 4.2). The results for the unidirectional ($\eta = 0$) and the bidirectional ($\eta = 0.8$) cases are plotted in Figure 4.10, where the distributions of the timing of activator concentration maximums within a cell length cycle are shown

for each case. Again, phase has been redefined so that 0.6 indicates the instant when cell length is minimal whereas 0.5 indicates the moment when length is maximal. Results are in good agreement with the experimental ones, showing that only the histogram for the bidirectional case, $\eta = 0.8$, emerges as a unimodal peaked distribution (see Figure C.3 for an intermediate coupling intensity of $\eta = 0.4$). This confirms that synchronization between the two oscillators increases with back-coupling.

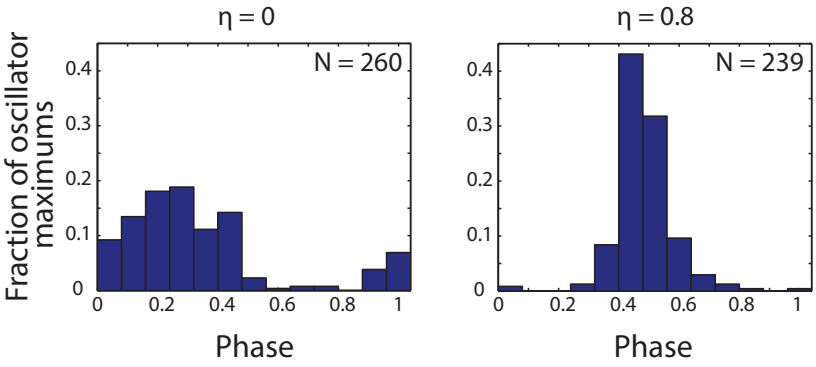


Figure 4.10: **Phase shift between the two simulated oscillators.** Histograms of the timing of activator concentration maxima within a cell length cycle are plotted for the unidirectional ($\eta = 0$, left panel) and bidirectional ($\eta = 0.8$, right panel) cases. As in Section 4.2, phase has been redefined so that 0.6 corresponds to $L$ being minimum and 0.5 to it being maximum. These results are in agreement with the experimental ones (Figure 4.5).

## 4.4 *Discussion*

The correct functioning of cells requires the orchestration of multiple cellular processes, many of which are inherently dynamical. The conditions under which these dynamical processes, such as genetic oscillations, entrain each other remain unclear. In this Chapter we have used synthetic biology to address this question. Specifically, we have studied at the single-cell level the interaction between the bacterial cell cycle and a robust synthetic oscillator in *E. coli*. Our results show that cell replication and division are able to entrain the synthetic oscillations consistently under normal growth conditions, by driving the periodic replication of the genes involved in the oscillator. In Figure 4.11 we have considered the theoretical case in which the synthetic oscillator is not driven by bacterial cell cycle, nor back-coupled to replication. Panel B shows the histogram of the timing of activator concentration maxima within a cell length cycle. Phases have been redefined as in Section 4.2. Comparing this histogram with the one in Figure 4.10 (for $\eta = 0$, left panel) we can appreciate that in the latter case the synthetic oscillator is entrained by cell cycle, in contrast with the situation depicted in this Figure.

However, it is only when the synthetic oscillations are coupled back into the cell cycle via the expression of a key regulator of chromosome replication, that the synchronization between the two periodic processes increases. A computational toy model allows us to confirm this effect.

Still, the proposed toy model has some limitations. In the limit of high back-coupling ($\eta \to 1$) the temporal window between chromosomal replication and cell division tends to disappear, resulting in an unrealistic scenario. Hence, further work should include defining a minimum

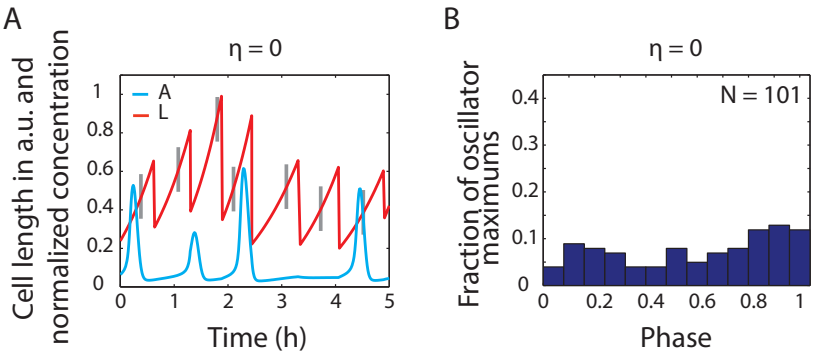


Figure 4.11: **Time series and phase shift between the two independent oscillators.** We have considered the theoretical case in which the synthetic oscillator is not driven by bacterial cell cycle, nor back-coupled to replication. (A) Time series for cell length ($L$), in red, and the normalized concentration of the activator ($A$), in blue, are plotted. In every cell cycle, replication threshold ($R_{thr}$) is indicated as a vertical gray bar. Periods for cell length and the synthetic oscillator are $\langle T_L \rangle = 45 \pm 10$ min and $\langle T_A \rangle = 120 \pm 70$ min, respectively. (B) Histogram of the timing of activator concentration maxima within a cell length cycle is plotted. As in Section 4.2 phase has been redefined so that 0.6 corresponds to $L$ being minimum and 0.5 to it being maximum.

time interval between replication and division events, as well as implementing a stochastic version of the model (so that variability is generated intrinsically).

# *IV*
# *Final remarks and outlook*

# 5
# Conclusion

In this Thesis we have used time-lapse fluorescence microscopy and dynamical systems theory to study how different cellular processes dynamically coupled give rise to well defined phenotypes. In particular, we have focused on the study and control of the coupling for two types of cellular dynamics: pulses of protein expression/activation and periodic oscillations.

The fruitful collaboration between experiments and theory deserves a special mention in the research on the gene regulatory network controlling competence. Up to now, certain studies identified competence as a bistable phenomenon [Maamar and Dubnau, 2005], whereas others described it as an excitable system [Süel et al., 2006, 2007]. Our experimental and theoretical work demonstrated that the circuit governing competence responds in one way or the other depending on the intensity of the stress applied to the cell, thus reconciling two competing views.

Another example of prolific interplay between experimental and theoretical research is the study on sigma factors. In a joint effort with our collaborators, we revealed for the first time that several alternative sigma factors in stressed *B. subtilis* cells present pulses in their activation. This intriguing behavior led us to postulate a new mechanism that could explain the partition allocation of RNAP, a common limited resource for sigma factors. The traditional "concentration sharing" strategy, in which a common resource is distributed equitably between different biomolecular species, cannot explain the observed sigma factor dynamics. Hence, we here propose a new mechanism that consists in sigma factors taking turns to use most of the available RNAP at once. We call this mechanism "time-sharing".

These two cases exemplify the quest led by physicists and other quantitative scientists to integrate all the information arising in the field of dynamical systems biology, and elaborate hypothesis that can in turn be tested experimentally. This rigorous approach should allow us to discover the "laws" of biology.

## *Summary of results and outlook*

### *Dynamics in competence*

Living organisms are subject to multiple simultaneous signals that provide them with information about their surrounding environment and internal state. Their appropriate response depends on the integration of these coupled inputs. Previous studies that aimed to understand signal integration in gene regulation have mainly focused on mapping the combinatorial response of bacteria to multiple environmental signals by measuring the expression of a single promoter [Kaplan et al., 2008, Krishna et al., 2009, Davidson et al., 2010, Hunziker et al., 2010, Silva-Rocha and de Lorenzo, 2011]. However, in many cases different inputs affect different genes or proteins, being the network itself the one that integrates the information at the system's level instead of dealing with the individual response of a particular promoter. In this way, it is necessary to understand how the integrated response of gene regulatory networks depends on the specific entry points of the inputs. We have shown that the integrated response of the circuit regulating competence in *B. subtilis* results in well defined phenotypes depend-

ing on the inputs applied to the system. Specifically, we have shown that the integrated response of the constitutive expression of ComK (one of the two master regulators of competence in *B. subtilis*) coupled to a high level of environmental stress (which affects the other regulator of the competence circuit, ComS) eliminates sporulation and normal vegetative growth, although no single input prevents these two cellular states simultaneously. The phenotypical effects reported in Chapter 2 of this Thesis are caused by changes in the dynamical behavior of the underlying genetic circuit. The stability analysis of a theoretical model of the competence circuit establishes the various dynamical regimes that the circuit can exhibit, which are in very good quantitative agreement with experimental results.

In this work we have perturbed two inputs of different nature: a contextual signal on the one hand (corresponding to modifying the level of constitutive expression of a certain protein, in a continuous way), and a copy number variation of a particular gene on the other. The effects of perturbing one of these two inputs individually has been assessed in recent studies [Cotterell and Sharpe, 2010, Conrad et al., 2010, DeLuna et al., 2008, Gruber et al., 2012], however little is known about the integration of those two levels of cellular control. These coupled perturbations could be applied to other gene regulatory networks to deeper explore the relation between structure and function in cellular networks.

An interesting application derived from the work presented here, is the possibility of quantifying the biological inputs applied to the cell. This allows a quantitative comparison with the corresponding theoretical model of the system. In this regard, we could take advantage of some of the techniques used in Chapter 2 and apply them to the study of the coupled oscillators exposed in Chapter 4. Hence, establishing the exact copy number of each of the three plasmids that compose the unidirectional and the bidirectional strains, we could chromosomally integrate all the elements now contained in the plasmids preserving the current copy number equilibrium (as it seems this has a non-neglectable effect on the synthetic oscillator [Stricker et al., 2008]). Varying the specific locations of the integration sites in the genome, we could test if replication delays between the coupled elements (due to their ubication at different distances to *oriC*) disrupt the entrainment of the synthetic oscillations by cell cycle. Still following, we could even quantify the back-coupling strength in the bidirectional strain, using the "normalization method" exposed, in order to be able to unambiguously identify the same regime in the model.

### *Dynamics in sigma factors*

In collaboration with Prof. M. Elowitz's lab from the California Institute of Technology, we have investigated the dynamical coupling between pulses of protein activity inside a single cell. The object of our study were the sigma factor family in *B. subtilis*. These proteins reversibly bind to core RNA polymerase conferring the formed holoenzyme promoter recognition specificity. In this way, alternative sigma factors have a tight control of the transcriptional programs that are triggered in response to several environmental stresses and other stimuli [Helmann and Chamberlin, 1988, Gruber and Gross, 2003]. We have shown for the first time that several alternative sigma factors are activated following a pulsatile dynamics when the cell is under energy stress, and that these pulses are generated stochastically and occur in conditions of competition for core RNAP. Considering these results, we have proposed a new mechanism, "time-sharing", in which sigma factors take turns in order to use most of the available RNAP, being only one or a few sigma factors simultaneously active in a given cell. Finally, we have developed several mathematical models that shed light on how pulsing and competition affect RNAP allocation.

The model predicts that one pulsing sigma factor would be strongly anti-correlated with all the other sigma factors. This prediction presents several challenges when attempting to test it experimentally. In order to quantify anti-correlations, the time series need to be long enough to be able to extract some information from fairly noisy data. This implies some challenging technical issues regarding how microcolonies are grown during imaging, which our collaborators are currently trying to address.

In this work, we have also shown that sigma factors compete by controlling the expression of ectopic $\sigma^B$ and checking the effect on $\sigma^W$ activity, in a strain where the $\sigma^B$ operon had been knocked out. For the competition experiment, instead of overexpressing $\sigma^B$ another option would be using gene 28 of the *B. subtilis* bacteriophage

SPO1 (sigma_gp28). This gene is a sigma factor itself, responsible for recruiting the RNAP so that the transcription of the phage middle stage infection genes begins [Lee and Pero, 1981, Costanzo and Pero, 1983]. The advantage of using the bacteriophage sigma factor is that in a genetic background of a non-infected cell, the holoenzyme formed by the core RNAP and the bacteriophage sigma factor would not have any target promoter (except for the reporter we would introduce). So in principle we could assure we would not interfere, except for reducing the pool of available RNAP, which is precisely the desired effect in the competition experiment. However, the gene 28 promoter recognition sequences in the -35 and in the -10 regions contain several bases corresponding to the thymine analog 5-hydroxymethyluracil [Lee and Pero, 1981]. Some authors studied if having "common" thymine instead of this thymine analog in the promoter sequence could result in a decrease of binding affinity between RNAP-sigma_gp28 holoenzyme and the promoter. Choy *et al.* created two hybrid promoters partially substituting the thymine analog bases for "common" thymine in one of the two conserved regions that Lee *et al.* found [Choy et al., 1986], and they saw a weaker interaction between these two hybrid promoters and the RNAP-sigma_gp28 complex. This issue could be insignificant if a bright enough fluorescent reporter could compensate the transcription deficiency effect. But it obviously requires a fairly accurate experimental characterization.

This also brings up another question. The SPO1 bacteriophage presents more genes like sigma_gp28, that is sigma factor analogs. This is the case of genes 33 and 34 responsible for the transcription of phage infection late genes [Costanzo and Pero, 1983]. It would be very exciting to monitor which is the dynamics of the SPO1 phage infection, and check what are the possible advantages of having the different stages of infection controlled by sigma factor analogs instead of, for instance, transcription factors.

### *Coupling oscillators*

Genetic oscillators are found in many organisms and part of their importance resides in their role controlling some key processes in living systems, such as repair mechanisms [Lahav, 2004], and metabolic [Kaasik and Lee, 2004] and signalling pathways [Covert et al., 2005]. These processes do not take place in isolation but occur simultaneously inside the cell. Thus it is necessary to understand how these genetic oscillators interact with each other in order to propagate information and generate specific phenotypes. We have studied a natural oscillator, such as the bacterial cell cycle in *E. coli*, and a synthetic one, developed in Prof. J. Hasty laboratory at the University of California San Diego [Stricker et al., 2008], to quantify the level of entrainment between these two oscillators. We have shown that the bacterial cell cycle is able to entrain the synthetic oscillations consistently under normal growth conditions, by driving the periodic replication of the genes involved in the oscillator. We have also shown that synchronization between the two periodic processes increases when the synthetic oscillator is coupled back to cell cycle via the expression of an inhibitor of replication initiation. We have also developed a computational toy model that confirmed this effect.

Checking whether increasing the period difference between the two oscillators has an impact in the loss of synchronization for the back-coupled system is an interesting question. This is a feasible experiment given that the synthetic oscillator was designed to have a tunable period depending on the concentration of inductors. Moreover, the cell cycle period can also be modified by changing the culture media.

Another possibility to explore would be to maximize the back-coupling by knocking out genomic *hda* and replacing wild-type genomic *dnaN* by the thermosensitive mutation *dnaN159ts* in the bidirectional strain. dnaN159ts folds into a functional protein when the temperature is around 30 °C and into a totally non-functional form at around 40 °C [Grompone et al., 2002, Maciag et al., 2011]. In this way, as the $P_{lac/ara}$ promoter would express the wild-type dnaN, increasing the temperature would only affect the genomic contribution portion (thermosensitive dnaN). This would allow us to control a natural oscillator vital for cell survival, as is replication, via the synthetic oscillator.

# *V*
# *Appendix*

# A
# Materials and Methods for Chapter 2

In this Appendix we have included a compilation of supporting information for the work exposed in Chapter 2.

## A.1 Growth conditions for microscopy

For the experiments with baseline stress conditions, *B. subtilis* cells were grown at 37°C in Luria Broth (Miller's modification) (LB) with appropriate antibiotics for selection, added to the following final concentrations: 10 $\mu$g/ml spectinomycin, 5 $\mu$g/ml chloramphenicol, 5 $\mu$g/ml kanamycin, and 5 $\mu$g/ml erythromycin. Cells were grown to an OD of 1.8 and resuspended in 0.5 volume of resuspension media (RM) (composition per 1 L: 0.046 mg $FeCl_2$, 4.8 g $MgSO_4$, 12.6 mg $MnCl_2$, 535 mg $NH_4Cl$, 106 mg $Na_2SO_4$, 68 mg $KH_2PO_4$, 96.5 mg $NH_4NO_3$, 219 mg $CaCl_2$, 2 g L-glutamic acid) [Sterlini and Mandelstam, 1969]. The cells were incubated at 37°C for 1.5 h, then diluted 10-fold in RM and spotted onto a 1.5% (w/v) low-melting agarose pad placed into a coverslip-bottom Willco dish for imaging. When necessary, IPTG was added to cultures and agarose pads at a final concentration of 3, 5, 10, or 100 $\mu$M.

For the general stress experiments, *B. subtilis* cells were grown overnight at 30°C in LB without antibiotics. Then, cells were diluted to an OD of 0.1 into 10 mL of LB (1:20) in Phosphate-Buffered Saline (PBS) and incubated at 37°C for a time period ranging from 4 to 6 h. Finally, cells were diluted to a final OD = 0.1–0.12 and placed into a 2% (w/v) low-melting agarose pad made of conditioned medium (1:30; prepared as described below) in PBS enriched with L-glutamate at a final concentration of 0.21% (w/v). When necessary, IPTG was added to cultures and agarose pads at a final concentration of 5 $\mu$M. Conditioned media was prepared growing PY79 wild-type *B. subtilis* strain in 2 mL of LB at 37°C for 4.5 h. Then, this culture was diluted in 23 mL of fresh LB and was grown at 37°C for 17.5 h. After this, cells were removed by centrifugation (at 3000 × *g* for 10 min) and the supernatant was sterilized by filtration (using 0.2-$\mu$m pore-size filters) and stored at −80°C. This is a variation of the conditioned media used in previous works [Çagatay et al., Locke et al., 2011].

All data were acquired imaging *B. subtilis* microcolonies in the pads at 37°C with a Nikon TE2000 inverted microscope and a motorized stage (Prior). Images were acquired every 20 min with a Hamamatsu ORCA-ER camera. Imaging time was optimized to prevent phototoxicity [Süel et al., 2006]. The NIS-Elements software was used to automate image acquisition and microscope control. Data analysis of time-lapse movies was performed by custom software developed with MATLAB image processing and statistics toolboxes (MathWorks).

## *A.2 Strain construction*

The strains 75xS and Control-$\beta$S-75xS were constructed from the plasmid pDG148, kind gift of Beth A. Lazazzera (UCLA). Native $P_{comS}$-*comS* and $P_{comS}$-*cfp* constructs were amplified by standard PCR techniques and were cloned into pDG148 using EcoRV and BamHI restriction sites. The cloned plasmids were transformed into the strains containing chromosomally integrated $P_{comG}$-*cfp* and $P_{comS}$-*yfp* reporters (V10) and $P_{hyp}$-*yfp* (Control-$\alpha$).

For the construction of the Control-$\beta$S-6xS strain we used the low-copy number plasmid pHP13 [Haima et al., 1987]. Standard PCR techniques were used to amplify a $P_{comS}$-*cfp* construct, that was cloned into pHP13 using SmaI and BamHI restriction sites. This plasmid was then transformed into the strain containing chromosomally integrated $P_{hyp}$-*yfp* (Control-$\alpha$).

The strain Norm-$\beta$S was obtained by integrating the construct $P_{comS}$-*cfp* into the *amyE* locus using the pDL30 plasmid (kind gift from Jonathan Dworkin, Columbia University).

The Hyper-$\alpha$K-6xS and Hyper-$\alpha$K-75xS strains were obtained by transformation of the plasmids pHP13::$P_{comS}$-*comS* and pDG148::$P_{comS}$-*comS*, respectively, into the Hyper-$\alpha$K strain.

## *A.3 Discrete simulations of the competence circuit*

Discrete simulations of the competence circuit were performed using Gillespie's first reaction method [Gillespie, 1977]. The simulated biochemical reactions are detailed in Table A.1. In this table, $P_i^{(c)}$ and $P_i$ are the constitutive and regulated promoters of their corresponding genes ($K$ for ComK and $S$ for ComS), $K$ and $S$ are the number of ComK and ComS molecules, respectively, $m_K$ and $m_S$ are the mRNAs for ComK and ComS, respectively, $k_i$ are the reaction rates and $\Omega$ represents a volume factor, which we take to be equal to 1 molec/nM [Süel et al., 2007]. The transcriptional regulation of each gene is represented by the following Hill functions:

$$f(K, k_2, k_k, n) = \frac{k_2 (K/\Omega)^n}{k_k^n + (K/\Omega)^n}, \qquad g(K, k_5, k_s, p) = \frac{k_5}{1 + (K/(\Omega k_s))^p}$$

| | |
|---|---|
| **Transcription** | |
| $P_K^{(c)} \xrightarrow{k_1} P_K^{(c)} + m_K$ | (a) |
| $P_K \xrightarrow{f(K,k_2,k_k,n)} P_K + m_K$ | (b) |
| $P_S^{(c)} \xrightarrow{k_4} P_S^{(c)} + m_S$ | (c) |
| $P_S \xrightarrow{g(K,k_5,k_s,p)} P_S + m_S$ | (d) |
| **Translation** | |
| $m_K \xrightarrow{k_3} m_K + K$ | (e) |
| $m_S \xrightarrow{k_6} m_S + S$ | (f) |
| **mRNA degradation** | |
| $m_K \xrightarrow{k_7} \varnothing,$ | (g) |
| $m_S \xrightarrow{k_9} \varnothing,$ | (h) |
| **Protein degradation** | |
| $K \xrightarrow{k_8} \varnothing,$ | (i) |
| $S \xrightarrow{k_{10}} \varnothing,$ | (j) |
| **Competitive enzymatic degradation** | |
| $MecA + K \xrightarrow{k_{11}/\Omega} MecA_K,$ | (k) |
| $MecA_K \xrightarrow{k_{-11}} MecA + K,$ | (l) |
| $MecA_K \xrightarrow{k_{12}} MecA,$ | (m) |
| $MecA + S \xrightarrow{k_{13}/\Omega} MecA_S,$ | (n) |
| $MecA_S \xrightarrow{k_{-13}} MecA + S,$ | (o) |
| $MecA_S \xrightarrow{k_{14}} MecA.$ | (p) |

Table A.1: **Set of reactions for the discrete competence circuit.** Adapted from [Espinar et al., 2013].

where $k_k$ ($k_s$) represent the concentration of ComK for which the activation of ComK (repression of ComS) is half-maximal. The number of MecA molecules is conserved, here we assumed it to be equal to 1000 molecules. The values of the reaction rates, which are compatible with the values of the parameters of the deterministic model according to the conversion rules given in [Süel et al., 2007], are listed in Table A.2.

| Par. | Value | Units | Par. | Value | Units |
|---|---|---|---|---|---|
| $k_1$ | $6.25 \times 10^{-5}$ | $s^{-1}$ | $k_{10}$ | 0.0001 | $s^{-1}$ |
| $k_2$ | 0.156 25 | $s^{-1}$ | $k_{11}$ | $1.02 \times 10^{-6}$ | $s^{-1}$ |
| $k_3$ | 0.2 | $s^{-1}$ | $k_{-11}$ | 0.0005 | $s^{-1}$ |
| $k_4$ | 0.0 | $s^{-1}$ | $k_{12}$ | 0.025 | $s^{-1}$ |
| $k_5$ | 0.000 25 | $s^{-1}$ | $k_{13}$ | $3.5 \times 10^{-6}$ | $s^{-1}$ |
| $k_6$ | 0.2 | $s^{-1}$ | $k_{-13}$ | $5 \times 10^{-5}$ | $s^{-1}$ |
| $k_7$ | 0.005 | $s^{-1}$ | $k_{14}$ | $2 \times 10^{-5}$ | $s^{-1}$ |
| $k_8$ | 0.0001 | $s^{-1}$ | $k_k$ | 5000 | molec |
| $k_9$ | 0.005 | $s^{-1}$ | $k_s$ | 1562 | molec |

Table A.2: **Values of the reaction rates used in the stochastic simulations of the competence circuit.** Adapted from [Espinar et al., 2013].

| Strain name | Genotype | Reference |
|---|---|---|
| V10 | *AmyE*::$P_{comG}$-*cfp*-$P_{comS}$-*yfp* | [Süel et al., 2006] |
| 6xS | *AmyE*::$P_{comG}$-*cfp*-$P_{comS}$-*yfp* | |
| | pHP13::$P_{comS}$-*comS* | [Süel et al., 2007] |
| 75xS | *AmyE*::$P_{comG}$-*cfp*-$P_{comS}$-*yfp* | |
| | pDG148::$P_{comS}$-*comS* | This study |
| Hyper-$\alpha$K | *AmyE*::$P_{hyp}$-*comK* | |
| | *SacA*::$P_{comG}$-*cfp*$P_{comS}$-*yfp* | This study |
| Hyper-$\alpha$K-6xS | *AmyE*::$P_{hyp}$-*comK* | |
| | *SacA*::$P_{comG}$-*cfp*$P_{comS}$-*yfp* | |
| | pHP13::$P_{comS}$-*comS* | This study |
| Hyper-$\alpha$K-75xS | *AmyE*::$P_{hyp}$-*comK* | |
| | *SacA*::$P_{comG}$-*cfp*$P_{comS}$-*yfp* | |
| | pDG148::$P_{comS}$-*comS* | This study |
| KG | *AmyE*::$P_{comG}$-*cfp*-$P_{comK}$-*yfp* | [Süel et al., 2006] |
| Control-$\alpha$ | *AmyE*::$P_{hyp}$-*yfp* | [Süel et al., 2007] |
| Control-$\beta$S-6xS | *AmyE*::$P_{hyp}$-*yfp* | |
| | pHP13::$P_{comS}$-*cfp* | This study |
| Control-$\beta$S-75xS | *AmyE*::$P_{hyp}$-*yfp* | |
| | pDG148::$P_{comS}$-*cfp* | This study |
| Norm-$\beta$S | *AmyE*::$P_{comS}$-*cfp* | This study |

Table A.3: **Strains used in the work explained in Chapter 2.** Adapted from [Espinar et al., 2013].

| Strain name | 15 h | SEM | n | 20 h | SEM | n | 30 h | SEM | n |
|---|---|---|---|---|---|---|---|---|---|
| KG | 6.12 | 1.99 | 77 | 4.63 | 2.25 | 52 | - | - | - |
| Control-$\alpha$ 0 µM IPTG | 3.14 | 0.87 | 118 | 1.79 | 0.81 | 107 | 1.56 | 0.79 | 48 |
| Control-$\alpha$ 3 µM IPTG | 8.32 | 1.94 | 160 | 7.22 | 1.87 | 251 | 6.27 | 1.70 | 86 |
| Control-$\alpha$ 5 µM IPTG | 14.39 | 4.34 | 207 | 11.15 | 2.81 | 131 | 11.44 | 3.47 | 55 |
| Control-$\alpha$ 10 µM IPTG | 36.31 | 10.98 | 217 | 27.14 | 6.96 | 203 | 25.69 | 6.82 | 73 |
| Control-$\alpha$ 100 µM IPTG | 126.30 | 30.14 | 214 | 141.13 | 31.16 | 250 | 139.93 | 23.25 | 96 |

Table A.4: **Fluorescence of control strains at 0, 3, 5, 10 and 100 $\mu$M of IPTG concentration, at 15, 20 and 30 h (in arbitrary units).** Adapted from [Espinar et al., 2013].

| IPTG ($\mu$M) | $\beta_s$ = 1 (n) | Prob. (%) | SEM | $\beta_s$ = 6.5 (n) | Prob. (%) | SEM | $\beta_s$ = 75 (n) | Prob. (%) | SEM |
|---|---|---|---|---|---|---|---|---|---|
| wt | 11/534 | 2.26 | 0.26 | 38/781 | 4.90 | 0.42 | 243/1485 | 16.86 | 1.35 |
| 0 | 12/388 | 3.37 | 0.39 | 46/243 | 18.05 | 2.17 | NA | 100.00 | NA |
| 3 | 95/546 | 17.39 | 1.56 | 175/329 | 54.36 | 3.67 | NA | 100.00 | NA |
| 5 | 464/695 | 64.95 | 4.03 | NA | 100.00 | NA | NA | 100.00 | NA |
| 10 | 131/193 | 67.90 | 2.86 | NA | 100.00 | NA | NA | 100.00 | NA |
| 100 | NA | 100.00 | NA | NA | 100.00 | NA | NA | 100.00 | NA |

Table A.5: **Probability of initiation for varying $\alpha_k$ and $\beta_s$.** n = fraction of initiation of competence events with respect to all cell divition events; SEM = standard error of the mean; wt = wild type; NA = not applicable, all cells enter in competence. Adapted from [Espinar et al., 2013].

| IPTG ($\mu$M) | $\beta_s$ = 1 (n) | Prob. (%) | SEM | $\beta_s$ = 6.5 (n) | Prob. (%) | SEM | $\beta_s$ = 75 (n) | Prob. (%) | SEM |
|---|---|---|---|---|---|---|---|---|---|
| wt | 88/147 | 61.12 | 3.41 | 57/122 | 48.77 | 4.86 | 12/287 | 4.12 | 0.32 |
| 0 | 16/26 | 62.14 | 3.54 | 12/380 | 3.19 | 0.57 | 10/340 | 2.95 | 0.17 |
| 3 | 45/74 | 61.55 | 2.49 | 13/405 | 3.18 | 0.54 | 9/360 | 2.56 | 0.56 |
| 5 | 63/115 | 55.39 | 3.72 | 12/435 | 2.79 | 0.29 | 7/350 | 2.01 | 1.8 |
| 10 | 58/103 | 56.71 | 2.95 | NA | 0.00 | NA | NA | 0.00 | NA |
| 100 | NA | 0.00 | NA | NA | 0.00 | NA | NA | 0.00 | NA |

Table A.6: **Probability of exit for varying $\alpha_k$ and $\beta_s$.** n = fraction of competent cells that successfully leave the competence state with respect to all competence events; SEM = standard error of the mean; wt = wild type; NA = not applicable, cells do not exit competence. Adapted from [Espinar et al., 2013].

| IPTG ($\mu$M) | $\beta_s$ = 1 (n) | Prob. (%) | SEM | $\beta_s$ = 6.5 (n) | Prob. (%) | SEM | $\beta_s$ = 75 (n) | Prob. (%) | SEM |
|---|---|---|---|---|---|---|---|---|---|
| wt | 6/213 | 2.38 | 0.92 | 9/240 | 2.96 | 1.01 | 8/192 | 2.93 | 1.09 |
| 0 | 7/121 | 3.47 | 1.58 | 2/66 | 3.06 | 0.28 | 2/78 | 2.57 | 0.07 |
| 3 | 15/75 | 21.20 | 4.49 | 1/52 | 2.08 | 2.08 | 1/42 | 2.08 | 2.08 |
| 5 | 84/262 | 33.02 | 3.59 | 2/73 | 2.77 | 0.27 | 1/62 | 1.56 | 1.56 |
| 10 | 69/142 | 50.43 | 2.99 | NA | 0.00 | NA | NA | 0.00 | NA |
| 100 | NA | 0.00 | NA | NA | 0.00 | NA | NA | 0.00 | NA |

Table A.7: **Probability of reinitiation for varying $\alpha_k$ and $\beta_s$.** n = fraction of competent cells that after leaving competence, go back into this state within two cell cycles, with respect to all competence events; SEM = standard error of the mean; wt = wild type; NA = not applicable, cells do not reinitiate competence. Adapted from [Espinar et al., 2013].

# B
# *Materials and Methods for Chapter 3*

In this Appendix we have included a compilation of supporting information for the work exposed in Chapter 3.

## *B.1 Strain construction*

*E. coli* strain DH5$\alpha$ was used to clone all plasmids using standard molecular cloning techniques. In turn, plasmids constructs were integrated into *B.subtilis* chromosomal loci via double crossover using standard techniques. All strains were constructed from PY79 wild-type *B.subtilis*. Many starting strains/genomic DNA were kind gifts of C.W. Price (see references in Table B.3).

| | Plasmid name | Description | Source |
|---|---|---|---|
| 1 | ppsB::$P_{trpE}$-mCherry $Erm^R$ | This plasmid provides uniform expression from mCherry from a $\sigma^A$ dependent promoter, so that time-lapse images can be automatically segmented during movie analysis. The $\sigma^A$ dependent promoter used is the one from TrpE gene; it was cloned into a vector with ppsB homology regions [Locke et al., 2011] | The original integration vector was a gift from A. Eldar [Eldar et al., 2009] |
| 2 | sacA::$P_{sig\square}$-yfp $Cm^R$ | Target promoters of each alternative sigma factor $\square$ = B, D, L, M, W, X, Y, were cloned into the EcoRI/BamHI sites of AEC127. | [Eldar et al., 2009] |
| 3 | amyE::$P_{sig\square}$-3 × cfp $Spect^R$ | Target promoters of each alternative sigma factor $\square$ = B, D, L, M, W, X, Y, were cloned into the EcoRI/NheI sites of plasmid pDR-111. | pDR-111 was a gift of D. Rudner (Harvard) |
| 4 | amyE::$P_{hyperspank}$-sigB $Spect^R$ | $\sigma^B$ gene followed by a 5' transcriptional terminator was cloned behind the $P_{hyperspank}$ IPTG-inducible promoter in plasmid pDR-111. | pDR-111 was a gift of D. Rudner (Harvard) |
| 5 | pyrD::$P_{sigB}$-cfp $Kan^R$ | $\sigma^B$ target promoter followed by CFP fluorescent protein gene was cloned into the EcoRI/BseRI site of the ECE171 plasmid. | [Middleton and Hofmeister, 2004] |

Table B.1: **Plasmid list.** Adapted from J.C.W.Locke and J.Park [Locke et al., 2014].

| Target promoter | Sequence | Reference |
|---|---|---|
| $\sigma^B$ | 5'-GTTTCTTGGAGCGTCCTGATCTGCAGAAGCTCATT GAGGAACATATGTGTTCCTCTGCGCAGGAAATGGTCAAAAAC ATTTATGACAGCCTCCTCAAATTGCAGGATTTTCAGCTT CACGATGATTTTACGTTAATTGTTTTGCGGAGAAAGGTT TAACGTCTGTCAGACGAGGGTATAAAGCAACT AGTGATTTGAAGGAAAATTTG - 3' | Sequence was chosen from the $\sigma^B$ binding site upstream of the rsbV gene [Kalman et al., 1990, Boylan et al., 1993]. |
| $\sigma^D$ | 5' – TTTTGCATTTTTCTTCAAAAAGTTTCAAAAA TGCCGAAAAGAAAGGAGAAAAAACAGAAATTCTG – 3' | Sequence was chosen from the $\sigma^D$ binding site upstream of the flgB gene [Estacio et al., 1998]. |
| $\sigma^L$ | 5' – AATATGGCCTTGCAAATGAAGGCATGCAATAATTT GCAGAATAAACGCAAACATCTGCACGAATGTTTCGGTATACCT GGTATGACAGCACCCTTAAGAGCTGGCATGGAA CTTGCATAATAAAAGGCGGAG – 3' | Sequence was chosen from the $\sigma^L$ binding site upstream of the ptb gene [Debarbouille et al., 1999]. |
| $\sigma^M$ | 5' – TTTGCATGTAATGTGCAACTTTAAACC TTTCTTATGCGTGTATAACATAGAGG-3' | Sequence was chosen from the $\sigma^M$ binding site upstream of the sigM gene [Horsburgh and Moir, 1999]. |
| $\sigma^W$ | 5' – TTAAGAATGAAACCTTTCTGTAAAAG AGACGTATAAATAACGACGAAAAAAAG – 3' | Sequence was chosen from the $\sigma^W$ binding site upstream of the ydbS gene [Cao et al., 2002]. |
| $\sigma^X$ | 5' – TTGTAATGTAACTTTTCAAGCTATTC ATACGACAAAAAAGTGAACGGAGGG – 3' | Sequence was chosen from the $\sigma^X$ binding site upstream of the sigX gene [Huang et al., 1997]. |
| $\sigma^Y$ | 5' – GAATTGTAAAAAAGATGAACGCTTTT GAATCCGGTGTCGTCTCATAAGGCAGAAAAACA – 3' | Sequence was chosen from the $\sigma^Y$ binding site upstream of the sigY gene [Cao et al., 2003]. |

Table B.2: **Target promoters of sigma factors.** Adapted from J.C.W.Locke and J.Park [Locke et al., 2014].

| | Strain name | Genotype | Construction Procedure | Used in | Reference |
|---|---|---|---|---|---|
| 0 | PY79 | trpC2 (omitted in the derived strains below) | | | BGSC 1A776 |
| 1 | JP1 | ppsB::$P_{trpE}$-mCherry Phleo$^R$ | Plasmid (1) → PY79 Antibiotic cassette switched from Erm$^R$ to Phleo$^R$ | | [Locke et al., 2011] |
| 2 | JP2 | JP1; ytvA::Neo$^R$ | JJB751 → JP1 (with Neo$^R$ selection) | | [Locke et al., 2011] |
| 3 | JP3 | JP2; sacA::$P_{sigB}$-yfp Cm$^R$ | Plasmid (2) → JP2 | Figures 3.2 to 3.4 and B.1 to B.3 | This work |
| 4 | JP4 | JP2; sacA::$P_{sigW}$-yfp Cm$^R$ | Plasmid (2) → JP2 | Figures 3.2 to 3.4 and B.1 to B.3 | This work |
| 5 | JP5 | JP2; sacA::$P_{sigD}$-yfp Cm$^R$ | Plasmid (2) → JP2 | Figures 3.2 to 3.4 and B.1 to B.3 | This work |
| 6 | JP6 | JP2; sacA::$P_{sigL}$-yfp Cm$^R$ | Plasmid (2) → JP2 | Figures 3.2, 3.4 and B.1 to B.3 | This work |
| 7 | JP7 | JP2; sacA::$P_{sigY}$-yfp Cm$^R$ | Plasmid (2) → JP2 | Figures 3.2 to 3.4 and B.1 to B.3 | This work |
| 8 | JP8 | JP2; sacA::$P_{sigM}$-yfp Cm$^R$ | Plasmid (2) → JP2 | Figures 3.2 to 3.4 and B.1 to B.3 | This work |
| 9 | JP9 | JP2; sacA::$P_{sigX}$-yfp Cm$^R$ | Plasmid (2) → JP2 | Figures 3.2 to 3.4 and B.1 to B.3 | This work |
| 10 | JP10 | JP2; sacA::$P_{sigA}$-yfp Cm$^R$ | Plasmid (2) → JP2 | Figure 3.5 | This work |
| 11 | JP11 | JP3; amyE::$P_{sigB}$-3 × cfp Spect$^R$ | Plasmid (3) → JP3 | Figure 3.6 | This work |
| 12 | JP12 | JP3; amyE::$P_{sigD}$-3 × cfp Spect$^R$ | Plasmid (3) → JP3 | Figure 3.6 | This work |
| 13 | JP13 | JP3; amyE::$P_{sigM}$-3 × cfp Spect$^R$ | Plasmid (3) → JP3 | Figure 3.6 | This work |
| 14 | JP14 | JP3; amyE::$P_{sigX}$-3 × cfp Spect$^R$ | Plasmid (3) → JP3 | Figure 3.6 | This work |
| 15 | JP15 | JP3; amyE::$P_{sigW}$-3 × cfp Spect$^R$ | Plasmid (3) → JP3 | Figure 3.6 | This work |
| 16 | JP16 | JP4; amyE::$P_{sigB}$-3 × cfp Spect$^R$ | Plasmid (3) → JP4 | Figure 3.6 | This work |
| 17 | JP17 | JP4; amyE::$P_{sigD}$-3 × cfp Spect$^R$ | Plasmid (3) → JP4 | Figure 3.6 | This work |
| 18 | JP18 | JP4; amyE::$P_{sigM}$-3 × cfp Spect$^R$ | Plasmid (3) → JP4 | Figure 3.6 | This work |
| 19 | JP19 | JP4; amyE::$P_{sigX}$-3 × cfp Spect$^R$ | Plasmid (3) → JP4 | Figure 3.6 | This work |
| 20 | JP20 | JP4; amyE::$P_{sigW}$-3 × cfp Spect$^R$ | Plasmid (3) → JP4 | Figure 3.6 | This work |
| 21 | JP21 | JP5; amyE::$P_{sigB}$-3 × cfp Spect$^R$ | Plasmid (3) → JP5 | Figure 3.6 | This work |
| 22 | JP22 | JP5; amyE::$P_{sigD}$-3 × cfp Spect$^R$ | Plasmid (3) → JP5 | Figure 3.6 | This work |
| 23 | JP23 | JP5; amyE::$P_{sigM}$-3 × cfp Spect$^R$ | Plasmid (3) → JP5 | Figure 3.6 | This work |
| 24 | JP24 | JP5; amyE::$P_{sigX}$-3 × cfp Spect$^R$ | Plasmid (3) → JP5 | Figure 3.6 | This work |
| 25 | JP25 | JP5; amyE::$P_{sigW}$-3 × cfp Spect$^R$ | Plasmid (3) → JP5 | Figure 3.6 | This work |
| 26 | JP26 | JP8; amyE::$P_{sigB}$-3 × cfp Spect$^R$ | Plasmid (3) → JP10 | Figure 3.6 | This work |
| 27 | JP27 | JP8; amyE::$P_{sigD}$-3 × cfp Spect$^R$ | Plasmid (3) → JP10 | Figure 3.6 | This work |
| 28 | JP28 | JP8; amyE::$P_{sigM}$-3 × cfp Spect$^R$ | Plasmid (3) → JP10 | Figure 3.6 | This work |
| 29 | JP29 | JP8; amyE::$P_{sigX}$-3 × cfp Spect$^R$ | Plasmid (3) → JP10 | Figure 3.6 | This work |
| 30 | JP30 | JP8; amyE::$P_{sigW}$-3 × cfp Spect$^R$ | Plasmid (3) → JP10 | Figure 3.6 | This work |
| 31 | JP31 | JP9; amyE::$P_{sigB}$-3 × cfp Spect$^R$ | Plasmid (3) → JP11 | Figure 3.6 | This work |
| 32 | JP32 | JP9; amyE::$P_{sigD}$-3 × cfp Spect$^R$ | Plasmid (3) → JP11 | Figure 3.6 | This work |
| 33 | JP33 | JP9; amyE::$P_{sigM}$-3 × cfp Spect$^R$ | Plasmid (3) → JP11 | Figure 3.6 | This work |
| 34 | JP34 | JP9; amyE::$P_{sigX}$-3 × cfp Spect$^R$ | Plasmid (3) → JP11 | Figure 3.6 | This work |
| 35 | JP35 | JP9; amyE::$P_{sigW}$-3 × cfp Spect$^R$ | Plasmid (3) → JP11 | Figure 3.6 | This work |
| 36 | JP36 | JJB213; rsbU-rsbX::Tet$^R$ | ΔrsbU-rsbX Tet$^R$ recombination at the rsbU-rsbX locus | | This work and [Locke et al., 2011] |
| 37 | JP37 | JP1; rsbU-rsbX::Tet$^R$ | JP36 → JP1 (with Tet$^R$ selection | | This work |
| 38 | JP38 | JP37; amyE::$P_{hyperspank}$-sigB Spect$^R$ | Plasmid (4) → JP37 | | This work |
| 39 | JP39 | JP38; pyrD::$P_{sigB}$-cfp Kan$^R$ | Plasmid (7) → JP38 | | This work |
| 40 | JP40 | JP39; sacA::$P_{sigW}$-yfp Cm$^R$ | Plasmid (2) → JP39 | Figure 3.7 | This work |

Table B.3: **Strain information and construction for sigma factors.** In the column labeled as "Construction Procedure" the '→' symbol indicates an integration event from plasmid or genomic DNA into the strain after the arrow. Adapted from J.C.W.Locke and J.Park [Locke et al., 2014].

## B.2 Sample growth and imaging

The following passages have been quoted verbatim from [Locke et al., 2014] Supplementary Information:

### B.2.1 Sample preparation

Samples were prepared following a time-lapse microscopy protocol described in [Young et al., 2012]. Between days, relative lamp intensity levels were monitored by taking an image of fluorescent beads and measuring their mean intensity. Exposure times were then adjusted to keep per exposure light levels constant between experiments. For snapshots, cells were spotted on solidified 1.5% low melt agarose in PBS pads and imaged. Images were then analyzed via custom MATLAB software, where mean cell intensities were background corrected using strain JP2, which has mCherry expression for segmentation, but lacks YFP or CFP expression. For most time-lapse movies (unless otherwise specified), cells were spotted on solidified 1.5% low melt agarose in SMM pads. These prepared pads were then enclosed in coverglass bottom dishes (Wilco #HBSt-5040), sealed with parafilm or grease to prevent evaporation, and then imaged.

### B.2.2 Growth conditions

SMM is derived from Spizizen's minimal media [Spizizen, 1958], which uses 0.5% glucose as the carbon source, and tryptophan (50 $\mu$g/mL) as an amino-acid supplement. Mycophenolic acid (MPA) was dissolved in DMSO and diluted 1000 fold into working concentrations in liquid and pad conditions. IPTG was dissolved in $H_2O$ and diluted 1000 fold into working concentrations. Concentrations of 0.1% DMSO were not found to affect cell growth or $\sigma^B$ activity.

Stationary phase (conditioned medium) experiments

*Conditioned Medium Preparation:* Conditioned medium was prepared growing PY79 wild-type B. subtilis strain in 2 mL of LB at 37°C for 4.5 h. Then, this culture was diluted in 23 mL of fresh LB and was grown at 37°C for 17.5h. After this, cells were removed by centrifugation (at 5000 rpm for 10 min) and the supernatant was sterilized by filtration (using 0.2 $\mu$m pore-size filters) and stored at -80°C. This conditioned media protocol was defined in [Espinar et al., 2013].

*Time-lapse microscopy:* Cells were grown from glycerol stocks in LB until $OD_{600}$ 1.5-3.5, then diluted back into LB (1:10) in PBS to an $OD_{600}$ of 0.05. This culture was grown at 37°C for a minimum of 4 hours and a maximum of

7, when cells were diluted to an $OD_{600}$ of 0.8-0.1 with conditioned medium (1:45) in PBS for imaging. 1.5% low melting agarose pads were prepared with conditioned medium (1:45) in PBS. After allowing cells to equilibrate for 2-3 hours, time-lapse acquisition was started.

Mycophenolic Acid (MPA) experiments

*Liquid snapshots:* Cells were grown overnight from glycerol stocks in SMM to mid-log (OD 0.3-0.8) at 30°C, then diluted back in SMM to an $OD_{600}$ of 0.01 the next morning. After regrowing to $OD_{600}$ of 0.1 at 37°C, varying concentrations of MPA (MP Biomedicals cat #194172), dissolved in 1000 fold DMSO concentrate, were added to separate cultures. After 2.5 hours of MPA exposure, cells were imaged as described above.

*Time-lapse microscopy:* Protocol was similar to liquid snapshot protocol above, except when cells regrew to $OD_{600}$ of 0.1, cells were then spotted on SMM 1.5% low melt agarose pads containing various concentrations of MPA. MPA pads were prepared by taking 1 mL of the SMM/agarose mixture and adding it to 1 $\mu$L of various MPA stock concentrations. After allowing cells to equilibrate after 2-3 hours, time-lapse acquisition was started.

### *B.2.3 Quantitative analysis of time-lapse movies*

Quantitative movie analysis used custom image analysis code in MATLAB, described in previous work [Rosenfeld et al., 2005]. [...] We characterized the amplitude, duration and frequency of the pulses using custom MATLAB software [Locke et al., 2011]. The pulse amplitude and duration were obtained by calculating the pulse height and half-maximum width, respectively. Pulse frequency was defined as the number of pulses per hour. To prevent erroneous detection of non-pulse fluctuations in the traces, we imposed two criteria for pulse detection: First, we rejected pulses below a minimum amplitude cutoff. Second, we rejected pulses which contributed less than thirty percent of total gene expression over their duration, i.e. pulses that were relatively small compared to the basal expression rates.

### *B.2.4 Competition assay*

For the competition assay, strain JP40 was inoculated from glycerol stock into SMM minimal media (plus glucose, tryptophan, 40 $\mu$g/mL uracil and trace elements), and then grown overnight at 30°C. The following morning, cultures were diluted to 0.01 $OD_{600}$ in SMM, and then regrown to 0.1 $OD_{600}$ at 37°C. After regrowth, the culture was split in two. One culture received MPA

(40 $\mu$g/mL) and IPTG (100 $\mu$M), while the other culture received only MPA. All cultures were then grown at 37°C for an additional 2 h. Following this 2 h incubation, cells were harvested for microscopy (using imaging protocol described above).

### *B.2.5 Microscopy*

All data were acquired using a CoolSnap HQ2 attached to a Nikon inverted TI-E microscope, equipped with the Nikon Perfect Focus System (PFS) hardware autofocus module. Molecular Devices commercial software (Metamorph 7.5.6.0) controlled microscope, camera, motorized stage (ASI instruments), and epifluorescent and brightfield shutters (Sutter Instruments). Epi-illumination was provided by a 300 W Xenon light source (LamdbaLS, Sutter instruments) connected via a liquid light guide into the illuminator of the scope. Phase contrast illumination was provided by a halogen bulb to allow verification of cell focus and cell shape. Temperature control was achieved using an enclosed microscope chamber (Nikon) attached to a temperature sensitive heat exchanger set to 37°C. All experiments used a Phase 100x Plan Apo (NA 1.4) objective. Chroma filter sets used were as follows: #41027 (mCh), #41028 (YFP), and #31044v2 (CFP). The interval between consecutive imaging was 15-20 minutes.

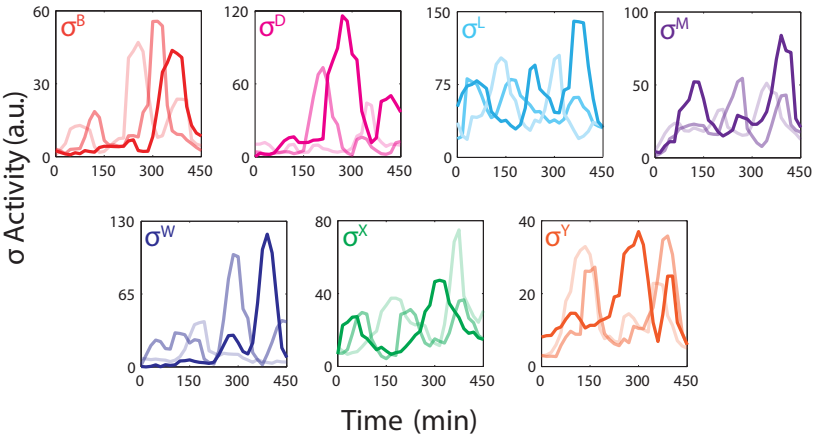


Figure B.1: **Multiple sigma factors pulse under energy stress conditions.** Alternative sigma factor reporter strains were grown separately/individually in a minimal medium containing 40 $\mu$g/ml MPA. Each panel shows 3 representative time traces of a lineage with pulsatile dynamics. Adapted from J.C.W.Locke and J.Park [Locke et al., 2014].

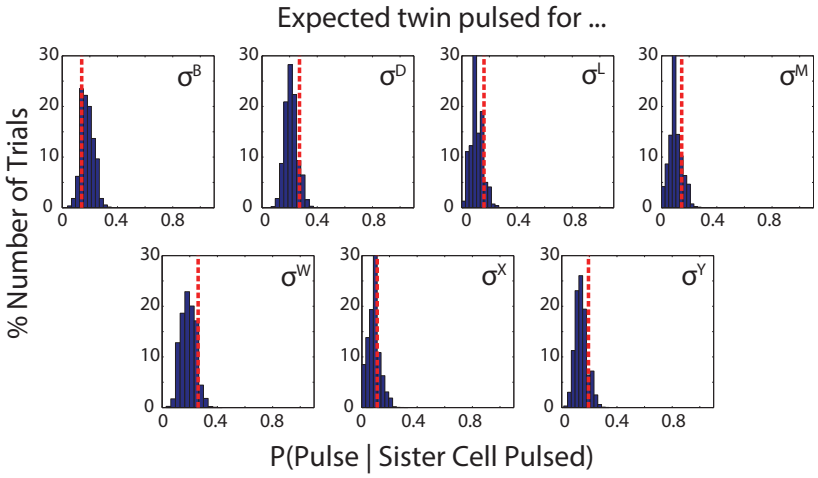


Figure B.2: **No correlations observed between sister cells.** Blue histograms show expected probabilities that a cell pulses in the event that her twin cell pulses, in a bootstrap model where sister cell pulses are randomized. Red dashed line indicates measured probability. Adapted from J.C.W.Locke and J.Park [Locke et al., 2014].

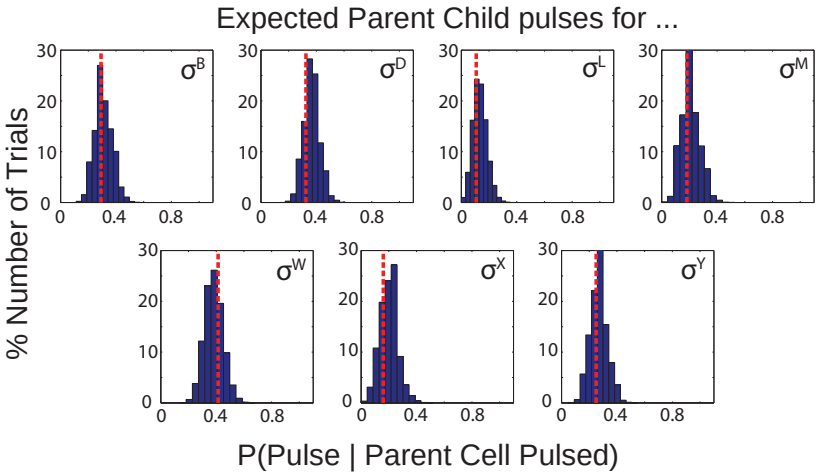


Figure B.3: **No correlations observed between a parent cell and its two daughters.** The frequency of events where a parent and subsequent child pulsed (red dashed line) was compared to a bootstrapped model (blue histogram) where parent/child pulses were randomized. The probability of pulses in generation n+1 is independent of the presence of pulses in generation n. Adapted from J.C.W.Locke and J.Park [Locke et al., 2014].

## B.3 Modelling sigma factor pulses

### B.3.1 Ultrasensitivity model

Figure B.4 (panel A) shows the peak height variation (defined as the dimensionless sigma factor concentration, $S$, maximum value minus the minimum value) as a function of the degradation rates of $A$ (the anti-sigma factor) and $S$ (considering $\delta_A = \delta_S = \delta$). Panel B of this figure displays the maximum logarithmic slope for 6 different curves $S_{eq}(\mu)$ corresponding to different values of $\delta$ (in Figure 3.10A, three of the $S_{eq}(\mu)$ curves considered here are plotted). Panel B allows us to define an ultrasensitivity region for a given set of parameters by defining a threshold value for $S_{eq}(\mu)$ slope (shadowed region).

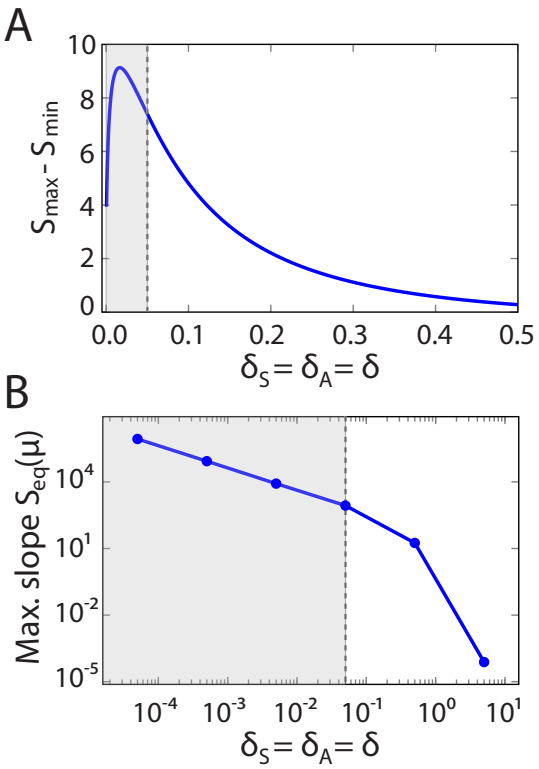


Figure B.4: **Characterization of the ultrasensitivity region.** (A) Peak height variation (defined as the maximum value of $S$ minus the minimum one) as a function of $\delta_S = \delta_A = \delta$. The parameter values used here are the same as in Figure 3.9 (except for the variation in $\delta_S$, $\delta_A$). (B) Maximum logarithmic slope for 6 different curves $S_{eq}(\mu)$ corresponding to 6 values of $\delta$ (including the ones plotted in Figure 3.10A). The parameter values used are the ones shown in Figure 3.10A plus $\delta = 5 \cdot 10^{-5}, 5 \cdot 10^{-4}, 5$. In both figures, shadowed regions correspond to the ultrasensitivity regime.

It is also worth to mention that in this system, under the ultrasensitivity regime, we can have bistability even though there is no cooperativity in $S$ and $A$ productions (see Figure B.5).

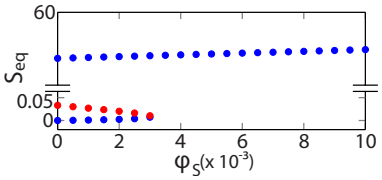


Figure B.5: **Bifurcation diagram for the ultrasensitivity model.** This diagram shows $S$ at the steady state ($S_{eq}$) versus $\varphi_S$. Blue dots indicate stable fixed points, whereas red dots represent unstable fixed points. Parameter values for this diagram are the following: $\varphi_A = 0.01$, $\rho = 0.7$, $\mu = 0.07$, $\chi = 0.8$, $\xi = 7$, $\delta_S = 0.005$, $\delta_A = 0.005$.

Figure B.6 shows the time series for $S(t)$ and the anti-sigma production rate, $\mu(t)$, for a simulation of the rescaled model for only one sigma factor. We considered $\mu(t) = \mu_0 e^{\epsilon(t)}/\langle e^{\epsilon(t)} \rangle$, where $\epsilon(t)$ is an Ornstein-Uhlenbeck (OU) process with autocorrelation time $\tau = 1000$ and an intensity of noise $D = 0.1$. The OU process was simulated using the algorithm from [Fox et al., 1988], and the ODEs were numerically integrated using the Heun algorithm for a colored noise [García-Ojalvo and Sancho, 1999].

As it can be seen in this figure, pulses in $S(t)$ are not a trivial reflection of the dynamics of $\mu(t)$. Of course, due to the nature of the ultrasensitivity mechanism, only when fluctuations surpass a certain threshold $S$ presents a pulse.

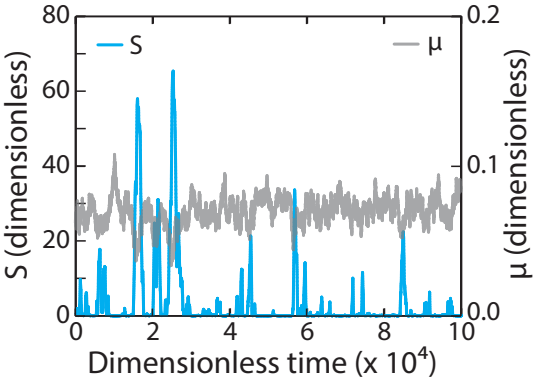


Figure B.6: **Comparing $S$ pulses with noise in the dimensionless ultrasensitivity model.** Time series for $S$ and *mu* are plotted for a simulation of only one sigma factor. Pulses in $S$ do not trivially follow the noise. Parameter values considered in this simulation are $\varphi_S = 0.003$, $\varphi_A = 0.001$, $\xi = 11$, $\rho = 0.7$, $\chi = 0.8$, $\delta_S = \delta_A = 0.005$, and $\mu(t) = \mu_0 e^{\epsilon(t)}/\langle e^{\epsilon(t)}\rangle$ where $\epsilon(t)$ is an Ornstein-Uhlenbeck (OU) process with autocorrelation time $\tau = 1000$ and intensity of noise $D = 0.1$. Where $\langle\mu(t)\rangle = \mu_0 = 0.07$.

Table B.4 contains the set of discrete reactions for the ultrasensitivity model. Time series for all species from a stochastic simulation considering only one sigma factor are shown in Figure B.7. Pulses in $C(t)$ follow those in $S(t)$ thanks to a high unbinding rate ($k_{r-}$). And pulses in $S$ are due to a tight binding with its cognate anti-sigma factor ($A$). Parameter values used for simulations shown in Figures 3.11 and B.7 are listed in Table B.5.

| | |
|---|---|
| **Basal productions** | **Activated productions** |
| $\varnothing \xrightarrow{\phi_s} S$ (a) | $C \xrightarrow{\beta_s} C + S$ (h) |
| $\varnothing \xrightarrow{\phi_a} A$ (b) | $C \xrightarrow{\beta_a(t)} C + A$ (i) |
| $\varnothing \xrightarrow{\alpha} R$ (c) | **Degradations/dilutions** |
| **Molecular titration** | $S \xrightarrow{\lambda_s} \varnothing$ (j) |
| $S + A \xrightarrow{k_{a+}} X$ (d) | $A \xrightarrow{\lambda_a} \varnothing$ (k) |
| $X \xrightarrow{k_{a-}} S + A$ (e) | $R \xrightarrow{\lambda_r} \varnothing$ (l) |
| **Holoenzyme formation** | $X \xrightarrow{\lambda_x} \varnothing$ (m) |
| $S + R \xrightarrow{k_{r+}} C$ (f) | $C \xrightarrow{\lambda_c} \varnothing$ (n) |
| $C \xrightarrow{k_{r-}} S + R$ (g) | |

Table B.4: **Set of reactions for the stochastic ultrasensitivity model.**

| Par. | Value | Units | Par. | Value | Units |
|---|---|---|---|---|---|
| $\phi_s$ | $2.47 \times 10^{-4}$ | $s^{-1}$ | $\beta_s$ | 0.05 | $s^{-1}$ |
| $\phi_a$ | $8.23 \times 10^{-5}$ | $s^{-1}$ | $\beta_a^0$ | 0.0495 | $s^{-1}$ |
| $\alpha$ | 40 | $s^{-1}$ | $\lambda_s$ | 0.005 | $s^{-1}$ |
| $k_{a+}$ | 0.0307 | $s^{-1}$ | $\lambda_a$ | 0.005 | $s^{-1}$ |
| $k_{a-}$ | 0.5 | $s^{-1}$ | $\lambda_r$ | 0.005 | $s^{-1}$ |
| $k_{r+}$ | 0.002 674 | $s^{-1}$ | $\lambda_x$ | 0.005 | $s^{-1}$ |
| $k_{r-}$ | 5.0 | $s^{-1}$ | $\lambda_c$ | 0.005 | $s^{-1}$ |

Table B.5: **Values of the reaction rates used in the stochastic simulations of the ultrasensitivity model.** $\beta_a(t) = \beta_a^0 e^{\epsilon(t)}/\langle e^{\epsilon(t)}\rangle$, where $\epsilon(t)$ is an Ornstein-Uhlenbeck (OU) process with autocorrelation time of the order of the cell cycle duration (this is, 2.5 h approximately) and intensity of noise $D = 100$.

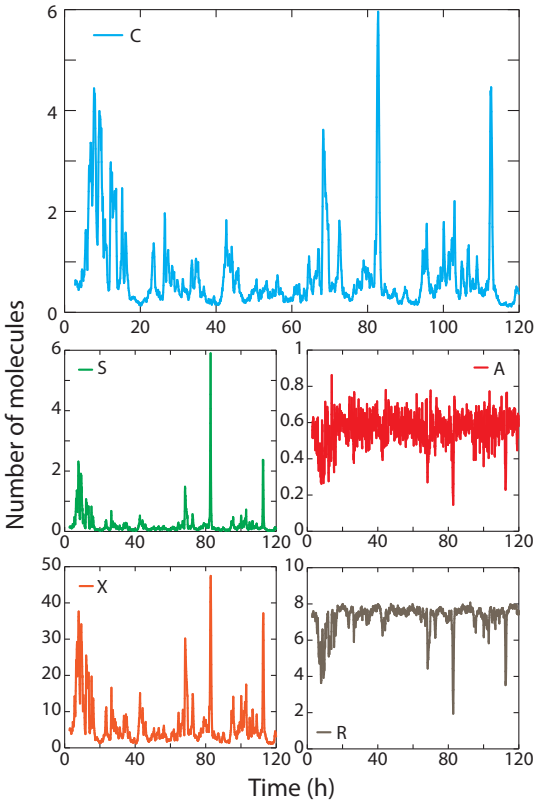


Figure B.7: **Time traces for all species from a stochastic simulation of the ultrasensitive model for only one sigma factor with noisy $\beta_a$.** The number of molecules for each species are plotted in function of time. See Table B.5 for the parameter values used in this simulation.

### B.3.2 Ligand model

| Par. | Value | Units | Par. | Value | Units |
|---|---|---|---|---|---|
| $k_1$ | 1 | $s^{-1}$ | $k_{12}$ | $3\times10^{-4}$ | $s^{-1}$ |
| $k_2$ | $2.468\times10^{-4}$ | $s^{-1}$ | $k_{13}$ | $3\times10^{-4}$ | $s^{-1}$ |
| $k_3$ | $1\times10^{-4}$ | $s^{-1}$ | $k_{14}$ | $3\times10^{-5}$ | $s^{-1}$ |
| $k_{l+}/\Omega$ | 0.3 | $s^{-1}$ | $k_{15}$ | $3\times10^{-4}$ | $s^{-1}$ |
| $k_{l-}$ | $5\times10^{-4}$ | $s^{-1}$ | $k_{16}$ | $3\times10^{-4}$ | $s^{-1}$ |
| $k_{a+}/\Omega$ | 0.4 | $s^{-1}$ | | | |
| $k_{a-}$ | 0.001 | $s^{-1}$ | $K_1$ | 0.001 | $s^{-1}$ |
| $k_{r+}/\Omega$ | 0.05 | $s^{-1}$ | $K_2$ | 0.01 | $s^{-1}$ |
| $k_{r-}$ | 5.0 | $s^{-1}$ | $K_3$ | 0.001 | $s^{-1}$ |
| $\beta_S$ | 0.001 | $s^{-1}$ | $K_4$ | 1.0 | $s^{-1}$ |
| $\beta_A$ | 0.0015 | $s^{-1}$ | $K_5$ | 0.001 | $s^{-1}$ |
| $k_{11}$ | $3\times10^{-4}$ | $s^{-1}$ | $K_6$ | $3\times10^{-5}$ | $s^{-1}$ |

Table B.6: **Values of the reaction rates used in the stochastic simulations of the ligand model.** Note that rates of bimolecular reactions are divided by the volume factor $\Omega$, that relates number of molecules in the stochastic description with concentrations in the deterministic one. In bacteria, $\Omega \approx 1$ molec $nM^{-1}$ [Süel et al., 2007].

| Par. | Value | Units | Par. | Value | Units |
|---|---|---|---|---|---|
| $k_1$ | 5 | $nM\ s^{-1}$ | $\beta_A$ | 0.0015 | $s^{-1}$ |
| $k_2$ | $2.468\times10^{-4}$ | $nM\ s^{-1}$ | $k_{11}$ | $3\times10^{-4}$ | $s^{-1}$ |
| $k_3$ | $1\times10^{-4}$ | $nM\ s^{-1}$ | $k_{12}$ | $3\times10^{-4}$ | $s^{-1}$ |
| $k_{l+}$ | 0.3 | $nM^{-1}\ s^{-1}$ | $k_{13}$ | $3\times10^{-4}$ | $s^{-1}$ |
| $k_{l-}$ | $5\times10^{-4}$ | $s^{-1}$ | $k_{14}$ | $3\times10^{-5}$ | $s^{-1}$ |
| $k_{a+}$ | 0.4 | $nM^{-1}\ s^{-1}$ | $k_{15}$ | $3\times10^{-4}$ | $s^{-1}$ |
| $k_{a-}$ | 0.001 | $s^{-1}$ | $k_{16}$ | $3\times10^{-4}$ | $s^{-1}$ |
| $k_{r+}$ | 0.5 | $nM^{-1}\ s^{-1}$ | $k_{17}$ | $3\times10^{-4}$ | $s^{-1}$ |
| $k_{r-}$ | $5\times10^{-4}$ | $s^{-1}$ | $L$ burst freq. | $3\times10^{-4}$ | $s^{-1}$ |
| $\beta_S$ | 0.001 | $s^{-1}$ | $L$ burst size | 10 | - |

Table B.7: **Values of the reaction rates used in the deterministic version of the ligand model simulations.** For these values of the parameters the mean duration of pulses is 1.2 h, and the mean frequency is 0.3 $h^{-1}$ (Figure 3.16). In order to perform the competition experiment *in silico* (Figure 3.18B) the following parameters were modified: $k_{r-}^{(1)}$ =0.005 $s^{-1}$, $k_{r-}^{(7)}$ =$5\times10^{-8}$ $s^{-1}$, $\beta_S^{(7)} \in [0.0003, 0.00035]$ $s^{-1}$, $k_3^{(7)} = k_{l+}^{(7)} = k_{l-}^{(7)} = k_{a+}^{(7)} = k_{a-}^{(7)} = k_{13}^{(7)} = k_{14}^{(7)} = k_{15}^{(7)} = k_{20}^{(7)} = 0$.

The sequence of a sigma factor activity pulse in the ligand model is illustrated in Figure B.8. A burst in ligand concentration (motivated by a gamma distributed Ornstein-Uhlenbeck process) causes sequestration of the anti-sigma factor by the formation of the inactive complex ligand–anti-sigma factor ($I$). This reduces the amount of free anti-sigma factor, which allows the dissociation of the inactive complex sigma–anti-sigma ($X$). This results in an increase of free sigma factor that rapidly recruits RNAP in order to form the holoenzyme sigma-RNAP ($C$) active complex. The activated transcription of the sigma factor and its cognate anti-sigma factor due to $C$ activity results in an increase of the complex sigma–anti-sigma, and eventually the pulse in $C$ is terminated as the activated production of the anti-sigma factor is slightly larger than the one of the sigma factor.

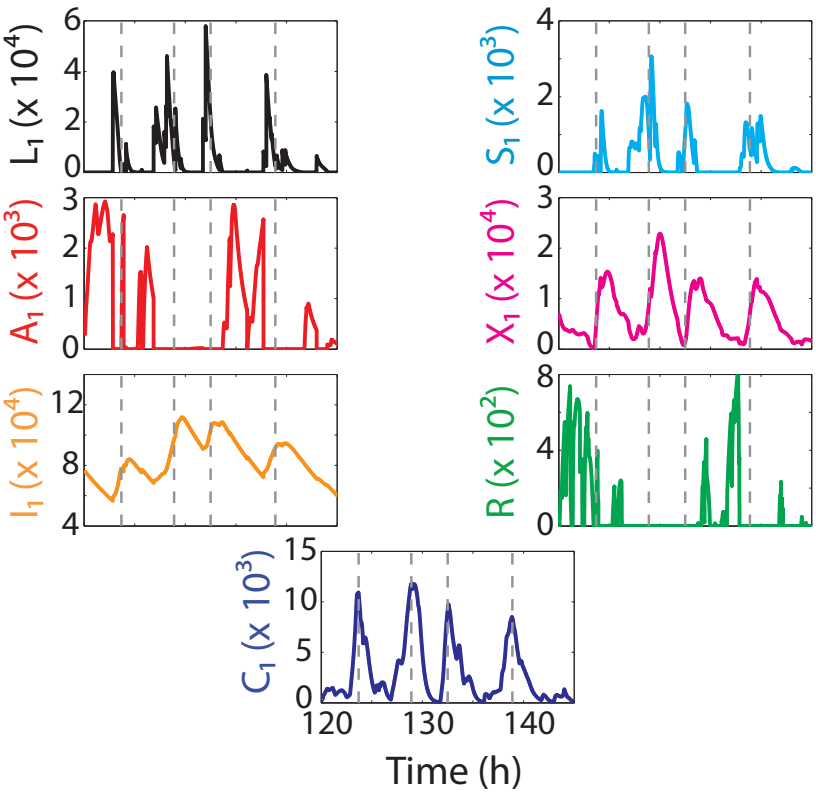


Figure B.8: **Time traces for all species for the ligand model.** Focusing on a few typical pulses in $C_1$, we plot here the behavior of the different species in the model. For the simulation shown in Figure 3.16, here we plot the time traces for the ligand ($L_1$), the free sigma factor ($S_1$), its cognate anti-sigma factor ($A_1$), the complex $S_1 - A_1$ ($X_1$), the complex $L_1 - A_1$ ($I_1$), the available RNAP ($R$) and the holoenzyme $S_1 - R$ ($C_1$), all for sigma factor 1. Gray dashed lines mark the time at which $C_1$ pulses occur. Note that for the parameter set considered RNAP is saturated. See Table B.7 for parameter values.

### B.3.3 Limit cycle model

| Par. | Value | Units | Par. | Value | Units |
|---|---|---|---|---|---|
| $k_2$ | $8.7 \times 10^{-5}$ | nM s$^{-1}$ | $k_t$ | 0.0077 | s$^{-1}$ |
| $k_3$ | $5 \times 10^{-5}$ | nM s$^{-1}$ | $k_m$ | $2.94 \times 10^{-4}$ | s$^{-1}$ |
| $k_{l+}$ | 0.2353 | nM$^{-1}$ s$^{-1}$ | $\beta_S$ | 0.0238 | s$^{-1}$ |
| $k_{a+}$ | 0.0203 | nM$^{-1}$ s$^{-1}$ | $\beta_A$ | 0.1590 | s$^{-1}$ |
| $k_{a-}$ | 0.0013 | s$^{-1}$ | $\delta$ | $1 \times 10^{-4}$ | s$^{-1}$ |
| $k_{r+}$ | $3.97 \times 10^{-6}$ | nM$^{-1}$ s$^{-1}$ | $\delta_m$ | 0.0015 | s$^{-1}$ |
| $k_{r-}$ | 0.0014 | s$^{-1}$ | $L_T$ | 534.1087 | nM |
| $k_{lx}$ | $1.2807 \times 10^{-4}$ | nM$^{-1}$ s$^{-1}$ | $R_T$ | 19.9223 | nM |

Table B.8: **Reaction rates values for the limit cycle simulations.**

## B.4 Predicted distribution of the number of sigma factors simultaneously active

In order to compute the predicted distribution of the number of sigma factors simultaneously active from experimentally determined pulse statistics shown in Figure 3.18, we considered the following. With $\sigma^i$ (where $i = 1, \ldots, 7$) denoting the 7 sigma factors studied experimentally, each of them with its own frequency ($f_i$) and duration ($\tau_i$), the probability that a given $\sigma^i$ is active at any instant is given by $p_i = f_i \tau_i$ assuming pulses are generated stochastically.

Assuming now that sigma factors pulses occur independently of each other, it is possible to have up to 7 sigma factors pulsing simultaneously. If we consider the probability that $\sigma^1$, and only $\sigma^1$, is pulsing at some point in time, this is given by $p_1 \prod_{j=2}^{7}(1 - p_j)$. Hence, summing this quantity over all sigma factors, we can find the probability that exactly one sigma is pulsing at some point in time, regardless of the sigma identity:

$$\sum_{i=1}^{7} \left( p_i \prod_{\substack{j=1 \\ j \neq i}}^{7} (1 - p_j) \right) \tag{B.1}$$

This expression is the one used to calculate the distribution shown in Figure 3.18B.

# C
# *Materials and Methods for Chapter 4*

In this Appendix we have included a compilation of supporting information for the work exposed in Chapter 4.

## *C.1 Plasmid and strain construction*

E. coli strain DH5$\alpha$ was used to clone all plasmids using standard molecular cloning techniques. Plasmid pMiL001 was constructed *de novo* by assembling the origin of replication SC101 and the gene for spectinomycin resistance. Plasmid pMiL101 was constructed cloning the construct $P_{lac/ara}$-*hda*-*dnaN*-*T1* into pMiL001 (*T1* being the transcriptional terminator used in the synthetic oscillator) (see Figure C.1). $P_{lac/ara}$ and *T1* fragments were amplified by PCR from the original synthetic oscillator strain (JS011). In turn, *hda* and *dnaN* genes were amplified from the wild-type *E. coli* MG1655 genome. Both plasmids were verified by sequencing.

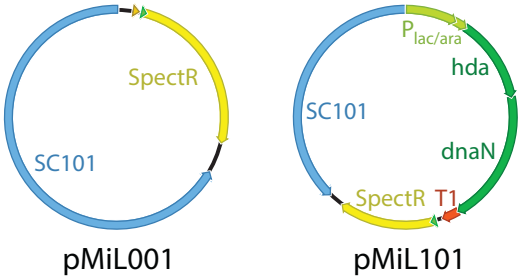


Figure C.1: **Plasmids diagrams.** Plasmid pMiL001 contains only the origin of replication (SC101) and the antibiotic resistance gene (spectinomycin). It was transformed into the synthetic oscillator "wild-type" strain (JS011) to conform the unidirectional strain. Plasmid pMiL101 contains the origin of replication (SC101), the antibiotic resistance gene (spectinomycin), and the construct $P_{lac/ara}$-*hda*-*dnaN*-*T1* (responsible for back-coupling the synthetic oscillator to chromosomal replication). pMiL101 was transformed into JS011 to form the bidirectional strain.

The unidirectional strain was constructed transforming the plasmid pMiL001 into the original synthetic oscillator strain JS011 (kind gift from Prof. J. Hasty, University of California San Diego). The bidirectional strain was constructed transforming the plasmid pMiL101 into JS011.

## *C.2 Growth conditions for microscopy*

Cells were grown overnight from glycerol stocks at 37°C in Luria Broth (Miller's modification) (LB) with appropriate antibiotics for selection (added to the following final concentrations: 100 $\mu$g/ml ampicilin, 50 $\mu$g/ml kanamycin, and 50 $\mu$g/ml spectinomycin), then diluted back

in LB with the corresponding antibiotics and inductors: 0.7% (w/v) arabinose and 2 mM IPTG, to a final $OD_{600} = 0.02$. This culture was grown at 37°C until $OD_{600} = 0.2$. After this, cells were diluted 1:5 in A minimal medium[1] with inductors and 0.4% (w/v) glucose. 50 $\mu$l of this diluted culture were spotted onto a low-melt agarose pad made of A minimal medium 2% (w/v) and containing the inductors and 0.4% (w/v) glucose. Cells were grown in the pad at 37°C for 2 h and then were vortexed in 10 ml of A minimal medium. 2.25 $\mu$l of the resulting "supernatant" were spotted onto a freshly prepared A minimal medium 2% (w/v) low melt agarose pad containing the inductors and 0.4% (w/v) glucose that was placed afterwards into a coverslip-bottom Willco dish for imaging.

[1] Composition of the A minimal medium per 100 ml: 20 ml A Salts (5x), 80 ml sterile deionized water, 100 $\mu$l $MgSO_4 \cdot 7\,H_2O$ (1 M), 250 $\mu$l Glycerol (80%), and 1 ml CasaAa (10%).

A Salts (5x) composition per 100 ml: 0.046 g $(NH_4)_2SO_4$, 2.25 g $KH_2PO_4$, 5.25 g $K_2HPO_4$, 0.25 g sodium citrate tribasic $\cdot\, 2\,H_2O$, and 100 ml sterile deionized water ([Sambrook et al., 1989]).

All data were acquired imaging *E. coli* microcolonies in the pads at 37°C with a Nikon TE2000 inverted microscope and a motorized stage (Prior). Images were acquired every 5 min with a Hamamatsu ORCA-ER camera. Imaging time was optimized to prevent phototoxicity [Süel et al., 2006] and photobleaching [Herman et al., 2014]. Between days, relative lamp intensity levels were monitored by taking an image of fluorescent beads and measuring their mean intensity. Exposure times were then adjusted to keep emission light levels constant between experiments. The NIS-Elements software was used to automate image acquisition and microscope control. Data analysis of time-lapse movies was performed by custom software developed with MATLAB using the image processing and statistics toolboxes (MathWorks).

## C.3 Modelling the synthetic oscillator

Stricker *et al.* proposed a detailed molecular model for their synthetic oscillator consisting in 73 reactions, 27 species and 27 parameters. The authors explicitly considered intermediate processes such as dimerization of AraC and tetramerization of LacI [Stricker et al., 2008]. Due to the difficulty to work with such a complex model, we propose a low-dimensional model based on minimal mechanisms, inspired by the model from Rué and Garcia-Ojalvo [2011],

$$\frac{dA}{dt} = \alpha_1 + \frac{\beta_1 A^n}{K^n + A^n + (\gamma R)^p} - \delta_1 A \tag{C.1a}$$

$$\frac{dR}{dt} = \alpha_2 + \frac{\beta_2 A^n}{K^n + A^n + (\gamma R)^p} - \delta_2 R \tag{C.1b}$$

where $A$ is the activator (AraC dimers) and $R$ the repressor (LacI tetramers). Given that all the synthetic oscillator elements are controlled by the same promoter ($P_{lac/ara}$) $K$, $n$, $p$ and $\gamma$ are the same for both species. A cartoon showing model interactions is shown in Figure C.2. These ODEs are part of the coupled oscillator model (see Eq.(4.1)a-b).

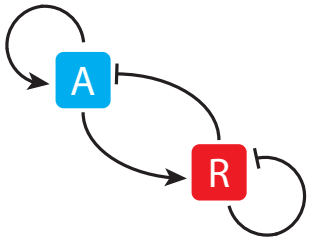


Figure C.2: **Diagram of interactions for the synthetic oscillator reduced model.** The activator ($A$) promotes its own production and the repressor ($R$) one. Whereas the repressor inhibits $A$ expression and its own.

This system presents a limit cycle for the parameter values shown in

Table C.1. Note that we assume a non zero basal production because the limit cycle disappears when $\alpha_1 = 0$. In this regard, experiments show that when the synthetic oscillator is not induced part of the population turns on the reporter's expression, thus demonstrating that that the hybrid promoter $P_{lac/ara}$ is leaky.

Degradation rate of $R$ ($\delta_2$) is one order of magnitude smaller than the one of $A$ ($\delta_1$) which can be explained by the following reason. AraC and LacI are marked with a *ssrA* degradation tag. This tag is recognized by ClpXP, a proteolytic machine composed by ClpX (responsible for unfolding the protein to be degraded) and ClpP (a peptidase) [Baker and Sauer, 2012]. This tag is also recognized by ClpAP, that analogously to ClpPX is composed by a chaperon (ClpA) and also by the ClpP peptidase [Sharma et al., 2005]. When ClpAP finds an homodimer (which happens when the two protomers -the subunits that constitute an oligomeric protein- have the *ssrA* degradation tag, as it is our case) the most probable scenario is that ClpAP degrades the two subunits at the same time [Sharma et al., 2005]. It is also probable that ClpXP behaves in the same way. However, there is no evidence in the literature that ClpAP and/or ClpXP may degrade a whole tetrameric complex at once. Studies measuring the size of the pore that allows the substrate to reach the active site of ClpP show that this pore would be big enough to simultaneously accommodate between two and three polypeptidic chains [Burton et al., 2013]. In addition, kinetic experiments with ClpXP machinery indicate that the denaturalization process determines the degradation rate [Kim et al., 2000]. Hence, it seems reasonable that LacI tetramers ($R$) degrade slower than AraC dimers ($A$) [2].

The Hill coefficients in the synthetic oscillator model, defined by parameters $n$ and $p$ are both equal to 2 and account for changes in DNA conformation. Regarding $n$, regulation of $P_{ara}$ by AraC is implemented in a positive form (in the presence of arabinose) and in a negative one (in the absence of arabinose) involving DNA looping [Lobell and Schleif, 1990]. Regarding $p$, the repression of $P_{lac}$ also relies in a DNA looping conformation effect [Lewis et al., 1996].

[2] Consider a pool of a protein that assembles in "homo-tetramers". If we denote by $D$ the dimeric conformation and by $T$ the tetrameric form, assuming degradation only occurs enzimatically we have:

$$\frac{dD}{dt} = -k_+ D^2 + \delta_T CT - \delta_D CD$$
$$\frac{dT}{dt} = k_+ D^2 - \delta_T CT$$

where $C$ corresponds to the protease concentration. If we assume that $D$ is in quasi-steady state, we obtain

$$\frac{dT}{dt} = \frac{(\delta_D C)^2}{2k_+} - \frac{\delta_D C}{2k_+}\sqrt{(\delta_D C)^2 + 4k_+\delta_T CT}$$

Given the assumption in $k_+$, from the previous expression we have that $T$ degrades as $\sim T^{1/2}$. Since in the model Eq.(C.1) we consider only linear degradations, we take this fact into account by assuming a smaller degradation rate for $R$ (LacI tetramers) compared to $A$ degradation rate (AraC dimers).

| Par. | Value | Units | Description |
|---|---|---|---|
| $\alpha_1$ | 5.1 | nM $s^{-1}$ | A basal production rate |
| $\alpha_2$ | 0.75 | nM $s^{-1}$ | R basal production rate |
| $\alpha_3$ | 0.5 | nM $s^{-1}$ | B basal production rate |
| $\beta_1$ | 225 | nM $s^{-1}$ | A maximum activated production rate |
| $\beta_2$ | 30 | nM $s^{-1}$ | R maximum activated production rate |
| $\beta_3$ | 10 | nM $s^{-1}$ | B maximum activated production rate |
| $\delta_1$ | 0.011 58 | $s^{-1}$ | A degradation rate |
| $\delta_2$ | 0.001 158 | $s^{-1}$ | R degradation rate |
| $\delta_3$ | 0.000 25 | $s^{-1}$ | B degradation rate |
| $\gamma$ | 2 | - | Ratio of activation to inhibition threshold |
| $K$ | 5000 | nM | Concentration of A for half-maximal activation |
| $n$ | 2 | - | Activation cooperativity |
| $p$ | 2 | - | Inhibition cooperativity |
| $L_0$ | 0.5 | a.u. | Initial cell length (when cell is born) |
| $\tau$ | 30 | min | Characteristic time of the cell growth integrate & fire model |
| $K_I$ | 100 | nM | Concentration of B for half-maximal back-coupling |
| $\epsilon$ | 0.75 | - | Replication threshold |

Table C.1: **Parameter values for the coupled oscillator model.**

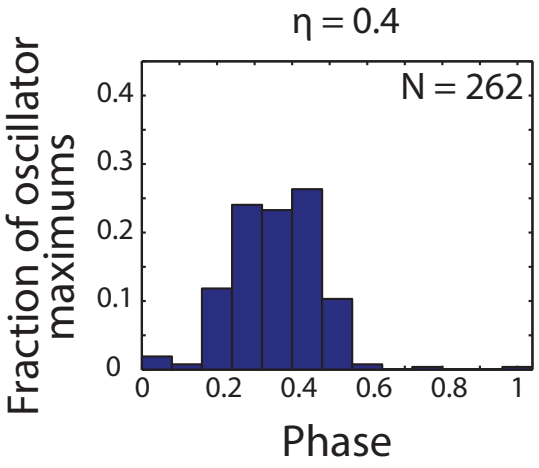


Figure C.3: **Phase shift between the two simulated oscillators for $\eta = 0.4$.** Histogram of the timing of activator concentration maximums within a cell length cycle computed for $\eta = 0.4$. This figure shows an intermediate intensity back-coupling case ($\eta = 0.4$) thus completing the results shown in Figure 4.10.

# *List of publications*

- L. Espinar, M. Dies, T. Çagatay, G. M. Süel, and J. Garcia-Ojalvo. Circuit-level input integration in bacterial gene regulation. *Proceedings of the National Academy of Sciences*, 110(17):7091–7096, 2013
- J. C. Locke, J. Park, M. Dies, S. E. Smith-Unna, S. Quinodoz, M. J. Hernández-Jiménez, J. Garcia-Ojalvo, and M. B. Elowitz. Molecular time-sharing through dynamic pulsing in single cells. *Science*, Under review, 2014
- M. Dies, L. Galera, and J. Garcia-Ojalvo. Mutual regulation causes co-entrainment of coupled cellular rhythms. *Integrative Biology*, To be submitted

# *Bibliography*


B. Alberts, A. Johnson, J. Lewis, M. Raff, K. Roberts, and P. Walter. *Molecular biology of the cell*. Garland Science, 2002.

M. Amdaoud, M. Vallade, C. Weiss-Schaber, and I. Mihalcescu. Cyanobacterial clock, a stable phase oscillator with negligible intercellular coupling. *Proceedings of the National Academy of Sciences*, 104(17):7051–7056, 2007.

S. Artavanis-Tsakonas, M. D. Rand, and R. J. Lake. Notch signaling: cell fate control and signal integration in development. *Science*, 284(5415):770–776, 1999.

K. Asai, T. Ootsuji, K. Obata, T. Matsumoto, Y. Fujita, and Y. Sadaie. Regulatory role of RsgI in sigI expression in Bacillus subtilis. *Microbiology*, 153(1):92, 2007.

L. Ashall, C. A. Horton, D. E. Nelson, P. Paszek, C. V. Harper, K. Sillitoe, S. Ryan, D. G. Spiller, J. F. Unitt, D. S. Broomhead, et al. Pulsatile stimulation determines timing and specificity of NF-κB-dependent transcription. *Science*, 324(5924):242–246, 2009.

T. A. Baker and R. T. Sauer. ClpXP, an ATP-powered unfolding and protein-degradation machine. *Biochimica et Biophysica Acta (BBA) - Molecular Cell Research*, 1823(1):15–28, Jan. 2012.

P. Balbás, X. Soberón, E. Merino, M. Zurita, H. Lomeli, F. Valle, N. Flores, and F. Bolivar. Plasmid vector pBR322 and its special-purpose derivatives — a review. *Gene*, 50(1):3–40, 1986.

E. Batchelor, A. Loewer, C. Mock, and G. Lahav. Stimulus-dependent dynamics of p53 in single cells. *Molecular systems biology*, 7(1), 2011.

S. A. Boylan, A. R. Redfield, M. S. Brody, and C. W. Price. Stress-induced activation of the sigma B transcription factor of Bacillus subtilis. *Journal of bacteriology*, 175(24):7931–7937, 1993.

N. E. Buchler and M. Louis. Molecular titration and ultrasensitivity in regulatory networks. *Journal of molecular biology*, 384(5):1106–1119, 2008.

R. E. Burton, S. M. Siddiqui, Y. I. Kim, T. A. Backer, and R. T. Sauer. Effects of protein stability and structure on substrate processing by the ClpXP unfolding and degradation machine. pages 1–9, Oct. 2013.

T. Çagatay, M. Turcotte, M. B. Elowitz, J. Garcia-Ojalvo, and G. M. Süel. Architecture-dependent noise discriminates functionally analogous differentiation circuits.

L. Cai, N. Friedman, and X. S. Xie. Stochastic protein expression in individual cells at the single molecule level. *Nature*, 440(7082):358–362, 2006.

L. Cai, C. Dalal, and M. Elowitz. Frequency-modulated nuclear localization bursts coordinate gene regulation. *Nature*, 455(7212):485–490, 2008.

J. E. Camara, A. M. Breier, T. Brendler, S. Austin, N. R. Cozzarelli, and E. Crooke. Hda inactivation of DnaA is the predominant mechanism preventing hyperinitiation of Escherichia coli DNA replication. *EMBO reports*, 6(8):736–741, 2005.

M. Cao, T. Wang, R. Ye, and J. D. Helmann. Antibiotics that inhibit cell wall biosynthesis induce expression of the Bacillus subtilis $\sigma^W$ and $\sigma^M$ regulons. *Molecular microbiology*, 45(5):1267–1276, 2002.

M. Cao, L. Salzberg, C. Tsai, T. Mascher, C. Bonilla, T. Wang, R. Ye, L. Marquez-Magana, and J. Helmann. Regulation of the Bacillus subtilis extracytoplasmic function protein {sigma} Y and its target promoters. *Journal of bacteriology*, 185(16):4883, 2003. ISSN 0021-9193.

M. Chalfie, Y. Tu, G. Euskirchen, W. W. Ward, and D. C. Prasher. Green fluorescent protein as a marker for gene expression. *Science*, 263(5148):802–805, 1994.

L. Chevroton and F. Vles. La cinématique de la segmentation de l'oeuf et la chronophotographie du développement de l'oursin. *Comptes rendus hebdomadaires des séances de l'Académie des Sciences*, 149:806–809, 1909.

S.-K. Choi and M. H. Saier. Regulation of sigL expression by the catabolite control protein CcpA involves a roadblock mechanism in Bacillus subtilis: potential connection between carbon and nitrogen metabolism. *Journal of bacteriology*, 187(19):6856–6861, 2005.

H. A. Choy, J. M. Romeo, and E. P. Geiduschek. Activity of a phage-modified RNA polymerase at hybrid promoters: Effects of substituting thymine for hydroxymethyluracil in a phage SP01 middle promoter. *Journal of molecular biology*, 191(1):59–73, 1986.

W. Chu. A study of asynchronous time division multiplexing for time-sharing computer systems. In *Proceedings of the November 18-20, 1969, fall joint computer conference*, pages 669–678. ACM, 1969.

D. F. Conrad, D. Pinto, R. Redon, L. Feuk, O. Gokcumen, Y. Zhang, J. Aerts, T. D. Andrews, C. Barnes, P. Campbell, et al. Origins and functional impact of copy number variation in the human genome. *Nature*, 464(7289):704–712, 2010.

M. Costanzo and J. Pero. Structure of a Bacillus subtilis bacteriophage SPO1 gene encoding RNA polymerase sigma factor. *Proceedings of the National Academy of Sciences*, 80(5):1236–1240, 1983.

J. Cotterell and J. Sharpe. An atlas of gene regulatory networks reveals multiple three-gene mechanisms for interpreting morphogen gradients. *Molecular systems biology*, 6(1), 2010.

D. L. Coutu and T. Schroeder. Probing cellular processes by long-term live imaging–historic problems and current solutions. *Journal of cell science*, 126(17):3805–3815, 2013.

M. W. Covert, T. H. Leung, J. E. Gaston, and D. Baltimore. Achieving stability of lipopolysaccharide-induced NF-$\kappa$B activation. *Science*, 309(5742):1854–1857, 2005.

C. J. Davidson, A. Narang, and M. G. Surette. Integration of transcriptional inputs at promoters of the arabinose catabolic pathway. *BMC systems biology*, 4(1):75, 2010.

M. Debarbouille, R. Gardan, M. Arnaud, and G. Rapoport. Role of BkdR, a transcriptional activator of the SigL-dependent isoleucine and valine degradation pathway in Bacillus subtilis. *Journal of bacteriology*, 181(7): 2059–2066, 1999.

M. Decina and C. Rossi. Time division multiplexing. In *In Fondazione Ugo Bordoni Numerical Transmission by Cable, Vol. 1 p 279-386 (SEE N81-27351 18-32)*, volume 1, pages 279–386, 1980.

A. DeLuna, K. Vetsigian, N. Shoresh, M. Hegreness, M. Colón-González, S. Chao, and R. Kishony. Exposing the fitness contribution of duplicated genes. *Nature genetics*, 40(5):676–681, 2008.

M. Dies, L. Galera, and J. Garcia-Ojalvo. Mutual regulation causes co-entrainment of coupled cellular rhythms. *Integrative Biology*, To be submitted.

W. D. Donachie and G. W. Blakely. Coupling the initiation of chromosome replication to cell size in Escherichia coli. *Current opinion in microbiology*, 6(2):146–150, 2003.

D. Dubnau and R. Losick. Bistability in bacteria. *Molecular microbiology*, 61(3):564–572, 2006.

A. Eldar, V. K. Chary, P. Xenopoulos, M. E. Fontes, O. C. Losón, J. Dworkin, P. J. Piggot, and M. B. Elowitz. Partial penetrance facilitates developmental evolution in bacteria. *Nature*, 460(7254):510–514, 2009.

M. B. Elowitz, A. J. Levine, E. D. Siggia, and P. S. Swain. Stochastic gene expression in a single cell. *Science*, 297 (5584):1183–1186, 2002.

B. Ermentrout and A. Mahajan. Simulating, analyzing, and animating dynamical systems: a guide to XPPAUT for researchers and students. *Appl Mech Rev*, 5:B53, 2003.

L. Espinar, M. Dies, T. Çagatay, G. M. Süel, and J. Garcia-Ojalvo. Circuit-level input integration in bacterial gene regulation. *Proceedings of the National Academy of Sciences*, 110(17):7091–7096, 2013.

W. Estacio, S. Santa Anna-Arriola, M. Adedipe, and L. Márquez-Magaña. Dual promoters are responsible for transcription initiation of the fla/che operon in Bacillus subtilis. *Journal of bacteriology*, 180(14):3548–3555, 1998.

R. F. Fox, I. R. Gatland, R. Roy, and G. Vemuri. Fast, accurate algorithm for numerical simulation of exponentially correlated colored noise. *Physical review A*, 38(11):5938, 1988.

N. Friedman, L. Cai, and X. S. Xie. Linking stochastic dynamics to population distribution: an analytical framework of gene expression. *Physical review letters*, 97(16):168302, 2006.

H. G. Garcia and R. Phillips. Quantitative dissection of the simple repression input–output function. *Proceedings of the National Academy of Sciences*, 108(29):12173–12178, 2011.

H. G. Garcia, H. J. Lee, J. Q. Boedicker, and R. Phillips. Comparison and calibration of different reporters for quantitative analysis of gene expression. *Biophysical journal*, 101(3):535–544, 2011.

J. García-Ojalvo and J. M. Sancho. Fundamentals and tools. In *Noise in Spatially Extended Systems*, pages 53–113. Springer, 1999.

N. Geva-Zatorsky, N. Rosenfeld, S. Itzkovitz, R. Milo, A. Sigal, E. Dekel, T. Yarnitzky, Y. Liron, P. Polak, G. Lahav, et al. Oscillations and variability in the p53 system. *Molecular systems biology*, 2(1), 2006.

D. T. Gillespie. Exact stochastic simulation of coupled chemical reactions. *The journal of physical chemistry*, 81(25): 2340–2361, 1977.

A. Goldbeter. Computational approaches to cellular rhythms. *Nature*, 420(6912):238–245, 2002.

I. L. Grigorova, N. J. Phleger, V. K. Mutalik, and C. A. Gross. Insights into transcriptional regulation and $\sigma$ competition from an equilibrium model of RNA polymerase binding to DNA. *Proceedings of the National Academy of Sciences*, 103(14):5332–5337, 2006.

G. Grompone, M. Seigneur, S. D. Ehrlich, and B. Michel. Replication fork reversal in DNA polymerase III mutants of Escherichia coli: a role for the $\beta$ clamp. *Molecular microbiology*, 44(5):1331–1339, 2002.

A. D. Grossman. Genetic networks controlling the initiation of sporulation and the development of genetic competence in Bacillus subtilis. *Annual review of genetics*, 29(1):477–508, 1995.

J. D. Gruber, K. Vogel, G. Kalay, and P. J. Wittkopp. Contrasting properties of gene-specific regulatory, coding, and copy number mutations in Saccharomyces cerevisiae: frequency, effects, and dominance. *PLoS genetics*, 8 (2):e1002497, 2012.

T. M. Gruber and C. A. Gross. Multiple sigma subunits and the partitioning of bacterial transcription space. *Annual Reviews in Microbiology*, 57(1):441–466, 2003.

P. Haima, S. Bron, and G. Venema. The effect of restriction on shotgun cloning and plasmid stability in Bacillus subtilis Marburg. *Molecular and General Genetics MGG*, 209(2):335–342, 1987.

M. Hecker, J. Pané-Farré, and U. Völker. SigB-dependent general stress response in Bacillus subtilis and related gram-positive bacteria. *Microbiology*, 61(1):215, 2007.

J. Helmann. The extracytoplasmic function (ECF) sigma factors. *Advances in microbial physiology*, 46:47–110, 2002. ISSN 0065-2911.

J. D. Helmann and M. Chamberlin. Structure and function of bacterial sigma factors. *Annual review of biochemistry*, 57(1):839–872, 1988.

B. Herman, M. Parry-Hill, I. Johnson, and M. Davidson. Photobleaching. Optical Microscopy Division of the National High Magnetic Field Laboratory, March 2014. http://micro.magnet.fsu.edu/primer/java/fluorescence/photobleaching/.

K. A. Hicks and A. D. Grossman. Altering the level and regulation of the major sigma subunit of RNA polymerase affects gene expression and development in Bacillus subtilis. *Molecular microbiology*, 20(1):201–212, 1996.

M. J. Horsburgh and A. Moir. $\sigma^M$, an ECF RNA polymerase sigma factor of Bacillus subtilis 168, is essential for growth and survival in high concentrations of salt. *Molecular microbiology*, 32(1):41–50, 1999.

X. Huang, A. Decatur, A. Sorokin, and J. D. Helmann. The Bacillus subtilis $\sigma^X$ protein is an extracytoplasmic function sigma factor contributing to survival at high temperature. *Journal of bacteriology*, 179(9):2915–2921, 1997.

K. T. Hughes and K. Mathee. The anti-sigma factors. *Annual Reviews in Microbiology*, 52(1):231–286, 1998.

A. Hunziker, C. Tuboly, P. Horváth, S. Krishna, and S. Semsey. Genetic flexibility of regulatory networks. *Proceedings of the National Academy of Sciences*, 107(29):12998–13003, 2010.

K. Kaasik and C. C. Lee. Reciprocal regulation of haem biosynthesis and the circadian clock in mammals. *Nature*, 430(6998):467–471, 2004.

J. M. Kaguni. DnaA: controlling the initiation of bacterial DNA replication and more. *Annu. Rev. Microbiol.*, 60: 351–371, 2006.

S. Kalman, M. Duncan, S. M. Thomas, and C. W. Price. Similar organization of the sigB and spoIIA operons encoding alternate sigma factors of Bacillus subtilis RNA polymerase. *Journal of bacteriology*, 172(10):5575–5585, 1990.

T. Kalmar, C. Lim, P. Hayward, S. Muñoz-Descalzo, J. Nichols, J. Garcia-Ojalvo, and A. Arias. Regulated fluctuations in Nanog expression mediate cell fate decisions in embryonic stem cells. *PLoS biology*, 7(7):e1000149, 2009.

S. Kaplan, A. Bren, A. Zaslaver, E. Dekel, and U. Alon. Diverse two-dimensional input functions control bacterial sugar genes. *Molecular cell*, 29(6):786–792, 2008.

T. Katayama, S. Ozaki, K. Keyamura, and K. Fujimitsu. Regulation of the replication cycle: conserved and diverse regulatory systems for DnaA and oriC. *Nature Reviews Microbiology*, 8(3):163–170, 2010.

Y.-I. Kim, R. E. Burton, B. M. Burton, R. T. Sauer, and T. A. Baker. Dynamics of substrate denaturation and translocation by the ClpXP degradation machine. *Molecular cell*, 5(4):639–648, 2000.

S. Krishna, L. Orosz, K. Sneppen, S. Adhya, and S. Semsey. Relation of intracellular signal levels and promoter activities in the *gal* regulon of Escherichia coli. *Journal of molecular biology*, 391(4):671–678, 2009.

L. Kroos and Y. Yu. Regulation of $\sigma$ factor activity during Bacillus subtilis development. *Current Opinion in Microbiology*, 3(6):553–560, 2000. ISSN 1369-5274.

A. Kuchina, L. Espinar, T. Çagatay, A. O. Balbin, F. Zhang, A. Alvarado, J. Garcia-Ojalvo, and G. M. Süel. Temporal competition between differentiation programs determines cell fate choice.

G. Lahav. The strength of indecisiveness: oscillatory behavior for better cell fate determination. *Science Signaling*, 2004(264):pe55–pe55, 2004.

H. Landecker. Seeing things: from microcinematography to live cell imaging. *Nature methods*, 6(10):707–709, 2009.

G. Lee and J. Pero. Conserved nucleotide sequences in temporally controlled bacteriophage promoters. *Journal of molecular biology*, 152(2):247–265, 1981.

J. Lewis. Autoinhibition with transcriptional delay: a simple mechanism for the zebrafish somitogenesis oscillator. *Current Biology*, 13(16):1398–1408, 2003.

M. Lewis, G. Chang, N. C. Horton, M. A. Kercher, H. C. Pace, M. A. Schumacher, R. G. Brennan, and P. Lu. Crystal structure of the lactose operon repressor and its complexes with DNA and inducer. *Science*, 271(5253): 1247–1254, 1996.

J. Lippincott-Schwartz, E. Snapp, and A. Kenworthy. Studying protein dynamics in living cells. *Nature Reviews Molecular Cell Biology*, 2(6):444–456, 2001.

R. B. Lobell and R. F. Schleif. DNA looping and unlooping by AraC protein. *Science*, 250(4980):528–532, 1990.

J. C. Locke, J. W. Young, M. Fontes, M. J. H. Jiménez, and M. B. Elowitz. Stochastic pulse regulation in bacterial stress response. *Science*, 334(6054):366–369, 2011.

J. C. Locke, J. Park, M. Dies, S. E. Smith-Unna, S. Quinodoz, M. J. Hernández-Jiménez, J. Garcia-Ojalvo, and M. B. Elowitz. Molecular time-sharing through dynamic pulsing in single cells. *Science*, Under review, 2014.

R. Losick and J. Pero. Cascades of Sigma factors. *Cell*, 25(3):582, 1981.

Y. Luo, K. Asai, Y. Sadaie, and J. Helmann. Transcriptomic and phenotypic characterization of a Bacillus subtilis strain without extracytoplasmic function $\sigma$ factors. *Journal of Bacteriology*, 2010. ISSN 0021-9193.

H. Maamar and D. Dubnau. Bistability in the Bacillus subtilis K-state (competence) system requires a positive feedback loop. *Molecular microbiology*, 56(3):615–624, 2005.

M. Maciag, D. Nowicki, L. Janniere, A. Szalewska-Palasz, and G. Wegrzyn. Genetic response to metabolic fluctuations: correlation between central carbon metabolism and DNA replication in Escherichia coli. *Microb Cell Fact*, 10:19, 2011.

S. MacLellan, J. Helmann, and H. Antelmann. The YvrI alternative $\sigma$ factor is essential for acid stress induction of oxalate decarboxylase in Bacillus subtilis. *Journal of bacteriology*, 191(3):931, 2009. ISSN 0021-9193.

H. Maeda, N. Fujita, and A. Ishihama. Competition among seven Escherichia coli $\sigma$ subunits: relative binding affinities to the core RNA polymerase. *Nucleic acids research*, 28(18):3497–3503, 2000.

T. Matsumoto, K. Nakanishi, K. Asai, and Y. Sadaie. Transcriptional analysis of the ylaABCD operon of Bacillus subtilis encoding a sigma factor of extracytoplasmic function family. *Genes & genetic systems*, 80(6):385–393, 2005. ISSN 1341-7568.

M. V. Matz, K. A. Lukyanov, and S. A. Lukyanov. Family of the green fluorescent protein: journey to the end of the rainbow. *Bioessays*, 24(10):953–959, 2002.

J.-B. Michel, P. J. Yeh, R. Chait, R. C. Moellering, and R. Kishony. Drug interactions modulate the potential for evolution of resistance. *Proceedings of the National Academy of Sciences*, 105(39):14918–14923, 2008.

R. Middleton and A. Hofmeister. New shuttle vectors for ectopic insertion of genes into Bacillus subtilis. *Plasmid*, 51(3):238–245, 2004.

I. Mihalcescu, W. Hsing, and S. Leibler. Resilient circadian oscillator revealed in individual cyanobacteria. *Nature*, 430(6995):81–85, 2004.

L. Mitchell. The man who stopped time. Stanford Alumni Magazine, May/June 2001. http://alumni.stanford.edu/get/page/magazine/article/?article_id=39117.

N. A. M. Monk. Oscillatory Expression of Hes1, p53, and NF-κB Driven by Transcriptional Time Delays. *Current Biology*, 13(16):1409–1413, Aug. 2003.

E. Muybridge. *Animals in motion*. Courier Corporation, 1957.

W. Ockenga. Phase contrast, June 2011. http://www.leica-microsystems.com/science-lab/phase-contrast/.

M. Paget and J. Helmann. The $\sigma^{70}$ family of sigma factors. *Genome Biol*, 4(203):2003–4, 2003.

A. Pikovsky, M. Rosenblum, and J. Kurths. *Synchronization: a universal concept in nonlinear sciences*, volume 12. Cambridge university press, 2003.

A. Pizon. Une nouvelle application de la chronophotographie: la biotachygraphie. *Compte-rendu des séances du sixième congrès international du zoologie, tenu à Berne du 14 au 16 aout*, pages 404–9, 1905.

D. C. Prasher, V. K. Eckenrode, W. W. Ward, F. G. Prendergast, and M. J. Cormier. Primary structure of the aequorea victoria green-fluorescent protein. *Gene*, 111(2):229–233, 1992.

J. E. Purvis, K. W. Karhohs, C. Mock, E. Batchelor, A. Loewer, and G. Lahav. p53 dynamics control cell fate. *Science*, 336(6087):1440–1444, 2012.

A. Raj, C. S. Peskin, D. Tranchina, D. Y. Vargas, and S. Tyagi. Stochastic mRNA synthesis in mammalian cells. *PLoS biology*, 4(10):e309, 2006.

J. Ries. Kinematographie der befruchtung und zellteilung. *Archiv für mikroskopische Anatomie*, 74(1):1–31, 1909.

M. G. Rosenblum, A. S. Pikovsky, and J. Kurths. Phase synchronization of chaotic oscillators. *Physical Review Letters*, 76(11):1804, 1996.

N. Rosenfeld, J. W. Young, U. Alon, P. S. Swain, and M. B. Elowitz. Gene regulation at the single-cell level. *Science*, 307(5717):1962–1965, 2005.

P. Roux, S. Münter, F. Frischknecht, P. Herbomel, and S. L. Shorte. Technoreview: Focusing light on infection in four dimensions. *Cellular microbiology*, 6(4):333–343, 2004.

P. Rué. *Transient and stochastic dynamics in cellular processes*. PhD thesis, Universitat Politècnica de Catalunya, 2013.

P. Rué and J. Garcia-Ojalvo. Gene circuit designs for noisy excitable dynamics. *Mathematical Biosciences*, 231(1): 90–97, May 2011.

J. Sambrook, E. F. Fritsch, T. Maniatis, et al. *Molecular cloning*. Cold spring harbor laboratory press New York, 1989.

D. Segre, A. DeLuna, G. M. Church, and R. Kishony. Modular epistasis in yeast metabolism. *Nature genetics*, 37 (1):77–83, 2005.

V. Shahrezaei, J. F. Ollivier, and P. S. Swain. Colored extrinsic fluctuations and stochastic gene expression. *Molecular systems biology*, 4(1), 2008.

S. Sharma, J. R. Hoskins, and S. Wickner. Binding and Degradation of Heterodimeric Substrates by ClpAP and ClpXP. *Journal of Biological Chemistry*, 280(7):5449–5455, Feb. 2005.

R. Silva-Rocha and V. de Lorenzo. Implementing an OR–NOT (ORN) logic gate with components of the SOS regulatory network of Escherichia coli. *Molecular BioSystems*, 7(8):2389–2396, 2011.

J. Spizizen. Transformation of biochemically deficient strains of Bacillus subtilis by deoxyribonucleate. *Proceedings of the National Academy of Sciences of the United States of America*, 44(10):1072, 1958.

D. Sprinzak, A. Lakhanpal, L. LeBon, L. A. Santat, M. E. Fontes, G. A. Anderson, J. Garcia-Ojalvo, and M. B. Elowitz. Cis-interactions between Notch and Delta generate mutually exclusive signalling states. *Nature*, 465 (7294):86–90, 2010.

J. M. Sterlini and J. Mandelstam. Commitment to sporulation in Bacillus subtilis and its relationship to development of actinomycin resistance. *Biochem. J*, 113:29–37, 1969.

J. Stricker, S. Cookson, M. R. Bennett, W. H. Mather, L. S. Tsimring, and J. Hasty. A fast, robust and tunable synthetic gene oscillator. *Nature*, 456(7221):516–519, 2008.

S. H. Strogatz. *Nonlinear dynamics and chaos: with applications to physics, biology, chemistry, and engineering*. Westview press, 2000.

G. M. Süel, J. Garcia-Ojalvo, L. M. Liberman, and M. B. Elowitz. An excitable gene regulatory circuit induces transient cellular differentiation. *Nature*, 440(7083):545–550, 2006.

G. M. Süel, R. P. Kulkarni, J. Dworkin, J. Garcia-Ojalvo, and M. B. Elowitz. Tunability and noise dependence in differentiation dynamics. *Science*, 315(5819):1716–1719, 2007.

P. S. Swain, M. B. Elowitz, and E. D. Siggia. Intrinsic and extrinsic contributions to stochasticity in gene expression. *Proceedings of the National Academy of Sciences*, 99(20):12795–12800, 2002.

Y. Taniguchi, P. J. Choi, G.-W. Li, H. Chen, M. Babu, J. Hearn, A. Emili, and X. S. Xie. Quantifying E. coli proteome and transcriptome with single-molecule sensitivity in single cells. *Science*, 329(5991):533–538, 2010.

G. Tiana, S. Krishna, S. Pigolotti, M. H. Jensen, and K. Sneppen. Oscillations and temporal signalling in cells. *Physical Biology*, 4(2):R1–R17, June 2007.

S. Tojo, M. Matsunaga, T. Matsumoto, C. Kang, H. Yamaguchi, K. Asai, Y. Sadaie, K. Yoshida, and Y. Fujita. Organization and expression of the Bacillus subtilis sigY operon. *Journal of biochemistry*, 134(6):935, 2003. ISSN 0021-924X.

C. Tseng and G. Shaw. Genetic evidence for the actin homolog gene mreBH and the bacitracin resistance gene bcrC as targets of the alternative sigma factor SigI of Bacillus subtilis. *Journal of bacteriology*, 190(5):1561, 2008. ISSN 0021-9193.

R. Tsien. Opinion: imagining imaging's future. *Nature Reviews Molecular*, pages SS16–SS21, 2003.

M. Turcotte, J. Garcia-Ojalvo, and G. M. Süel. A genetic timer through noise-induced stabilization of an unstable state. *Proceedings of the National Academy of Sciences*, 105(41):15732–15737, 2008.

J. D. Wang and P. A. Levin. Metabolism, cell growth and the bacterial cell cycle. *Nature Reviews Microbiology*, 7 (11):822–827, 2009.

F. Wiegeshoff, C. Beckering, M. Debarbouille, and M. Marahiel. Sigma L is important for cold shock adaptation of Bacillus subtilis. *Journal of bacteriology*, 188(8):3130, 2006. ISSN 0021-9193.

M. V. Wilkes. Time-sharing computer systems. 1972.

A. T. Winfree. Biological rhythms and the behavior of populations of coupled oscillators. *Journal of theoretical biology*, 16(1):15–42, 1967.

Q. Yang, B. F. Pando, G. Dong, S. S. Golden, and A. van Oudenaarden. Circadian gating of the cell cycle revealed in single cyanobacterial cells. *Science*, 327(5972):1522–1526, 2010.

J. W. Young, J. C. Locke, A. Altinok, N. Rosenfeld, T. Bacarian, P. S. Swain, E. Mjolsness, and M. B. Elowitz. Measuring single-cell gene expression dynamics in bacteria using fluorescence time-lapse microscopy. *Nature Protocols*, 7(1):80–88, 2012.

M. W. Young and S. A. Kay. Time zones: a comparative genetics of circadian clocks. *Nature Reviews Genetics*, 2 (9):702–715, 2001.

S. Zellmeier, C. Hofmann, S. Thomas, T. Wiegert, and W. Schumann. Identification of $\sigma^V$-dependent genes of Bacillus subtilis. *FEMS microbiology letters*, 253(2):221–229, 2005. ISSN 1574-6968.

J. Zhang, R. E. Campbell, A. Y. Ting, and R. Y. Tsien. Creating new fluorescent probes for cell biology. *Nature Reviews Molecular Cell Biology*, 3(12):906–918, 2002.

S. Zhang and W. Haldenwang. Contributions of ATP, GTP, and redox state to nutritional stress activation of the Bacillus subtilis $\sigma^B$ transcription factor. *Journal of bacteriology*, 187(22):7554–7560, 2005.

M. Zimmer. Green fluorescent protein (GFP): applications, structure, and related photophysical behavior. *Chemical reviews*, 102(3):759–782, 2002.

U. Zuber, K. Drzewiecki, and M. Hecker. Putative sigma factor SigI (YkoZ) of Bacillus subtilis is induced by heat shock. *Journal of Bacteriology*, 183(4):1472, 2001.